Temperature Compensation of Aluminum Nitride Lamb Wave Resonators Utilizing the Lowest-Order Symmetric Mode

Chih-Ming Lin

Electrical Engineering and Computer Sciences
University of California at Berkeley

Technical Report No. UCB/EECS-2012-264
http://www.eecs.berkeley.edu/Pubs/TechRpts/2012/EECS-2012-264.html

December 14, 2012

Copyright © 2012, by the author(s).
All rights reserved.

Permission to make digital or hard copies of all or part of this work for personal or classroom use is granted without fee provided that copies are not made or distributed for profit or commercial advantage and that copies bear this notice and the full citation on the first page. To copy otherwise, to republish, to post on servers or to redistribute to lists, requires prior specific permission.

Temperature Compensation of Aluminum Nitride Lamb Wave Resonators Utilizing the Lowest-Order Symmetric Mode

by

Chih-Ming Lin

A report submitted in partial satisfaction of the

requirements for the degree of

Master of Science

in

Engineering – Electrical Engineering and Computer Sciences

in the

Graduate Division

of the

University of California, Berkeley

Committee in charge:

Professor Albert P. Pisano, Chair
Professor Richard M. White

Fall 2012

Temperature Compensation of Aluminum Nitride Lamb Wave Resonators Utilizing the Lowest-Order Symmetric Mode

by

Chih-Ming Lin

Research Project

Submitted to the Department of Electrical Engineering and Computer Sciences, University of California at Berkeley, in partial satisfaction of the requirements for the degree of **Master of Science, Plan II**.

Approval for the Report and Comprehensive Examination:

Committee:

Professor Albert P. Pisano
Research Advisor

(Date)

* * * * * * *

Professor Richard M. White
Second Reader

(Date)

Temperature Compensation of Aluminum Nitride Lamb Wave Resonators
Utilizing the Lowest-Order Symmetric Mode

Copyright © 2012

by

Chih-Ming Lin

Abstract

Temperature Compensation of Aluminum Nitride Lamb Wave Resonators
Utilizing the Lowest-Order Symmetric Mode

by

Chih-Ming Lin

Master of Science in Electrical Engineering and Computer Sciences

University of California, Berkeley

Professor Albert P. Pisano, Chair

Frequency references with a low phase noise and a low temperature-induced frequency drift are important components for navigation systems, wireless communication systems, and signal processing applications. As is well known, crystal oscillators (XOs) and temperature compensated crystal oscillators (TCXOs) based on AT-cut quartz dominate this market because AT-cut quartz has outstanding frequency-temperature performance and long-term stability. However, there are drawbacks and fabrication limitations for quartz-based resonators related to down-scaling for future applications. In addition, the material properties of quartz limit the integration of the frequency references and the complementary metal-oxide semiconductor (CMOS) circuits on a single chip. As a result, there has been a great interest in the realization of low-cost, CMOS-compatible, high quality factor (Q), and temperature-stable micro-electro-mechanical systems (MEMS) resonators.

Recently, Lamb wave mode propagating in piezoelectric thin plates has attracted great attention for the designs of electroacoustic resonators since it combines the advantages of bulk acoustic wave (BAW) and surface acoustic wave (SAW): ultra-high phase velocities and multiple frequencies excitation by an interdigital transducer (IDT). More specifically, the Lamb wave resonator (LWR) on an aluminum nitride (AlN) thin film have attracted many attentions because it can provide high acoustic phase velocity, small temperature-induced frequency drift, low motional resistance, and CMOS compatibility. The lowest-order symmetric (S_0) Lamb wave mode in an AlN thin plate is particularly preferred because it exhibits a phase velocity close to 10000 m/s, a low dispersive phase velocity characteristic, and a moderate electromechanical coupling coefficient. However, similar to the thin film bulk acoustic resonator (FBAR) and solid mounted resonator (SMR) using AlN thin films, the uncompensated AlN LWR also shows a first-order temperature coefficient of frequency (TCF) from –20 to –30 ppm/°C. This level of the frequency-temperature stability is unsuitable for any frequency reference or timing application.

In this work, temperature compensation of AlN LWRs using the S_0 Lamb wave mode is theoretically and experimentally investigated. By adding a compensating layer of silicon

dioxide (SiO_2) with an appropriate thickness ratio to the AlN thin film, the AlN/SiO_2 LWR can achieve a low first-order TCF at room temperature. In addition, LWRs with an AlN layer as thin as 250 nm are proposed to realize the temperature compensation over a wide frequency range from 100 MHz to 1 GHz. Using a multilayer plate composed of 1-µm-thick AlN and 0.83-µm-thick SiO_2, a temperature-compensated AlN/SiO_2 LWR operating at a series resonance frequency of 711 MHz exhibits a zero first-order TCF and a small second-order TCF of –21.5 ppb/°C^2 at its turnover temperature, 18.05 °C. The temperature dependence of fractional frequency variation is less than 250 parts per million (ppm) over a wide temperature range from –55 to 125 °C. The temperature-compensated AlN LWR is promising for future applications including thermally stable oscillators, filters, and sensors.

Professor Albert P. Pisano
Research Advisor

To my parents and Shing-Ting

TABLE OF CONTENTS

List of Figures iv

List of Tables viii

List of Abbreviations ix

Acknowledgments xii

Chapter 1 ***Introduction*** 1

1.1 Frequency References 1
1.2 Electrostatic Vibrating Resonators 4
1.2.1 Electrostatic Comb-Drive Resonator 5
1.2.2 Electrostatic Disk Resonator 6
1.3 Piezoelectric MEMS Resonators 6
1.3.1 Surface Acoustic Wave (SAW) Resonator 6
1.3.2 Bulk Acoustic Wave (BAW) Resonator 8
1.3.3 Lateral Extension Mode Resonator 10
1.3.4 Lamb Wave Resonator (LWR) 12
1.4 Temperature Compensation Techniques 13
1.4.1 Passive Temperature Compensation 14
1.4.2 Active Temperature Compensation 14
1.5 Outline 16

Chapter 2 ***Lamb Wave Modes Propagating in Piezoelectric AlN Membranes and AlN/SiO$_2$ Composite Plates*** 17

2.1 Why AlN Thin Film 17
2.2 Theoretical Analysis of Lamb Wave Modes in an AlN Plate 19
2.2.1 Transfer Matrix 19
2.2.2 Boundary Conditions 22
2.2.3 Effective Permittivity and Phase Velocity 23
2.2.4 Electromechanical Coupling Coefficient 26
2.3 Lamb Wave Modes in an AlN/SiO$_2$ Composite Plate 27
2.3.1 Boundary Conditions and Effective Permittivity 28
2.3.2 Phase Velocity 32
2.3.3 Electromechanical Coupling Coefficient 32

Chapter 3 ***Temperature-Compensated LWRs on AlN/SiO$_2$ Composite Plates*** 34

3.1 Electrode Metallization Selection for AlN LWRs 34
3.3.1 Lattice Mismatch between AlN and Metals 35
3.3.2 Effects on Phase Velocity and Electromechanical Coupling 37
3.2 First-order TCF of AlN LWRs 38

3.3 Zero First-order TCF of AlN/SiO_2 LWRs 39
3.4 Resonator Basics and Equivalent Circuits 43
3.5 Experimental Results and Discussions 46

Chapter 4 ***Microfabrication of Temperature-Compensated AlN/SiO_2 LWRs*** 54

4.1 Fabrication Process Flow 54
4.2 Metallization of Al Bottom Electrode 57
4.3 AlN Thin Film Deposition and Characterization 59
4.4 Low-Temperature Oxide (LTO) Hard Mask 61

Chapter 5 ***Conclusions and Future Research Directions*** 63

5.1 Summary 63
5.2 Future Research Directions 64
5.2.1 Temperature Compensation at High Temperatures 64
5.2.2 Temperature Compensation of the Second-Order TCF 65
5.2.3 Temperature Compensation for a Wide Frequency Range 65
5.2.4 Temperature Compensation Using Other Materials 65
5.2.5 Temperature-Stable Oscillators Using AlN/SiO_2 LWRs 65

Bibliography 67

LIST OF FIGURES

Figure 1-1. Cross-sectional illustration of a quartz resonator and some of its vibration mode shapes. 2

Figure 1-2. Illustrations of (a) XO, (b) VCXO, (c) TCXO / TCVCXO, and (d) OCXO / OCVCXO [2]. 3

Figure 1-3. Scanning electron micrograph (SEM) image of a capacitively transduced comb-drive resonator [15]. 5

Figure 1-4. SEM image of a 156 MHz electrostatic disk micromechanical resonator [17]. 5

Figure 1-5. (a) Cross-sectional illustration and (b) top view of one-port SAW resonator. 7

Figure 1-6. Cross-sections of various BAW resonators. 9

Figure 1-7. Cross-sectional illustration of the SMR. 10

Figure 1-8. Cross-sectional illustrations of (a) one-port and (b) two-port lateral extension mode resonators. 11

Figure 1-9. SEM images of (a) rectangular and (b) circular ring AlN resonators [37]–[39]. 11

Figure 1-10. Cross-sectional illustrations of two types of Lamb wave resonators. 12

Figure 1-11. Frequency-temperature characteristics of AT- and BT-cut quartz resonators. 13

Figure 1-12. Illustrations of passive temperature compensation for (a) SAW and (b) BAW resonators. 14

Figure 1-13. Principle of active temperature compensation of TCXOs. 15

Figure 2-1. Hexagonal wurtzite crystal structure of AlN, GaN and ZnO. 18

Figure 2-2. The coordinate system used in the theoretical analysis of a single piezoelectric layer. 19

Figure 2-3. Cross-sectional illustrations of two electrode arrangements of LWRs: (a) free bottom surface and (b) metallized bottom surface. 22

Figure 2-4. The effective permittivity of an AlN membrane with free bottom surface while AlN thickness (h_{AlN}) is 1 μm and the wavelength (λ) corresponds to 12 μm. 25

Figure 2-5. Normalized displacement profiles to surface potentials of the (a) A_0 and (b) S_0 Lamb wave modes in a 1-μm-thick AlN plate. 25

Figure 2-6. Simulated phase velocities of the first two Lamb wave modes propagating in an AlN plate. 26

Figure 2-7. Comparison of k^2 computed from the Green's function with the velocity difference method. 27

Figure 2-8. The coordinate system used in the analysis of a multilayer plate. 28

Figure 2-9. Cross-sectional illustrations of four electrode arrangements of composite LWRs: (a) free interface, (b) metallized interface, (c) free top surface, and (d) metallized top surface. 28

Figure 2-10. The effective permittivity of an AlN/SiO_2 membrane with free interface while h_{AlN} is 1 μm, h_{SiO_2} is 0.8 μm, and the wavelength λ corresponds to 12 μm. 31

Figure 2-11. Normalized displacement profiles to surface potentials of the (a) QA_0 and (b) QS_0 Lamb wave modes in an AlN/SiO_2 multilayer plate while h_{AlN} is 1 μm and h_{SiO_2} equals 0.8 μm. 31

Figure 2-12. Simulated phase velocity dispersion of the QS_0 Lamb wave mode for h_{SiO_2}/λ equal to 0, 0.05, 0.1, and 0.15, respectively. 32

Figure 2-13. Comparison of k^2 of various types of AlN/SiO_2 LWRs while the h_{SiO_2} is equal to 0.1λ. 33

Figure 2-14. Simulated k^2 of the type D device utilizing the QS_0 mode for h_{SiO_2}/λ equal to 0, 0.05, 0.1, and 0.15, respectively. 33

Figure 3-1. Illustration of an AlN LWR utilizing edge-type reflectors. 35

Figure 3-2. Simulated phase velocity of the S_0 mode in AlN films with various bottom metals while the metal thicknesses normalized to the wavelength are fixed to 0.015. 36

Figure 3-3. Simulated electromechanical coupling of the S_0 mode in AlN films with various bottom metals while the metal thicknesses normalized to the wavelength are fixed to 0.015. 37

Figure 3-4. Simulated TCFs of the AlN LWRs using the S_0 mode. 39

Figure 3-6. The effective thermal expansion experienced at the neutral plane. 40

Figure 3-5. Illustration of an AlN/SiO_2 LWR utilizing edge-type reflectors. 40

Figure 3-7. Simulated TCF dispersion of the AlN/SiO_2 LWRs using the QS_0 mode. 41

Figure 3-8. Required thickness ratios for the zero-TCF AlN/SiO_2 LWRs operating at different frequencies. 42

Figure 3-9. SiO_2 thickness and frequency dependence of the first-order TCF for four AlN thicknesses. 42

Figure 3-10. Modified Butterworth-Van Dyke (MBVD) equivalent circuit for a piezoelectric resonator. 44

Figure 3-11. A typical admittance spectrum including magnitude and phase of a piezoelectric resonator. 45

Figure 3-12. Measured broadband frequency spectrums of the two AlN/SiO_2 LWRs. 47

Figure 3-13. Close-up view of the frequency spectrums and the MBVD equivalent circuit fitting of (a) design 1 and (b) design 2 resonators. 48

Figure 3-14. The plot of measured fractional frequency variation versus temperature of the two LWRs. 49

Figure 3-15. Measured fractional frequency variation versus temperature of the design 1 LWR. 50

Figure 3-16. Measured fractional frequency variation versus temperature of the design 2 LWR. 50

Figure 3-17. Comparison of the frequency-temperature stability between the design 2 LWR and three selected crystal resonators. 51

Figure 3-18. The effect of the Al bottom electrode on the first-order TCF of the design 2 LWR. 52

Figure 4-1. Cross-sectional process flow for the AlN/SiO_2 LWRs. 55

Figure 4-2. SEM image of the fabricated AlN/SiO_2 LWR (design 2) using edge-type reflectors. 56

Figure 4-3. Cross-sectional SEM image of the AlN/SiO_2 composite membrane. 57

Figure 4-4. Normal coupled scan of the $Al(111)/AlN(0002)/SiO_2/Si$ layered structure. 58

Figure 4-5. Rocking curve scan of the 150-nm-thick Al (111) layer. 58

Figure 4-6. Normal coupled scan of the $AlN(0002)/Al(111)/SiO_2/Si$ layered structure. 60

Figure 4-7. Rocking curve scan of the 1-µm-thick AlN (0002) layer. 60

Figure 4-8. Microscope image of the Al electrode after LTO layer deposition. 61

Figure 4-9. Microscope images of the (a) Al top electrodes with 20-nm-thick Nb layer and (b) Al top electrodes with 400-nm-thick PECVD oxide layer after LPCVD LTO deposition. 62

Figure 4-10. Microscope images of the Al top electrodes with 20-nm-thick Nb after (a) 400-nm-thick PECVD oxide deposition and (b) then 2-µm-thick LPCVD LTO deposition. 62

LIST OF TABLES

Table 1-1. Performance comparison of common reference oscillators. 15

Table 2-1. Physical properties of ZnO, AlN, and GaN [29], [70]–[74]. 18

Table 2-2. Material constants of Al, SiO_2, and AlN used in the calculation. 24

Table 3-1. Physical properties of selected metals [29]. 36

Table 3-2. Temperature coefficients of Al, AlN, and SiO_2 used in simulation. 37

Table 3-3. Dimensions of the AlN/SiO_2 LWRs. 47

Table 3-4. Performance of the AlN/SiO_2 LWRs. 51

Table 4-1. Reactive sputtering conditions for AlN thin film deposition. 59

LIST OF ABBREVIATIONS

3C–SiC	Cubic Silicon Carbide
AC	Alternating Current
Al	Aluminum
AlN	Aluminum Nitride
BAW	Bulk Acoustic Wave
BCC	Body-Centered Cubic
BVD	Butterworth-Van Dyke
C	Capacitor
C_m	Motional Capacitor
CMOS	Complementary Metal-Oxide Semiconductor
DC	Direct Current
f_s	Series Resonance Frequency
f_p	Parallel Resonance Frequency
FBAR	Film Bulk Acoustic Resonator
FCC	Face-Centered Cubic
FPAR	Film Plate Acoustic Resonator
GaAs	Gallium Arsenide
GHz	Gigahertz
GSM	Global System for Mobile Communications
HBAR	High-Overtone Bulk Acoustic Resonator
ICP	Inductively Coupled Plasma
IDT	Interdigital Transducer
IF	Intermediate Frequency
kHz	Kilohertz
L	Inductor
LFE	Lateral-Field-Excited
LGS	Langasite
$LiNbO_3$	Lithium Niobate
$LiTaO_3$	Lithium Tantalate
L_m	Motional Inductor

LFE	Lateral Field Excitation
LPCVD	Low Pressure Chemical Vapor Deposition
LSN	Low Stress Nitride
LTO	Low Temperature Oxide
LWR	Lamb Wave Resonator
MBVD	Modified Butterworth-Van Dyke
MEMS	Microelectromechanical systems
MHz	Megahertz
Mo	Molybdenum
MOCVD	Metal Organic Chemical Vapor Deposition
N_2	Nitrogen
Nb	Niobium
OCXO	Oven-Controlled Crystal Oscillator
OCVCXO	Oven-Controlled Voltage-Controlled Crystal Oscillator
OMR	Over-Moded Resonator
PAW	Plate Acoustic Wave
PECVD	Plasma Enhanced Chemical Vapor Deposition
ppb	Parts-Per-Billion
ppm	Parts-Per-Million
Pt	Platinum
PVDF	Polyvinylidene Flouride
PZT	Lead Zirconium Titanate
Q	Quality Factor
R	Resistor
RIE	Reactive Ion Etching
R_m	Motional Resistor
RF	Radio Frequency
SAW	Surface Acoustic Wave
SEM	Scanning Electron Micrograph
SHF	Super High Frequency
Si	Silicon

SiC	Silicon Carbide
SiO_2	Silicon Dioxide
SiOF	Fluorine-Doped Silicon Oxide
SMR	Solidly Mounted Resonator
TCE	Temperature Coefficient of Elasticity
TCF	Temperature Coefficient of Frequency
TCP	Transformer Coupled Plasma
TCXO	Temperature-Compensated Crystal Oscillator
TCVCXO	Temperature-Compensated Voltage-Controlled Crystal Oscillator
TE	Thickness Extension
TeO_2	Tellurium Dioxide
TFE	Thickness-Field-Excited
Ti	Titanium
TMAH	Tetramethylammonium Hydroxide
TS	Thickness Shear
UHF	Ultra High Frequency
VCXO	Voltage-Controlled Crystal Oscillator
VHF	Very High Frequency
W	Tungsten
XO	Crystal Oscillator
XRD	X-Ray Diffraction
ZnO	Zinc Oxide

ACKNOWLEDGEMENTS

I would like to express, first, my sincere gratitude for the professional guidance and financial support given by my advisor and mentor, Professor Albert P. Pisano. It is my true honor to join his research group and the Berkeley Sensor and Actuator Center (BSAC) as a graduate student researcher. His invaluable advice on my research always inspires me to have creativity for my research. He also gives me complete freedom to pursue my own research interests and directions. I have always admired his vast knowledge of MEMS, leadership qualities, and sense of humor. He is the best adviser, the greatest teacher, and the top role model for me.

I would also like to acknowledge Professor Richard M. White for reading this research report. I have always been admired by his research on the interdigital transducer (IDT), acoustic wave devices, and piezoelectric materials. The invention of IDT prospers the microscale acoustic wave devices on many applications today.

I would like to thank Professor Clark T.-C. Nguyen for offering me the great opportunity of serving the graduate student instructor (GSI) of the EE C245 / ME C218 course (Introduction to MEMS Design) in the Fall Semester of 2009 and giving me technical advices on the RF MEMS resonators and filters.

I would like to show my deepest gratitude to my parents, Tsun-Chia and Hsiu-Mei, for their unlimited care and love throughout my life. Without their encouragement and support, I could not have completed this thesis and make my dream of studying abroad come true. I also owe my deep thanks to my girlfriend, Shing-Ting, for her unwavering patience and support over the years in the United States.

I would like to especially thank Dr. Jan H. Kuypers for his professional guidance on the AlN Lamb wave resonators during my first year at the University of California, Berkeley. In addition, I would like to acknowledge the two great project leaders, Dr. Matthew A. Hopcroft and Dr. Debbie G. Senesky, for their helpful discussions and invaluable guidance on the DARPA MiNaSIP and CSSA projects. I would like to thank Dr. Valery V. Felmetsger at the OEM Group Inc. for his help on AlN thin film deposition and inspired discussions. I would also like to thank Professor Gianluca Piazza at the Carnegie Mellon University for invaluable suggestions on the DARPA CSSA project. I particularly thank Professor Yung-Yu Chen at the Tatung University for the helpful discussions on the analytical theory of Lamb wave propagation, and Professor Jin-Chen Hsu at the National Yunlin University of Science and Technology for the insightful discussions on phononic crystals.

I am indebted to my colleagues in the Berkeley Micromechanical Analysis and Design (BMAD) group. I am particularly grateful to my friend and colleague, Ernest Ting-Ta Yen, for teaching me the fabrication processes of AlN Lamb wave resonators. In addition, I would like to acknowledge Wei-Cheng Lien for helpful discussion on cubic silicon carbide and relative materials. I would like to acknowledge Matilda Yun-Ju Lai, Dr. Gabriele Vigevani, and Fabian Goericke for sharing their fabrication experience on AlN-based devices with me. In addition, I would like to thank Matthew Chan, Sarah Wodin-Schwartz, Nuo Zhang, Chris D. McCoy, Kirti Mansukhani, Shiqian Shao, David Rolfe, Jie Zou, and Dr. Ayden Maralani for helpful discussion and suggestion during the

weekly HEaTS meeting. Especially thanks to Helen Kim and Yulia Golubovskaya for their incredible dedication to BMAD financial management.

I want to give my special thanks to the Marvell Nanofabrication Laboratory staff for their help and assistance, especially Dr. Xiaofan Meng, for help on the deposition of many metal layers. I particularly want to acknowledge Joe Donnelly who was able to stand my exhausting requests for assistance and help on the AMS and Endeavor AlN sputtering tools. At the same time, I wish to thank Zeying Ren for giving me invaluable suggestions on MEMS fabrication and tool assistance.

I would like to extend my sincere thanks to my dear friends, Yang Lin, Wei-Chang Li, Jun-Chau Chien, Yenhao Philip Chen, Lingqi Wu, Lamei Li, Fangran Xu, Chung-Wei Lin, Sean Shih, Ying-Yu Lin, Nai-Kuei Kuo, Huai-Yuan Tseng, Ting-Ying Chung, Yung-Kan Chen, and Yu-Chu Huang. With their company in the United States, I have a wonderful and enjoyable life outside the work environment.

Lastly, I would like to thank the funding support from the DARPA MiNaSIP and CSSA projects of the Microsystems Technology Office, the Geothermal R&D project of the U.S. Department of Energy, and the Anselmo John Macchi Fellowship fund in Engineering of the University of California, Berkeley.

Chapter 1

Introduction

Quartz resonators and surface acoustic wave (SAW) filters have been employed in many timing and frequency control applications, but the integration with complementary metal-oxide semiconductor (CMOS) circuits is still an unsolved problem due to their fabrication incompatibility of piezoelectric bulk materials with silicon (Si) wafers in nature. On the other hand, film bulk acoustic resonators (FBAR) and filters can be fabricated on Si wafers and form one of the enabling technologies for the radio technology used in various wireless communication systems. For bulk acoustic wave (BAW) devices, however, it is challenging to enable multiple resonance frequencies on a single Si chip. In recent years, plate acoustic wave (PAW) resonators (i.e. Lamb wave resonators) based on sputtered aluminum nitride (AlN) thin films are promising for high-frequency applications up to several gigahertz (GHz), multiple resonance frequencies on a single chip, and fabrication compatibility with CMOS circuits. The Lamb wave resonators (LWRs) can be served as frequency references in the electronic systems for frequency synchronization and clock sources as well as employed as GHz-range bandpass filters selecting the appropriate frequency ranges for the mobile phone radio to receive and transmit its communication signals, blocking out the other unwanted signals.

1.1 Frequency References

Almost all electronic systems need a frequency reference source for keeping track of real time or setting precise clock frequency for digital data transmission. The performance of the electronic systems usually depends on the accuracy and stability of the timing clock and frequency reference. Therefore, frequency references constitute a multi-billion dollar market in electronic industries today. For common consumer-type applications, two technologies are usually distinguished: mechanical and electrical reference oscillators. In mechanical reference oscillators, the frequency elements are essentially mechanical vibrating devices, which provide the stable natural resonance frequencies. In electrical reference oscillators, the frequency elements are integrated on the chip and comprise a network of resistors (R) and capacitors (C) or an inductor-capacitor (L-C) filter for clocking, logic, or frequency synthesizer applications [1]. Over the past few decades, the mechanical reference oscillators (e.g. quartz crystals) have dominated the market and

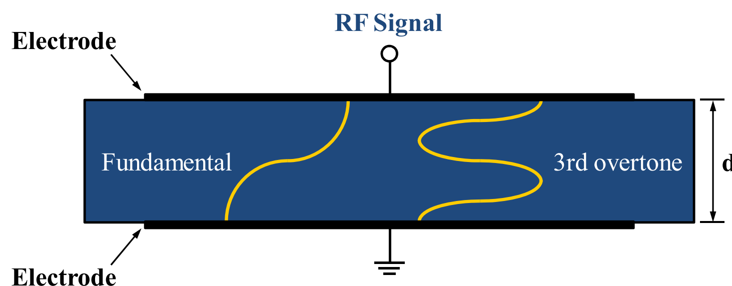

Figure 1-1. Cross-sectional illustration of a quartz resonator and some of its vibration mode shapes.

have been widely used in many electronic systems.

Quartz is basically crystallized silicon dioxide (SiO_2) and belongs to 32 symmetry group of the trigonal system. It exhibits intrinsic a high quality factor (Q), making quartz resonators and oscillators widely used as the reference signal source in circuitry [2]. As depicted in Fig. 1–1, one-port quartz crystal has two deposited electrodes on each side of the slab. When a thickness vibration mode is excited in the quartz slab, the resonance frequency (f_0) of the vibration mode is determined by the acoustic wave velocity and the slab thickness. For the fundamental mode, the resonance frequency can be estimated by the wave synchronism expression,

$$f_0 = v_a / \lambda = v_a / 2\mathrm{d}, \tag{1.1}$$

where v_a is the acoustic wave velocity, λ is the wavelength, and d represents the thickness of the crystal slab. The resonance frequency of the quartz resonator is typically specified from tens of kilohertz (kHz) to a few tens of megahertz (MHz). As shown in Fig. 1–1, high-order harmonic vibration modes also co-exist with the fundamental vibration mode in the crystal slab. Due to the reverse polarity of the two electrodes, only odd harmonic vibration modes can be excited in the quartz plate. A common crystal oscillator (XO) is an electronic oscillator circuit that uses the primary mechanical resonance of a quartz crystal to create an electrical signal with a very precise frequency. The precise frequency is usually used to keep track of time, to provide a stable clock signal for digital integrated circuits, and to stabilize frequencies for transmitters and receivers.

As shown in Fig. 1–2 (a), a crystal oscillator consists of a quartz crystal and a positive feedback transistor, and an output buffer amplifier. The crystal oscillator circuit sustains oscillation by taking a voltage signal from the quartz resonator, amplifying it, and then feeding it back to the resonator. Fig. 1–2 (b) presents a voltage-controlled crystal oscillator (VCXO) whose resonance frequency can be changed by applying direct current (DC) voltages to the VCXO. By employing a varactor diode, the oscillator is allowed to shift the resonance frequency by adjusting the effective capacitance. When the control voltage offsets the resonance frequency of the crystal oscillator, it doesn't improve the resonance frequency accuracy over temperature or supply voltage variations. The VCXO has a resonance frequency as accurate as a quartz crystal resonator contains. The budget for frequency errors in the radio frequency (RF) systems is significantly less than those in lower frequency applications, and the oscillation frequency variations of low-cost XOs

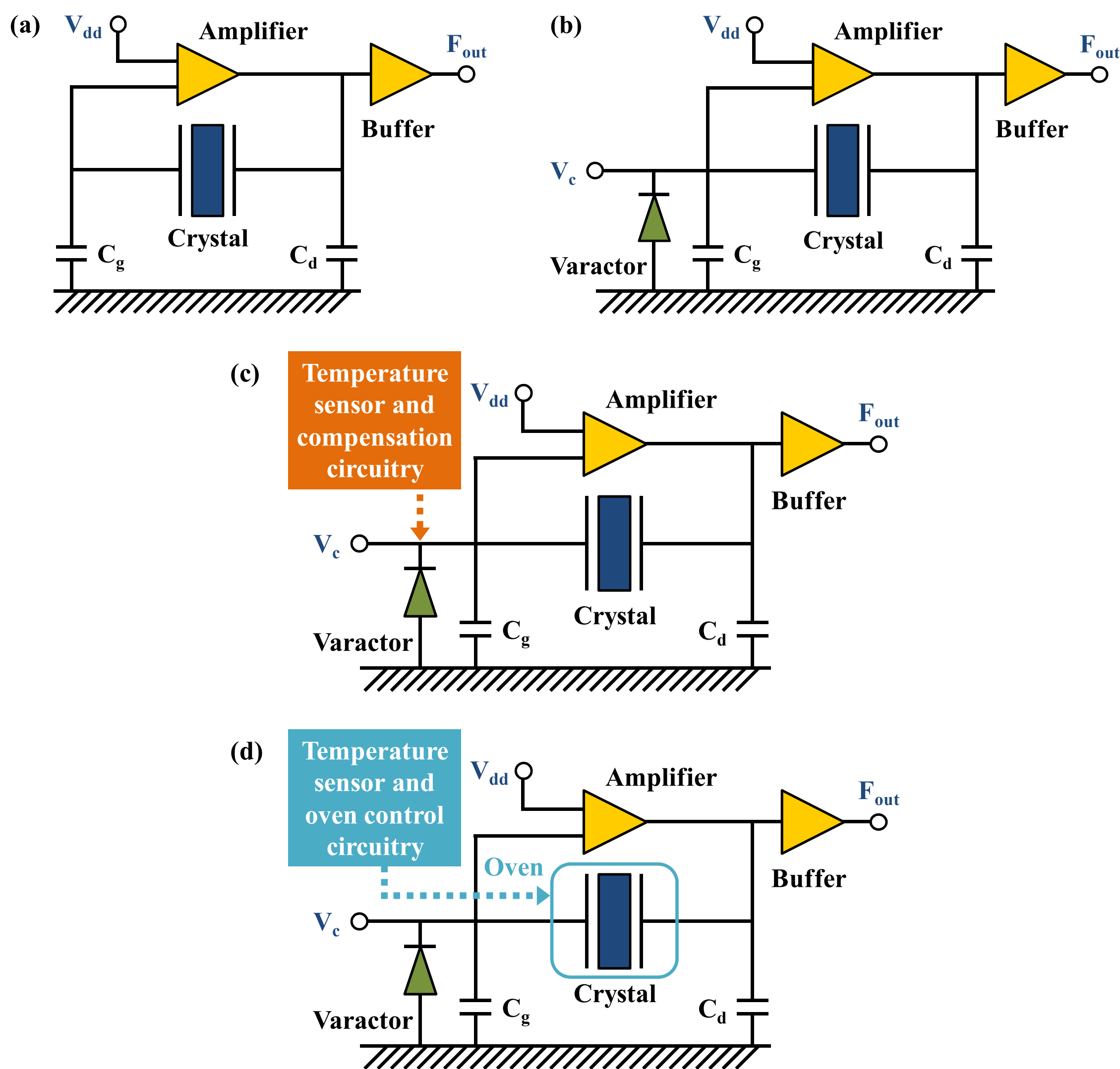

Figure 1-2. Illustrations of (a) XO, (b) VCXO, (c) TCXO / TCVCXO, and (d) OCXO / OCVCXO [2].

exceed the requirement due to the temperature dependency.

Therefore, additional temperature sensor and control circuitry are required to improve the frequency accuracy of the VCXO over the temperature variations, which cause a frequency drift from a fraction of parts-per-million (ppm) to hundreds of ppm. Fig. 1–2 (c) shows a temperature-compensated crystal oscillator (TCXO) as well as a temperature-compensated VCXO (TCVCXO), which employs a temperature sensor to sense the temperature variation and a temperature compensation circuitry to minimize oscillation frequency drifts caused by the temperature variations. Fig. 1–2 (d) depicts an oven-controlled crystal oscillator (OCXO) as well as an oven-controlled VCXO (OCVCXO), which employs a temperature sensor to sense the temperature variations and then uses a temperature-controlled oven. The temperature-controlled chamber is used to maintain the quartz crystal of the crystal oscillator at a constant temperature for preventing changes in

the oscillation frequency due to variations in ambient temperature. The OCXO usually achieves the highest frequency stability among the XO family. Although quartz crystal oscillators exhibit outstanding advantages, such as high Q and excellent temperature stability, for clocks and frequency references, unfortunately the quartz crystals are often too large in size and hard to integrate with the single CMOS chip. In other words, quartz crystals need to interface with other circuit components on the board, forming a bottleneck for the miniaturization of the electronic systems.

With the emerging progress of microelectromechanical systems (MEMS) technology, mechanical structures with ability to shrink mechanical features and mechanisms down to micro- and nano- scales can be fabricated on Si wafers [3]. With further development of interface circuitry, MEMS devices can provide substantial size and power reduction for timekeepers and frequency control functions in wireless systems. In particular, vibrating micromechanical resonators based on polysilicon and piezoelectric layers have now been demonstrated with their Q's greater than 3,000 at the GHz-range resonance frequencies [4]–[7]. Micromechanical vibrating resonators have also been embedded into oscillator circuits to achieve excellent phase noise performance, satisfying global systems for mobile communications (GSM) specifications for reference oscillators [8]–[13]. The extraordinary small size, high level of integration with CMOS chips, and low cost of micromechanical vibrating devices open exceptional possibilities for enabling miniature and precision oscillators at low cost. Moreover, it can be expected that a MEMS-based oscillator has a superior phase noise performance and frequency stability compared to an electrical oscillator because the MEMS-based oscillator is based on mechanical vibration which usually exhibits a high Q. That is to say, MEMS vibrating resonators fill the gap between high-performance non-CMOS compatible technologies and low-performance CMOS compatible technologies. It appears that the replacement of the crystal resonator with the MEMS vibrating resonator and the integration of the MEMS resonator with the CMOS circuits in a single die will lead to a significant reduction in board complexity and bill-of-materials of electronic circuits [1].

1.2 Electrostatic Vibrating Resonators

The capacitively transduced resonators using various micromechanical structures, such as cantilever beams or clamped-clamped beams, are driven by parallel-plate capacitive electrostatic forces [3], [14]. The capacitive transduction usually utilizes an electrostatic force across a sub-micron gap (usually smaller than 1 μm) to drive the micromechanical structure and then to sense the motional current. The Q's of the electrostatic resonant structures are very low at atmospheric pressures because of the squeeze-film air damping in a sub-micron air gap, but the Q's can be raised by orders of magnitude in vacuum [3]. In addition, the resonance frequency of the electrostatic vibrating resonator is determined by the lateral dimensions and can achieve multiple frequencies on a single chip. However the large motional resistance (R_m) of electrostatic resonant devices makes the interface with the 50-ohm RF system very difficult.

1.2.1 Electrostatic Comb-Drive Resonator

The first electrostatic vibrating comb-drive resonator was reported by Tang *et al.* in 1989 [15]. As shown in Fig. 1–3, the comb-drive resonator usually consists of a finger-supporting shuttle mass suspended several micron height above the substrate by folded flexures, which are anchored to a ground plane on the substrate. The ground plane should be in electrical contact with the suspended structure to prevent pulling in the structure. The electrostatic comb-driven and sensed lateral resonators offer numerous advantages over parallel-plate driven resonators. The most significant advantage is that the drive capacitance is linear with its displacement, resulting in a driving force independent on the vibration amplitude [15]. The resonance frequency of the comb-drive vibrating resonator is determined by material properties and lateral geometries [15], [16]. However, the resonance frequency of the vibrating comb-drive resonator is usually below 1 MHz due to the low spring constant of the long folded beam structure.

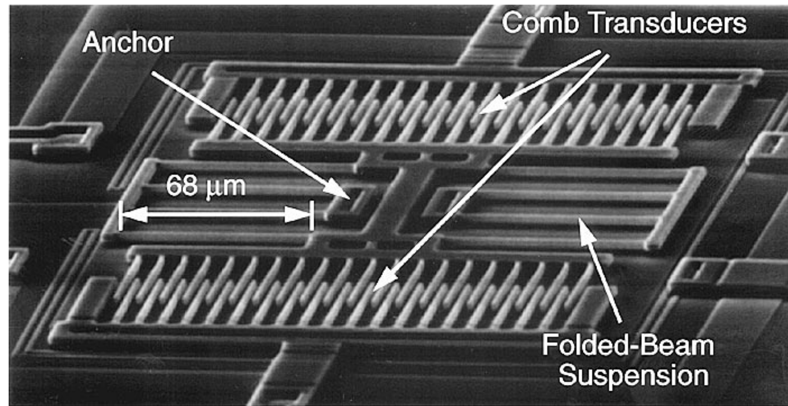

Figure 1-3. Scanning electron micrograph (SEM) image of a capacitively transduced comb-drive resonator [15].

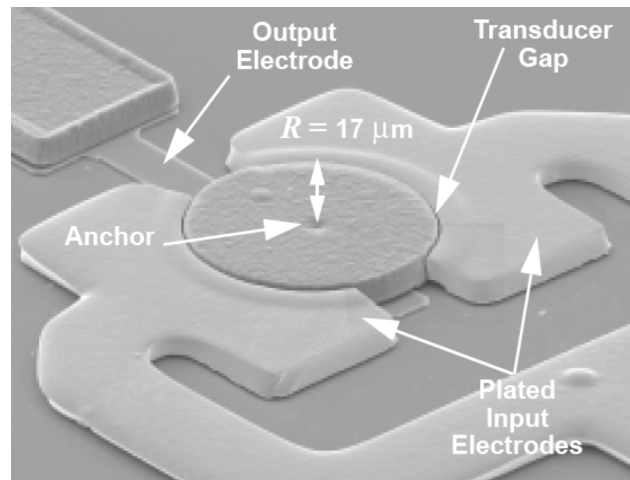

Figure 1-4. SEM image of a 156 MHz electrostatic disk micromechanical resonator [17].

1.2.2 Electrostatic Disk Resonator

Similar to the CMOS transistors, extending the resonance frequency of micromechanical resonators generally requires scaling of micromechanical resonators. However, smaller dimension often coincides with smaller power handling and lower *Q*. In 2000, as shown in Fig. 1–4, Clark *et al.* proposed a new micromechanically vibrating disk resonator [17]. Based on the radial contour mode, the micromechanical disk structure can attain very high frequencies while retaining relatively large dimensions because the high stiffness of the disk structure. Particularly, the resonance motion of the contour mode is purely radial so the disk center is a motionless nodal point during vibration. The fundamental contour mode of the micromechanical resonator can achieve a *Q* as high as 23000 at 193 MHz since energy losses to the substrate are minimized by anchoring the resonator at its center to reduce the mechanical motion [17], [18]. However, like the comb-drove resonator, the electrostatic disk resonator has a large motional resistance up to several thousand ohms, causing the impedance mismatch problem with the 50-ohm RF system.

1.3 Piezoelectric MEMS Resonators

Piezoelectricity was discovered by the brothers Curie in 1880 and received its name in 1881 from Hankel. In 1915, Langevin utilized a bulk acoustic wave transducer (steel-quartz-steel) in pulse echo experiments at a high frequency of 150 kHz for submarine detection in water. Cady followed up Langevin's work and developed quartz resonators for stabilizing electronic oscillators in 1921 [19]. In fact, acoustic wave devices based on piezoelectric materials have been used in commercial applications for over 70 years [20].

Generally acoustic wave devices refer to surface acoustic waves, bulk acoustic waves, and plate acoustic waves, but are not limited to this category. Metal electrodes are used as transducers on piezoelectric materials to convert electrical energy into mechanical displacement and vice versa, while employing different types of acoustic waves in solids. As their names suggest, SAW resonators take advantage of surface acoustic waves propagating on the top surface of the substrate, while BAW resonators employ bulk acoustic waves propagating in the thickness direction of the plate and LWRs employ plate acoustic waves propagating in the lateral direction of the plate. The most common piezoelectric substrate materials are quartz, lithium tantalate ($LiTaO_3$), and lithium niobate ($LiNbO_3$). Other piezoelectric materials with commercial potential include AlN, zinc oxide (ZnO), gallium arsenide (GaAs), silicon carbide (SiC), langasite (LGS), lead zirconium titanate (PZT), and polyvinylidene flouride (PVDF). Each piezoelectric material has its specific advantages and disadvantages, such as temperature dependence, attenuation, electromechanical coupling, phase velocity, and cost [20].

1.3.1 Surface Acoustic Wave (SAW) Resonator

Extensive research work in the ultrasonic field continues in the 19th and 20th centuries

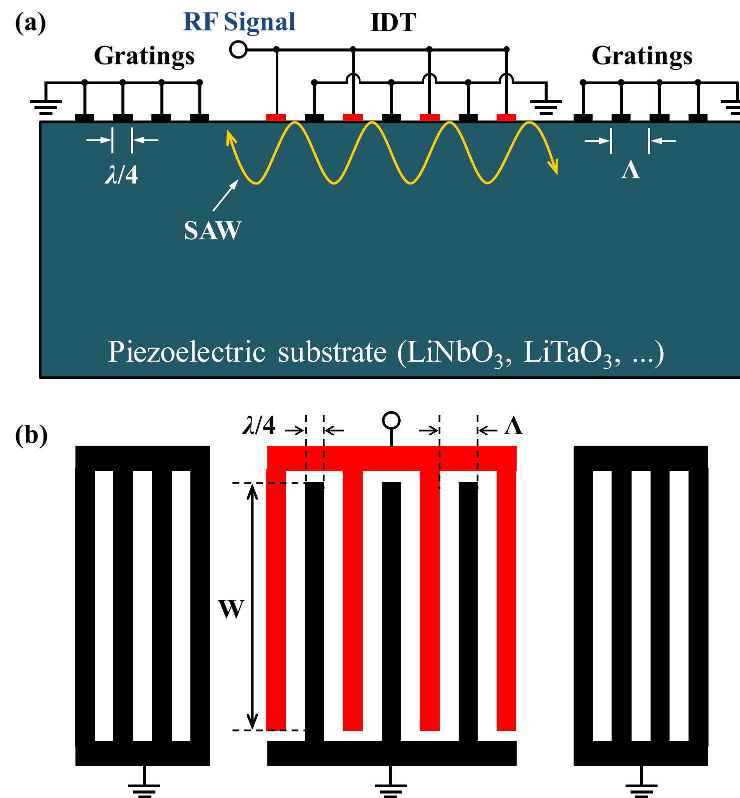

Figure 1-5. (a) Cross-sectional illustration and (b) top view of one-port SAW resonator.

after Rayleigh discovered surface waves propagating in solids in 1885 [21]. Although it remained a scientific curiosity with very few applications for a long time, the direct generation and detection of surface elastic waves through the piezoelectric effect led to a breakthrough in SAW devices after the invention of an interdigital transducer (IDT) by White and Voltmer in 1965 [22]. The interdigital finger width is usually equal to quarter wavelength ($\lambda/4$) and the interdigital electrode pitch (Λ) equals half wavelength ($\lambda/2$). SAW resonators and filters have been used for many electronic applications since then. One of the earliest SAW device applications was an intermediate frequency (IF) bandpass filter for television receivers, first developed in the 1970s [23].

SAW devices have been widely used as IF and RF filters in wireless transmission systems for several decades because of their small size, low cost, and great performance. They also have drawn much attention for dozens of sensing applications because most of acoustic energy of surface elastic waves is confined within one wavelength depth under the substrate surface, leading to high sensitivity. Fig. 1–5 shows the configuration of a typical one-port SAW resonator consisting of one IDT and two grating reflectors at both sides of the piezoelectric substrate. SAWs can be generated by applying RF signals to the IDT and propagate on the surface of the substrate along the direction perpendicular to the IDT length. The generated SAW would be reflected by the gratings at both sides, and consequently forms standing waves between the two sets of grating reflectors. The single IDT in the center is also used for receiving the reflected SAWs.

However, SAW phase velocities of common piezoelectric substrates, such as quartz, $LiNbO_3$, and $LiTaO_3$, are below 4000 m/s. Therefore, the center frequencies of SAW devices are usually limited to 3 GHz since strict shrinkage of IDT finger widths is required for achieving higher center frequencies. In order to enable high-frequency SAW devices, a piezoelectric substrate with a high phase velocity is an alternative. It is well-known that diamond has the highest acoustic wave velocity among all materials because of its high Young's modulus up to 1143 GPa [24]; therefore, layered SAW devices including a piezoelectric thin film, such as AlN or ZnO, and a polycrystalline diamond layers on a Si substrate have been utilized for high-frequency SAW devices [25]–[28].

1.3.2 Bulk Acoustic Wave (BAW) Resonator

For any material, there are three possible BAW propagation modes: longitudinal wave, shear horizontal (SH) wave, and shear vertical (SV) wave, where SH mode is polarized in the horizontal plane and SH mode is polarized in the vertical plane. In general, each mode has a different phase velocity and a different piezoelectric coupling coefficient due to the different polarization. Among these three BAW modes, longitudinal wave has the highest phase velocity and it is often called the P-wave to stand for primary wave. BAW resonators employ acoustic waves propagating through the bulk of a material. Generally the transduction of BAW requires the application of an alternating current (AC) electric field, applied to or in close proximity to, the surface of the piezoelectric plate using metal electrodes [29] and then acoustic waves propagate in longitudinal or shear modes. For quartz crystal resonators, thickness shear (TS) mode in the AT-cut quartz is the most common mode because it has the best temperature stability and efficient energy trapping underneath the coated electrodes on the crystal plate [30]. The resonance frequency of the AT-cut crystal resonator is determined by the plate thickness and the phase velocity of shear wave, rather than by the overall plate dimensions.

However, due to difficult manufacture of the quartz crystal plate thinner than 20 μm by grinding, manufacturers have difficulty in producing crystals to reach a fundamental frequency over 80 MHz [2]. To produce higher frequency oscillators, quartz crystals are often designed to operate at third, fifth, or seventh overtones because a thicker crystal plate is easier to manufacture than a crystal resonator utilizing the fundamental mode at the same operation frequency. To achieve a GHz resonance frequency, a piezoelectric thin plate with a thickness less than 5 μm is needed. Therefore, instead of grinding the plate thickness of the quartz crystal, piezoelectric thin films grown on Si substrates by using reactive sputtering or metal organic chemical vapor deposition (MOCVD) have been successfully utilized to enable BAW resonators operating in ultra high frequency (UHF) and super high frequency (SHF) regions.

Film Bulk Acoustic Resonator (FBAR)

An FBAR or BAW resonator is normally operated in thickness extension (TE) mode, whose resonance frequency is determined by the thickness of the piezoelectric thin film and the phase velocity of longitudinal wave rather than by the lateral dimensions of the

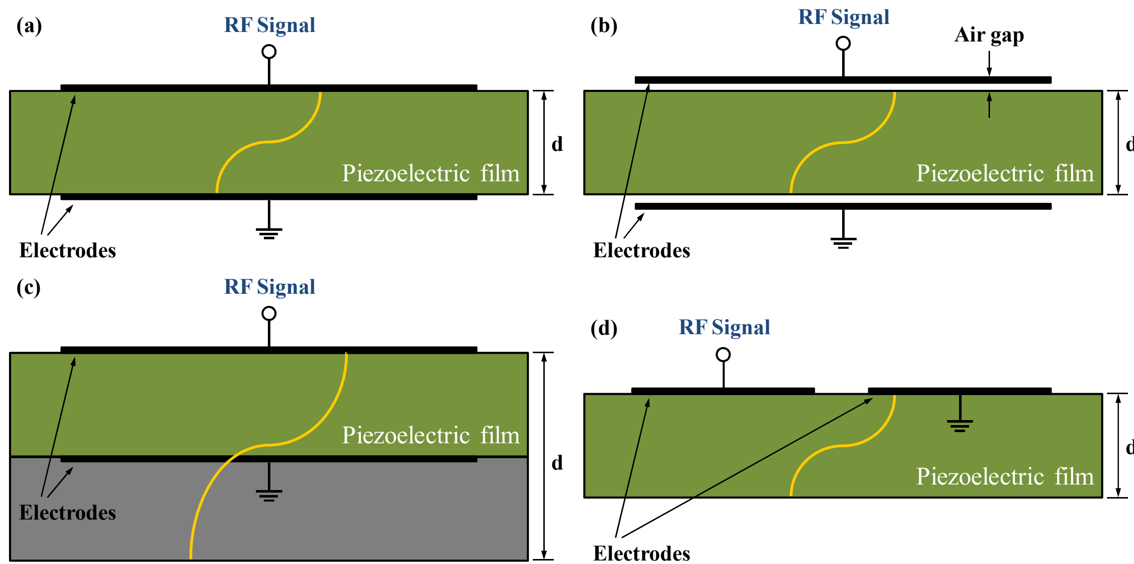

Figure 1-6. Cross-sections of various BAW resonators.

piezoelectric plate. The FBAR using an external electrical field parallel to the normal of the piezoelectric plate is called thickness-field-excited (TFE) resonator as shown in Figs. 1–6 (a), (b), and (c) [29]. Fig. 1–6 (a) presents the cross-sectional illustration of the FBAR which is sandwiched between top and bottom electrodes. The outer metal surfaces are against air so that the longitudinal wave reflects off the surfaces and the standing wave resonance is confined in the piezoelectric material body. As shown in Fig. 1–6 (b), the top and bottom metal electrodes are very close to the piezoelectric thin plate but not in contact with it. Small air gaps between the piezoelectric plate and metal electrodes ensure the voltage is applied to the piezoelectric body and the Q is enhanced since thin metal electrodes have too much electrical loss. However, the additional capacitances in the two air gaps also reduce the effective coupling (k^2_{eff}).

Fig. 1–6 (c) depicts an FBAR structure on another substrate whose thickness is often a number of wavelengths. Resonances occur at frequencies where the total resonator thickness corresponds to one or many half wavelengths. This topology is usually called over-moded resonator (OMR) or high-overtone bulk acoustic resonator (HBAR). With a large number of half waves in the substrate layer, most of the acoustic energy is stored in the substrate so a high Q over 70000 can be achieved when an appropriate material, such as sapphire, is used as the substrate layer [31]. The lateral-field-excited (LFE) resonator, as shown in Fig. 1–6 (d), has both electrodes on the same plate face, leaving the opposing surface bare. An LFE BAW resonator is excited with the fringing electrical fields across the gap between the electrodes and operated in TS mode, whose resonance frequency is determined by the thickness of the piezoelectric plate and the shear wave velocity.

Solidly Mounted Resonator (SMR)

The solidly mounted resonator (SMR) in Fig. 1–7 is considerably different form than the

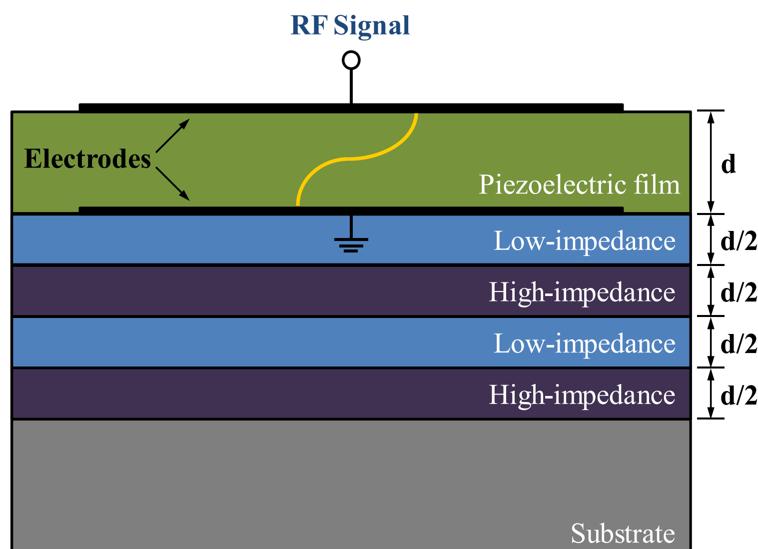

Figure 1-7. Cross-sectional illustration of the SMR.

BAW resonators described above. The piezoelectric thin film is sandwiched between top and bottom electrodes but solidly mounted to the substrate; therefore, excellent acoustic isolation of the piezoelectric thin film from the substrate is required if a high-Q resonance is desired. In 1965, Newell described a reflector array which is nominally composed of quarter-wavelength-thick layers to provide acoustic isolation [32]. The reflector array is called a Bragg reflector which consists of many pairs of high and low acoustic impedance layers and is utilized to reflect the acoustic energy back to the piezoelectric layer. If the substrate has relatively high acoustic impedance, the first layer on the top surface of the substrate should have low acoustic impedance, the next layer, high acoustic impedance, and so on.

Since AlN and most piezoelectric materials have moderately high acoustic impedance, the first under the piezoelectric thin film is of low acoustic impedance and SiO_2 is usually used. Because tungsten (W) has relatively high acoustic impedance, each following layer boundary has a higher reflection coefficient and then fewer layers are required. Thus a suitable sequence might be "SiO_2 and AlN" or "SiO_2 and W" on Si or sapphire substrates. The Bragg reflector diminishes the acoustic wave amplitude with the depth into itself [29], [31]. The number of the Bragg reflector layers required for a satisfactory reflection coefficient most depends on the acoustic impedances between layers. Since the SMR is constructed on the non-free-standing physical structure, it can provide better mechanical robustness and good power handling.

1.3.3 Lateral Extension Mode Resonator

Except for the TS and TE modes, lateral extension mode in a thin plate is also utilized in piezoelectric resonators [33]. Before 1937, many work focused on the development of TS mode crystal resonators. In 1937, Hight and Willard described the CT- and DT-cut

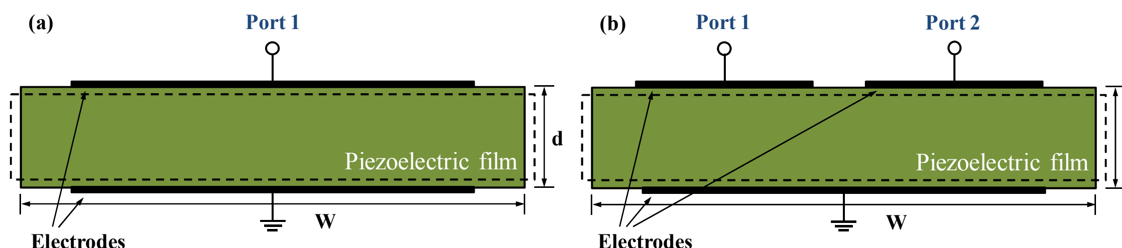

Figure 1-8. Cross-sectional illustrations of (a) one-port and (b) two-port lateral extension mode resonators.

crystal resonators operating in face shear mode shows a zero temperature coefficient [34], [35]. Later, in 1940, Mason proposed a new GT-cut crystal resonator operating in lateral extension mode that exhibits the best frequency-temperature behavior among all well-known crystal resonators [36]. Since then a great deal of research work has been devoted to contour-mode crystal resonators, including the shear mode and lateral extension mode. Moreover, the vibration motion of the contour mode mostly occurs in plane so the resonance frequency of the contour-mode resonator is determined by lateral dimensions (e.g. length or diameter). For example, as shown in Fig. 1–8, the resonance frequency of the lateral extension mode resonator is determined by its width or length rather than the plate thickness. As a result, contour-mode resonators are devoid of the main drawback of FABRs and SMRs, namely incapacity of achieving multiple frequencies on a single chip.

In order to enable higher resonance frequency, Piazza and Pisano tried to develop contour-mode resonators using AlN thin films since 2002 [37]. Similar to the FBAR, as shown in Fig. 1–8, the contour-mode resonator body is made of an AlN plate sandwiched between top and bottom electrodes, and two quarter-wavelength long tethers are normally used to suspend the resonator in air [38], [39]. Fig. 1–9 shows the scanning electron micrograph (SEM) images of rectangular and circular ring contour-mode resonators. The rectangular plate resonator can be excited in length-extensional and width-extensional modes and the circular ring resonator is excited in radial contour mode. As shown in Fig. 1–9 (b), notches were also introduced in the circular ring structure in order to minimize the interference of the anchor on the vibration mode shape. Typically the AlN contour-mode resonators show Q's of several thousands and low motional impedance at the very high frequency (VHF) range (30–300 MHz) [37]–[39]. Unfortunately, with an increasing

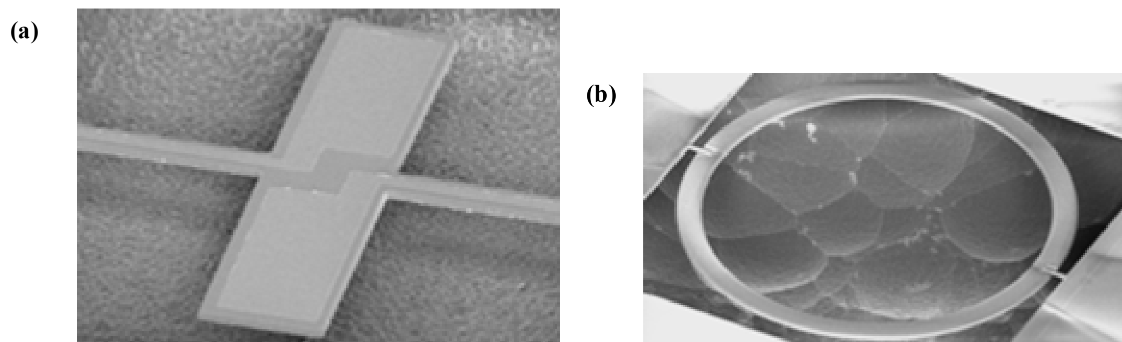

Figure 1-9. SEM images of (a) rectangular and (b) circular ring AlN resonators [37]–[39].

interest in higher resonance frequencies, scaling of AlN contour-mode resonators causes a considerable increase on motional impedance which is usually in reciprocal proportion to the effective transduction area.

1.3.4 Lamb Wave Resonator (LWR)

In 1973, Toda first realized a Lamb wave device on a PZT ceramic plate [40]. Since then Lamb wave devices utilizing the lowest-order antisymmetric (A_0) mode propagation in ZnO thin plate were widely studied for sensors applications [41] since the A_0 mode has a phase velocity slower than the compressional wave velocity in most liquids. In this situation, the A_0 Lamb wave cannot radiate its energy into the surrounding liquid with the higher velocity [42]. Recently, Lamb wave modes propagating in an AlN thin plate have attracted great attention for the designs of electroacoustic resonators since it combines the advantages of BAW and SAW: high phase velocity and multiple-frequency excitation by an IDT. More specifically, the lowest-order symmetric (S_0) Lamb wave mode in an AlN thin plate is particularly preferred because it exhibits a phase velocity close to 10000 m/s, a low dispersive phase velocity characteristic, and a moderate electromechanical coupling coefficient [43]–[53]. In addition, AlN LWRs are able to simultaneously solve the high motional impedance issue faced by electrostatic resonators, the low resonance frequency limitation faced by piezoelectric contour-mode resonators, and the multiple frequency capability problem faced by piezoelectric BAW resonators.

In recent years, the AlN LWRs are being developed in two different topologies with respect to the Lamb wave reflection. As presented in Fig. 1–10 (a), like SAW resonators, the first topology is based on the reflection from periodic grating reflectors with an electrode width of quarter wavelength [43]–[46]. The second topology is based on the reflection from suspended free edges of the thin plate as depicted in Fig. 1–10 (b) [47]–[53]. Lamb wave modes can be generated by applying RF signals to the IDT and then propagate in the AlN thin plate. The generated Lamb waves are reflected by the periodic

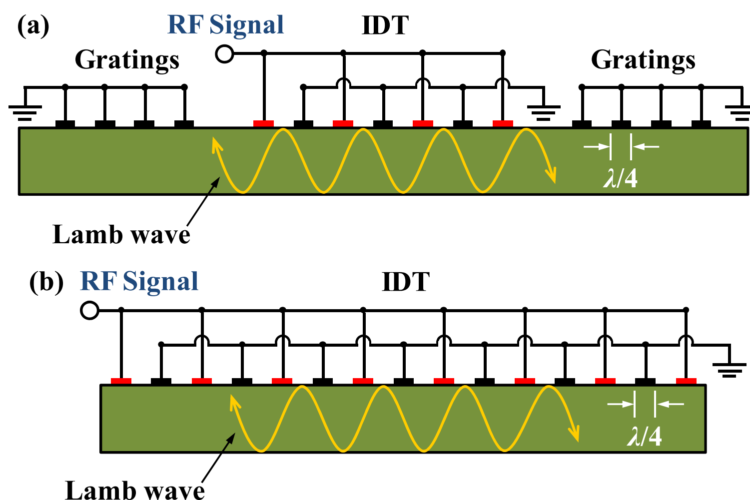

Figure 1-10. Cross-sectional illustrations of two types of Lamb wave resonators.

metal gratings or the suspended free edges at both sides, and consequently the standing wave resonance forms inside the AlN plate. In general, Lamb wave conversion into other modes does not occur while it propagates along a long periodic grating whereas Lamb waves would exhibit mode conversion upon reflection at the suspended free edges [54]. Mode conversion loss significantly depends on the wavelength, plate thickness, and Lamb wave mode. Fortunately, the lowest-order Lamb wave modes don't exhibit mode conversion upon reflection at the suspended free edges and can be fully reflected [55].

1.4 Temperature Compensation Techniques

As mentioned above, crystal resonators are the most commonly used in signal processing, due to their excellent temperature stability, long-term stability, and manufacturability. Quartz has different elastic, piezoelectric, and dielectric properties according to the different orientations of the crystal cuts. Therefore, by slicing the quartz at various cuts with respect to its axes, it is possible to obtain a variety of crystal resonators with different temperature characteristics. For example, as shown in Fig. 1–11, AT- and BT-cut quartz resonators operating in TS mode exhibit different frequency-temperature characteristics. The AT-cut quartz resonator has excellent frequency stability over a wide temperature range since its first- and second-order temperature coefficients of frequency (TCF) are zero at room temperature and the frequency-temperature characteristic is only determined by a third-order function of temperature deviation [2].

However, as discussed, there are still drawbacks and fabrication limitations for quartz resonators related to scaling for high-frequency applications. In addition, the material

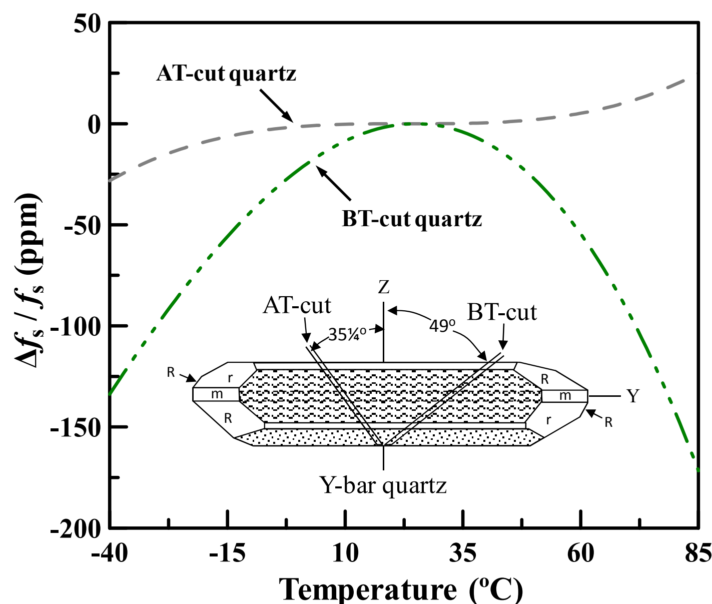

Figure 1-11. Frequency-temperature characteristics of AT- and BT-cut quartz resonators.

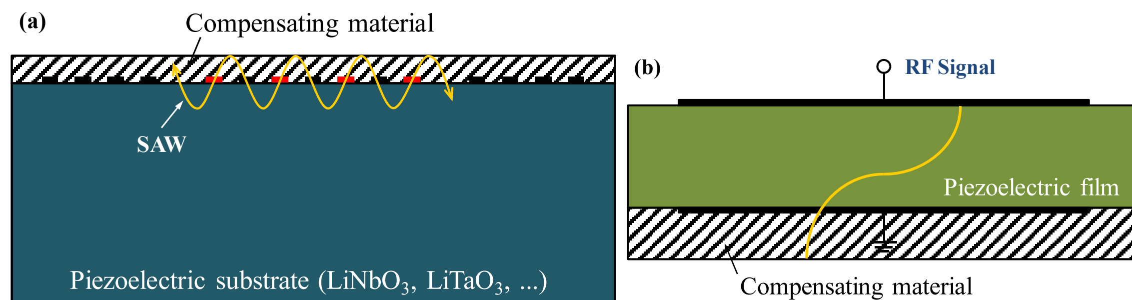

Figure 1-12. Illustrations of passive temperature compensation for (a) SAW and (b) BAW resonators.

property of quartz limits the integration of frequency references and CMOS circuits on a single chip. Although MEMS resonators have several advantages over crystal resonators, further improvement of the frequency-temperature stability is strongly demanded, especially for the narrow-band filters and reference oscillators.

1.4.1 Passive Temperature Compensation

Most materials, such as Si, AlN, or ZnO, become mechanically soft with an increasing temperature, giving negative temperature coefficients of elasticity (TCE); as a result, Si MEMS resonators exhibit a first-order TCF of approximately –31 ppm/°C [56]; AlN MEMS resonators, –25 ppm/°C; ZnO MEMS resonators, –60 ppm/°C [29]. This level of temperature stability is unsuitable for any frequency reference application. It is well-known that quartz is a crystalline form of SiO_2 and becomes mechanically stiff with an increasing temperature due to the positive temperature dependence of stiffness constants (i.e. C_{14} and C_{66}) and shows the existence of some temperature-insensitive cuts [57]. An amorphous SiO_2 layer also shows positive temperature dependence of elastic constants [58]. A passive thermal compensation technique using a compensating layer of SiO_2 has been widely applied to various Si-based electrostatic MEMS resonators [56] and piezoelectric resonators [55], [59]–[63].

Fig. 1–12 illustrates the passive temperature compensation technique for SAW and BAW resonators. By depositing a compensating thin film with an appropriate thickness, the first-order TCF can be reduced to zero at room temperature. Since the second-order TCEs of SiO_2 are not of positive temperature dependence [58], the second-order TCF would be still temperature dependent after passive temperature compensation. Except for SiO_2, tellurium dioxide (TeO_2) [64] and highly-doped Si [65], [66] layers were also used as the compensating material. Recently, fluorine-doped silicon oxide (SiOF) was found to have better temperature compensation efficiency than undoped SiO_2 films [67].

1.4.2 Active Temperature Compensation

Although AT-cut quartz resonators and temperature-compensated MEMS resonators can offer temperature stability lower than 100 ppm, which is still unsuitable for any reference

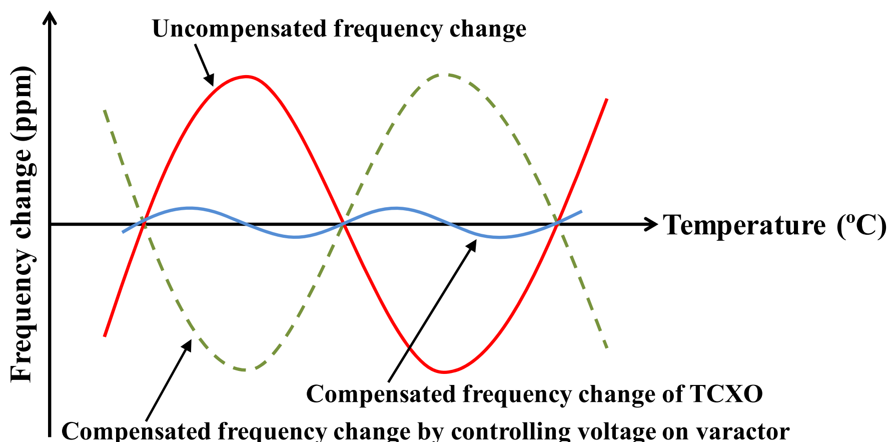

Figure 1-13. Principle of active temperature compensation of TCXOs.

oscillator application, the resonators must rely on additional temperature compensation techniques to achieve better frequency stability. One approach is to apply an electrostatic force to the resonator body via a direct current (DC) potential, causing a spring softening effect to adjust the resonance frequency [68], [69]. Another approach is to employ a temperature sensor to detect temperature changes and a compensation circuitry to minimize the temperature-induced frequency drifts. As shown in Fig. 1–13, TCXO is allowed for shifting the resonance frequency by adjusting the effective capacitance via applying a small correction voltage to a varactor diode. TCXO normally can offer excellent temperature stability with low power consumption and fast stabilization time.

In order to achieve a better degree of stability, for example, a more complicated circuitry is implemented in microcomputer compensated crystal oscillators (MCXOs) or a thermostatically controlled oven is implemented in OCXOs which are typically used for the highest precision frequency applications. Since the crystal and associated circuitry are heated to the upper turning point of crystal and a narrow temperature window needs to be maintained, the better frequency stability accompanies larger power consumption and longer stabilization time. Table 1–1 summarizes the performance of XO, TCXO, MCXO, and OCXO. The frequency-temperature stability of the resonators and reference oscillators is usually characterized over the temperature range from 0 to 70 °C, (commercial grade), –40 to 85 °C (industrial grade), or –55 to 125 °C (military grade).

Table 1-1. Performance comparison of common reference oscillators.

	XO	**TCXO**	**MCXO**	**OCXO**
Temperature stability over –40 to 85 °C (ppm)	10–100	1–10	0.01–0.1	0.001–0.01
Power (mW)	~1	~10	~100	~1000
Stabilization time (sec)	N/A	0.1–1	0.1–1	30–240
Size	~1x	~2x	~5x	~10x

1.5 Outline

This research work focuses on the development and characterization of temperature-compensated AlN LWRs utilizing the S_0 mode for frequency reference applications. As presented in Chapter 1, SiO_2 will be used for passive temperature compensation of AlN LWRs. Chapter 2 will discuss acoustic wave characteristics of Lamb wave modes propagating in an AlN thin plate and an AlN/SiO_2 composite plate. Chapter 3 will detail the frequency-temperature behaviors of an AlN/SiO_2 composite plate. Fine selection of the SiO_2 layer thickness for complete temperature compensation of AlN LWRs at room temperature will be included. In addition, the experimental results will be verified with the theoretical results. Chapter 4 will present and describe the microfabrication process of the AlN/SiO_2 LWRs. Finally, Chapter 5 will conclude this research work and suggest some potential future research directions.

Chapter 2

Lamb Wave Modes Propagating in Piezoelectric AlN Membranes and AlN/SiO$_2$ Composite Plates

Piezoelectric thin films, such as AlN, GaN, and ZnO, have been utilized in SAW filters as well as bulk acoustic resonators and filters for communication applications. There are two main factors for broad use of piezoelectric thin films: efficient electromechanical transduction and growth of high-quality piezoelectric films on a variety of substrates, such as Si, quartz, SiC, GaAs, and sapphire. With growing interests in high-frequency and high-Q resonators for millimeter-wave circuit applications, Lamb wave mode in a piezoelectric thin plate has drawn great attentions due to its high phase velocity. In this chapter, a study of the lowest-order Lamb wave modes (i.e. A_0 and S_0 modes) in an AlN plate and an AlN/SiO$_2$ composite plate is presented. Phase velocities, electromechanical coupling coefficients, and dispersion characteristics of Lamb waves will be included in the theoretical studies. The propagation properties of Lamb wave modes in piezoelectric media will be investigated in this chapter and then employed in designs of temperature-compensated AlN LWRs in the following chapter.

2.1 Why AlN Thin Film

Although PZT shows a strong piezoelectric coupling coefficient and has been used in MEMS devices for many years, its large acoustic losses and high dielectric constants limit its use in high-frequency applications [29]. III-V compounds such as AlN and GaN or II-VI compounds like ZnO are the most common piezoelectric thin films for high-frequency acoustic transducer applications. As illustrated in Fig. 2–1, AlN, GaN, and ZnO are all wurtzite-structured materials with *a*- and *c*-axis, belonging to hexagonal crystal system, with polarized direction along the *c*-axis (0001) which is usually normal to the substrate. The piezoelectric thin films can be synthesized and grown on substrates by using reactive sputtering, MOCVD, or molecular beam epitaxy (MBE). Since the deposition temperatures of MOCVD and MBE are usually higher than 800 °C, causing

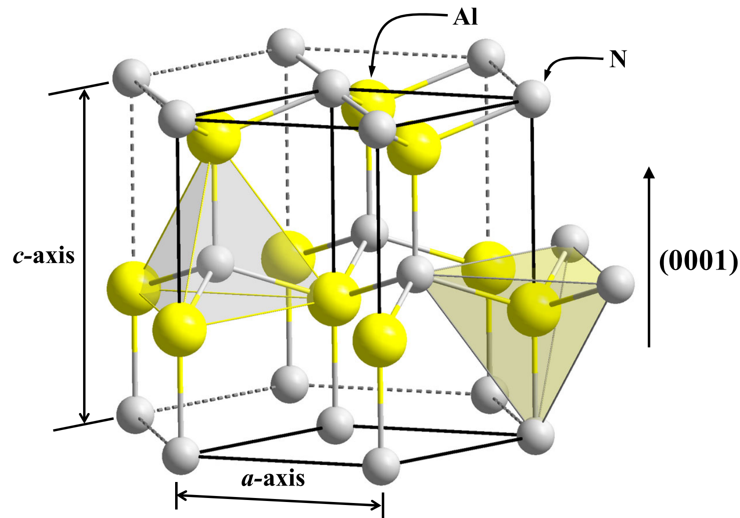

Figure 2-1. Hexagonal wurtzite crystal structure of AlN, GaN and ZnO.

some issues with post-deposition processes, reactive sputtering is greatly preferred due to the low deposition temperature below 400 °C.

Among common sputtered piezoelectric thin films, AlN is always considered a highly desirable thin film material for electroacoustic devices since it has high acoustic velocity, good thermal conductivity, large Young's modulus, moderate piezoelectric coupling coefficient, low acoustic loss, and relatively small TCF [70]–[74]. Table 2–1 compares

Table 2-1. Physical properties of ZnO, AlN, and GaN [29], [70]–[74].

	ZnO	AlN	GaN	Units
Density	5680	3260	6150	(kg/m^3)
Longitudinal acoustic wave velocity	~6350	~11300	~8050	(m/s)
Shear acoustic wave velocity	~2720	~6000	~4130	(m/s)
Lattice constant, a	3.249	3.112	3.189	(Å)
Lattice constant, c	5.207	4.982	5.186	(Å)
Thermal expansion (300 K), α_a	4.75	5.27	5.59	(10^{-6}/°C)
Thermal expansion (300 K), α_c	2.92	4.15	3.17	(10^{-6}/°C)
Piezoelectric coefficient, e_{15}	–0.48	–0.48	–0.33	(C/m^2)
Piezoelectric coefficient, e_{31}	–0.57	–0.58	–0.33	(C/m^2)
Piezoelectric coefficient, e_{33}	1.32	1.55	0.65	(C/m^2)
Electromechanical coupling coefficient, k_t^2	~8.5	~6.5	~1.2	(%)
Thermal conductivity	60	280	130	(W/mK)
TCF	–60	–25	–	(ppm/°C)

physical properties of ZnO, AlN, and GaN. Despite ZnO exhibits a slightly stronger electromechanical coupling coefficient (k^2) than AlN, its lower acoustic velocity, higher acoustic loss and larger TCF limits its applications on high-frequency acoustic devices. Therefore, AlN is selected for demonstration of temperature-compensated LWRs in this research work. In the following sections of this chapter, Lamb wave modes propagating in a piezoelectric AlN thin film and an AlN/SiO_2 composite plate will be theoretically investigated.

2.2 Theoretical Analysis of Lamb Wave Modes in an AlN Plate

The effective permittivity based on a transfer matrix is used to calculate the phase velocities of Lamb wave modes propagating in a piezoelectric thin plate [75]–[76]. The electromechanical coupling coefficient k^2 of Lamb waves excited by an IDT can be analyzed using an approximation method, which is based on the velocity difference under the free-surface and metalized-surface electrical boundary conditions [75]. The other approach for exact analysis of the k^2 of Lamb waves is the Green's function method [77]–[80]. In this section, the phase velocity and k^2 of the two fundamental Lamb wave modes propagating in an AlN thin plate will be theoretically analyzed. The k^2 calculated using the two above methods will be compared as well.

2.2.1 Transfer Matrix

Fig. 2–2 shows the geometry of the wave problem to be analyzed. Lamb wave modes propagate along the x-direction of a piezoelectric thin plate bounded by the planes $z = 0$ and h, respectively. The governing field equations of piezoelectricity can be expressed as

$$\sigma_{ij,j} = \rho \ddot{u}_i , \qquad (2.1)$$

$$D_{i,i} = 0 , \qquad (2.2)$$

where σ_{ij} and u_i denote the Cauchy stress tensor and the mechanical displacement,

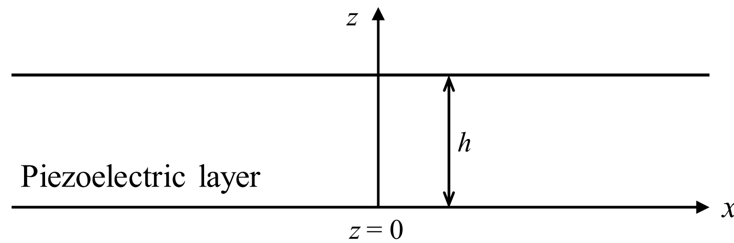

Figure 2-2. The coordinate system used in the theoretical analysis of a single piezoelectric layer.

respectively. ρ is the density and D_i is the electric displacement. The piezoelectric constitutive relations with the mechanical displacement u_i and electric potential ϕ as variables are of the form

$$\sigma_{ij} = c_{ijkl} u_{k,l} + e_{lij} \phi_{,l}, \tag{2.3}$$

$$D_i = e_{ikl} u_{k,l} - \varepsilon_{il} \phi_{,l}, \tag{2.4}$$

where c_{ijkl} is the elastic stiffness at constant electric field of the piezoelectric medium, e_{lij} is the piezoelectric constants, and ε_{il} is the dielectric constants at constant strain.

For plane harmonic wave propagating in the *x*-direction, the displacement vector $\mathbf{u}$, the *z*-component of the electric displacement vector D_z, the traction vector $\mathbf{t}$, and the electric potential ϕ are given by

$$\mathbf{u}(x, y, z) = \bar{\mathbf{u}}(z) \exp[i(\omega t - k_x x)], \tag{2.5}$$

$$D_z(x, y, z) = \bar{D}_z(z) \exp[i(\omega t - k_x x)], \tag{2.6}$$

$$\mathbf{t}(x, y, z) = \bar{\mathbf{t}}(z) \exp[i(\omega t - k_x x)], \tag{2.7}$$

$$\phi(x, y, z) = \bar{\phi}(z) \exp[i(\omega t - k_x x)], \tag{2.8}$$

where ω is the angular frequency and k_x is the *x*-component wave vector of the plane harmonic waves. According to the state vector formulation of acoustic elastic waves in anisotropic solids, the governing equations (2.1)–(2.4) can be rearranged in a matrix form as [76], [78]

$$\frac{d}{dz} \bar{\xi}(z) = -i\mathbf{N}(z) \cdot \bar{\xi}(z), \tag{2.9}$$

$$\bar{\xi}(z) = \begin{Bmatrix} \bar{\mathbf{u}}(z) \\ \bar{\phi}(z) \\ i\bar{\mathbf{t}}(z) \\ i\bar{D}_z(z) \end{Bmatrix}, \tag{2.10}$$

where $\bar{\xi}(z)$ is the state vector and **N**(*z*) is the fundamental acoustic tensor [81]. When the propagation medium is considered homogeneous, the tensor **N** is independent of *z*. Thus the solution of this differential equation system can be expressed as

$$\bar{\xi}(z)=\exp(-i\mathbf{N}z)\cdot\bar{\xi}(0)\,, \tag{2.11}$$

where $\exp(-i\mathbf{N}z)$ is called the transfer matrix and $\bar{\xi}\left(0\right)$ is the initial condition at z=0. It should be noted that this solution is appropriate for a layered system because the overall solution can be obtained by multiplication of the solutions of each layer. For multilayer media, the surface impedance approach can be adopted to avoid the numerical difficulties [81], [82]. Based on this approach, the generalized traction vector $\mathbf{T}=\left\{i\bar{\mathbf{t}}\left(z\right) \quad i\bar{D}_z\left(z\right)\right\}^T$ and the generalized displacement vector $\mathbf{U}=\left\{\bar{\mathbf{u}}\left(z\right) \quad \bar{\phi}\left(z\right)\right\}^T$ are defined at a plane normal to the z-axis. By using the eigenvalue-eigenvector decomposition of the transfer matrix, (2.11) can be rearranged in the following form

$$\begin{Bmatrix}\mathbf{U}\\ \mathbf{T}\end{Bmatrix}=\begin{bmatrix}\mathbf{A_1} & \mathbf{A_2}\\ \mathbf{L_1} & \mathbf{L_2}\end{bmatrix}\begin{bmatrix}\mathbf{\Phi_1} & \mathbf{0}\\ \mathbf{0} & \mathbf{\Phi_2}\end{bmatrix}\begin{Bmatrix}\mathbf{C_1}\\ \mathbf{C_2}\end{Bmatrix}, \tag{2.12}$$

where $\begin{bmatrix}\mathbf{A_1} & \mathbf{A_2}\\ \mathbf{L_1} & \mathbf{L_2}\end{bmatrix}$ is the matrix of eigenvalues of $\mathbf{N}$, which are arranged such that the first four eigenvalues of $\mathbf{N}$ correspond to waves decaying in the z-direction, and $\mathbf{A_1}$, $\mathbf{A_2}$, $\mathbf{L_1}$, $\mathbf{L_2}$ are 4×4 matrices. $\mathbf{C_1}$ and $\mathbf{C_2}$ are constant vectors which are related to the initial condition at z = 0. The diagonal matrices are

$$\mathbf{\Phi_1}=\mathrm{diag}(e^{-ik_{z1}z}, e^{-ik_{z2}z}, e^{-ik_{z3}z}, e^{-ik_{z4}z})\,, \tag{2.13}$$

$$\mathbf{\Phi}_2=\mathrm{diag}(e^{-ik_{z5}z}, e^{-ik_{z6}z}, e^{-ik_{z7}z}, e^{-ik_{z8}z})\,, \tag{2.14}$$

with k_{zi} the eigenvalues of $\mathbf{N}$. With the above arrangement of the transfer matrix, the surface impedance tensor of the layered piezoelectric medium can be defined as [78], [81]

$$\mathbf{T}=i\omega\mathbf{G}\mathbf{U}\,, \tag{2.15}$$

where the surface impedance tensor $\mathbf{G}$ is a 4×4 matrix. The recursive formulas of $\mathbf{G}$ for layered media are then given by

$$\mathbf{G}_j=\left[\mathbf{Z}_{1j}\mathbf{W}_{1j}\left(z\right)\mathbf{R}_{j-1}\mathbf{W}_{2j}^{-1}+\mathbf{Z}_{2j}\right]\left[\mathbf{W}_{1j}\left(z\right)\mathbf{R}_{j-1}\mathbf{W}_{2j}^{-1}+\mathbf{I}\right]^{-1}, \tag{2.16}$$

$$\mathbf{Z}_{\alpha j}=-\frac{1}{\omega}\mathbf{L}_{\alpha j}\mathbf{A}_{\alpha j}^{-1}, \tag{2.17}$$

$$\mathbf{W}_{\alpha j}=\mathbf{A}_{\alpha j}\mathbf{\Phi}_{\alpha j}\mathbf{A}_{\alpha j}^{-1}, \tag{2.18}$$

$$\mathbf{R}_{j-1} = \left[\mathbf{Z}_{1j} - \mathbf{G}_{j-1}\right]^{-1}\left[\mathbf{G}_{j-1} - \mathbf{Z}_{2j}\right], \tag{2.19}$$

where j=1 represents the non-piezoelectric membrane and j=2 represents the piezoelectric membrane. $\mathbf{Z}_{\alpha j}$ are local impedances for the up-going wave and the down-going wave. $\alpha = 1$ represents decaying waves in the positive z-direction (up-going), and $\alpha = 2$ represents decaying waves in the negative z-direction (down-going).

2.2.2 Boundary Conditions

Generally speaking, two types of electrode arrangements for a single piezoelectric plate are considered and shown in Fig. 2–3. Type A device is a single piezoelectric membrane with IDTs deposited on the top surface combined with a non-metallizd (i.e. free or open-circuited) bottom surface and type B device has IDTs on the top surface in conjunction with a metallized (i.e. short-circuited) bottom surface. For the type A device, in order to satisfy the boundary conditions of the bottom surface at $z = 0$, which include traction free and continuity of the normal electric displacement, the surface impedance tensor $\mathbf{G_0}$ of the bottom surface can be expressed as

$$\mathbf{G_0} = \begin{bmatrix} \mathbf{0} & \mathbf{0} \\ \mathbf{0} & -i\varepsilon_0 k_x \end{bmatrix}, \tag{2.20}$$

where ε_0 is the vacuum permittivity and the Laplace equation of the electric potential in the vacuum has been satisfied. For the type B device, to satisfy the boundary conditions of the bottom surface at $z = 0$, which include traction free and zero potential, the surface

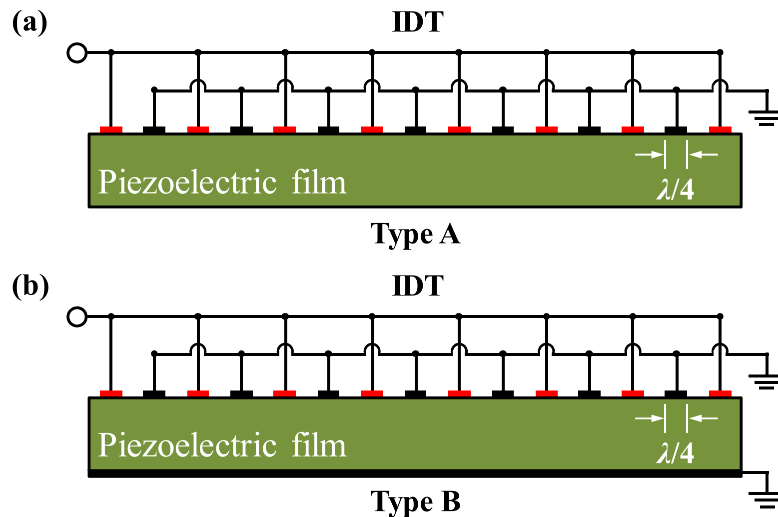

Figure 2-3. Cross-sectional illustrations of two electrode arrangements of LWRs: (a) free bottom surface and (b) metallized bottom surface.

impedance tensor $\mathbf{G_0}$ of the bottom surface can be expressed as

$$\mathbf{G_0} = \mathbf{0}\,. \tag{2.21}$$

2.2.3 Effective Permittivity and Phase Velocity

In order to conveniently define the effective permittivity, the surface impedance tensor $\mathbf{G}_j$ in (2.16) can be rearranged in the form

$$\mathbf{G}_j = \begin{bmatrix} \mathbf{G}_m & \mathbf{g}_{T\phi} \\ \mathbf{g}_{DU}^T & g_{D\phi} \end{bmatrix}, \tag{2.22}$$

where $\mathbf{G}_m$ is a 3×3 matrix representing the mechanical part of $\mathbf{G}_j$. $\mathbf{g}_{T\phi}$ and $\mathbf{g}_{DU}^T$ are 3×1 vectors standing for the electromechanical coupling terms of $\mathbf{G}_j$ where $\mathbf{g}_{T\phi}$ is the coupling between the traction and the electric potential, and $\mathbf{g}_{DU}^T$ is the coupling between electric displacement and particle displacement. The superscript "T" in $\mathbf{g}_{DU}^T$ denotes the transpose. The scalar $g_{D\phi}$ relates the electric potential to the electric displacement. Equation (2.15) can be expanded as

$$i\bar{\mathbf{t}} = i\omega\left[\mathbf{G}_m\bar{\mathbf{u}} + \mathbf{g}_{T\phi}\bar{\phi}\right], \tag{2.23}$$

$$i\bar{D}_z = i\omega\left[\mathbf{g}_{DU}^T\bar{\mathbf{u}} + \mathbf{g}_{D\phi}\bar{\phi}\right], \tag{2.24}$$

Since the tractions on the top surface are vanishing, the electric displacement at $z = h$ in the solid side is denoted as $\bar{D}_z\big|_{z=h^-}$ and is given by

$$\bar{D}_z\big|_{z=h^-} = \omega(-\mathbf{g}_{DU}^T\mathbf{G}_m^{-1}\mathbf{g}_{T\phi} + \mathbf{g}_{D\phi})\,\bar{\phi}\big|_{z=h^-}\,. \tag{2.25}$$

In the vacuum side, $z > h$, the electric potential should satisfy the Laplace equation. The normal electric displacement $\bar{D}_z\big|_{z=h^+}$ at $z = h$ in the vacuum side is given by

$$\bar{D}_z\big|_{z=h^+} = \varepsilon_0 k_x\,\bar{\phi}\big|_{z=h^+}\,. \tag{2.26}$$

The effective permittivity at the interface between the vacuum and the piezoelectric membrane can then be written as

$$\varepsilon_s = \frac{\bar{D}_z\big|_{z=h^+} - \bar{D}_z\big|_{z=h^-}}{k_x\,\bar{\phi}\big|_{z=h}} = \varepsilon_0 - \frac{\omega}{k_x}(-\mathrm{g}_{DU}^T \mathrm{G}_m^{-1} \mathrm{g}_{T\phi} + \mathrm{g}_{D\phi}), \tag{2.27}$$

where the continuity of the electric potential at the interface has been employed.

Two sets of AlN stiffness constants are widely used in theoretical analysis as listed in Table 2–2 [60], [71], [83]. In this work, the AlN stiffness constants reported in [71] are employed in the simulation. Fig. 2–4 shows effective permittivity of an AlN membrane with the free bottom surface while the AlN thin film thickness (h_{AlN}) is 1 μm, the wavelength (λ) corresponds to 12 μm, and the phase velocity is within 12000 m/s. In the Fig. 2–4, the solid line represents the real part of effective permittivity and the dashed line represents the imaginary part. The effective permittivity values of the Lamb wave modes are real in this case, indicating that Lamb waves would not attenuate since most surfaces of the AlN Lamb wave resonator are in contact with air. There are two poles and two zeros showed in Fig. 2–4 where the zeros are corresponding to Lamb wave mode solutions for a free top surface due to the zero charge density whereas the poles indicate Lamb wave mode solutions for a metallized top surface because it gives a finite charge density and a zero electric potential.

In general, Lamb wave modes only have displacements in the *x*- and *z*-directions in Fig. 2–2 so they are usually sorted into antisymmetric and symmetric modes according to their unique displacement fields. It is well-known that antisymmetric Lamb wave modes exhibits antisymmetic *x*-displacements and symmertric *z*-displacements and symmetric Lamb wave modes shows symmetic *x*-displacements and antisymmertric *z*-displacements [54]. According to the displace profiles illustrated in Fig. 2–5, the first Lamb wave mode observed in Fig. 2–4 is called the lowest-order antisymmetric (A_0) mode and the second

Table 2-2. Material constants of Al, SiO_2, and AlN used in the calculation.

	Symbol	Al [60]	SiO_2 [60]	AlN [71]	AlN [83]	Units
Stiffness constants	C_{11}	1.113	0.785	3.45	4.105	(10^{11} N/m^2)
	C_{12}	0.591	0.161	1.25	1.485	
	C_{13}	0.591	0.161	1.2	0.989	
	C_{33}	1.113	0.785	3.95	3.885	
	C_{44}	0.261	0.312	1.18	1.246	
	C_{66}	0.261	0.312	1.1	1.31	
Mass density	ρ	2700	2200	3260	3255	(kg/m^3)
Piezoelectric constants	e_{15}	–	–	–0.48		(C/m^2)
	e_{31}	–	–	–0.58		
	e_{33}	–	–	1.55		
Dielectric constants	ε_{13}	1	3.32	8.0		(10^{-11} F/m)
	ε_{33}	1	3.32	9.5		

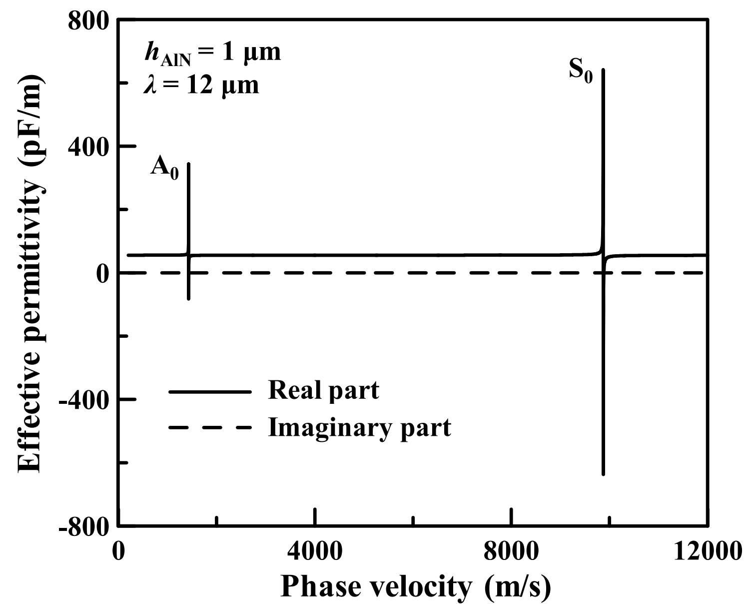

Figure 2-4. The effective permittivity of an AlN membrane with free bottom surface while AlN thickness (h_{AlN}) is 1 μm and the wavelength (λ) corresponds to 12 μm.

Lamb wave mode is called the lowest-order symmetric (S_0) mode.

When the thickness of the piezoelectric thin film is comparable to the wavelength, the acoustic wave propagation properties are dispersive with respect to the thickness of the piezoelectric layer. Fig. 2–6 shows the simulated phase velocity dispersion of the first two Lamb wave modes propagating in an AlN membrane with free top and bottom surfaces, which were calculated using the transfer matrix. The S_0 Lamb wave mode shows a phase velocity in excess of 9800 m/s which is close to the phase velocity of BAW, and it exhibits much weaker phase velocity dispersion than the A_0 Lamb wave mode. The high phase velocity of the S_0 mode in an AlN plate is highly suitable for high-

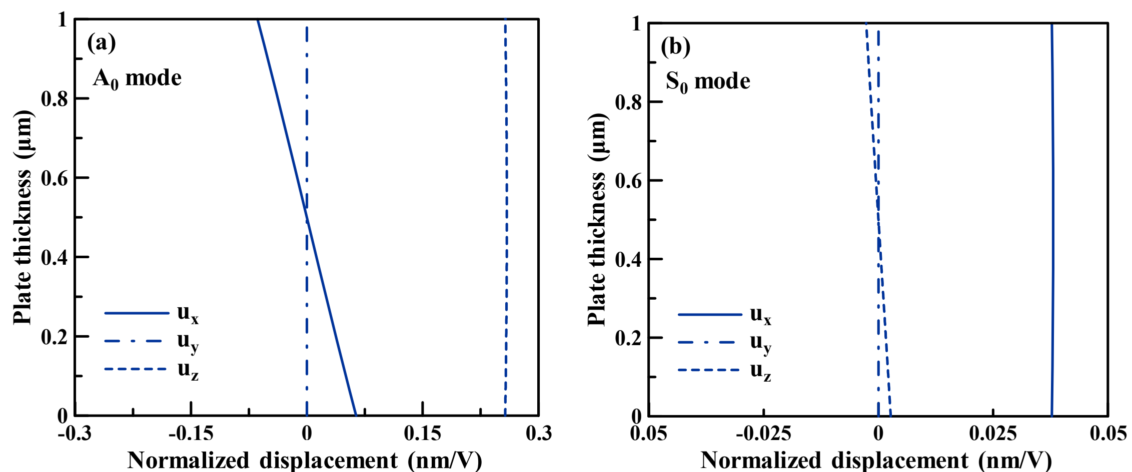

Figure 2-5. Normalized displacement profiles to surface potentials of the (a) A_0 and (b) S_0 Lamb wave modes in a 1-μm-thick AlN plate.

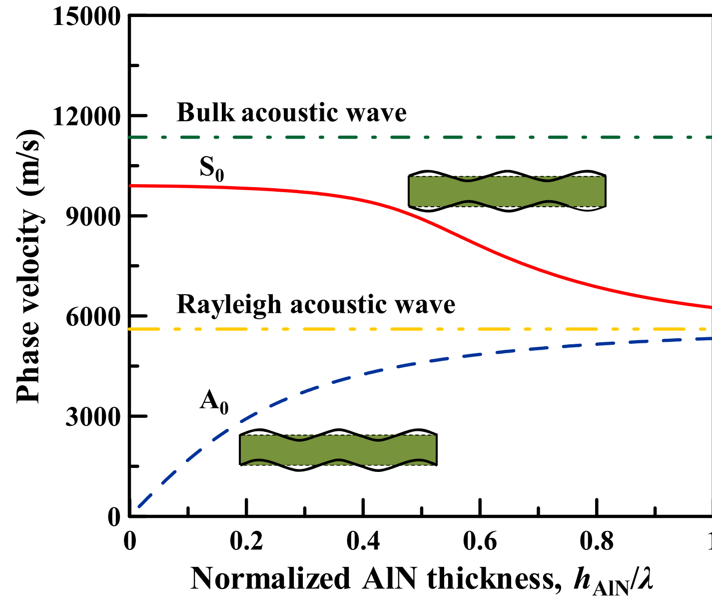

Figure 2-6. Simulated phase velocities of the first two Lamb wave modes propagating in an AlN plate.

frequency devices and the weak phase velocity dispersion is desirable since its resonance frequency is more insensitive to variations of AlN thin film thickness during AlN thin film deposition. In addition, both the phase velocities of the A_0 and S_0 Lamb wave modes are close to that of Rayleigh mode while the normalized AlN thickness (h_{AlN}/λ) approaches to 1.

2.2.4 Electromechanical Coupling Coefficient

After the extraction of the free velocity (v_o) and metallized velocity (v_m) from the zero and pole of the effective permittivity, the intrinsic k^2 of each Lamb wave mode can be easily evaluated by the velocity difference equation,

$$k^2 \cong \frac{v_o^2 - v_m^2}{v_o^2} \cong \frac{2(v_o - v_m)}{v_o}. \tag{2.28}$$

For more exact simulations, the Green's function method can be adopted to calculate the k^2 in the piezoelectric membrane [78], [82],

$$k^2 = -2\Gamma_s \varepsilon_s^{(\infty)}. \tag{2.29}$$

where $\varepsilon_s^{(\infty)}$ is the effective permittivity at infinite slowness and Γ_s is a coupling parameter. Fig. 2–7 shows the k^2 of the A_0 and S_0 modes based on the two configurations illustrated in Fig. 2–3. The simulation indicates the S_0 mode usually exhibits a larger k^2 than the A_0 mode for both configurations. Without the metalized backside, the k^2 of the S_0 mode is

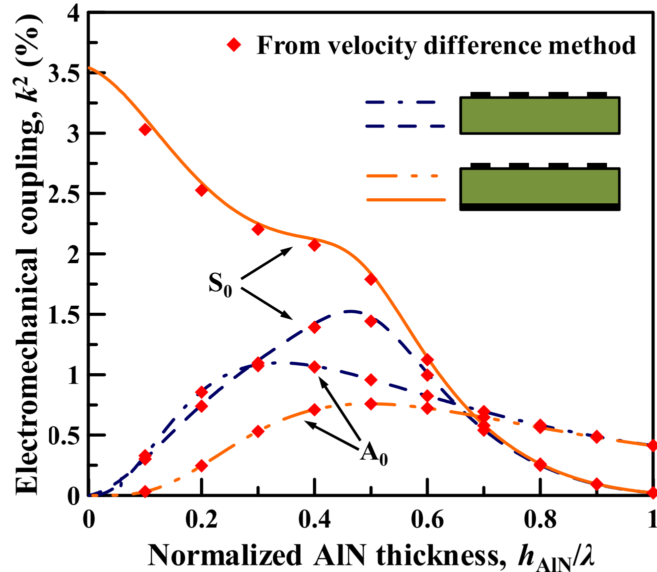

Figure 2-7. Comparison of k^2 computed from the Green's function with the velocity difference method.

limited to about 1.5%. By adding a bottom electrode beneath the AlN thin film, the k^2 can be increased to about 3.5%. This can be understood by considering an electric field applied between two IDT electrodes with a pitch of $\lambda/2$ on an AlN plate and another electric field through the AlN plate is generated by the backside metallization, enhancing the k^2. In addition, the k^2 of the unwanted A_0 mode with a low phase velocity has a comparable coupling strength and will appear as a spurious mode in the frequency spectrum. Fortunately, the conductive layer on the backside of the AlN thin film not only boosts the coupling of the S_0 mode but also reduces the coupling strength of the unwanted A_0 mode. Moreover, it is interesting to compare the intrinsic k^2 of the A_0 and S_0 modes obtained from the two approaches and they show agreement with each other.

2.3 Lamb Wave Modes in an AlN/SiO_2 Composite Plate

Similar to FBARs and SMRs using AlN thin films, the uncompensated LWR also has a first-order TCF of –20 to –30 ppm/°C [60]–[62]. This level of temperature stability is acceptable for frequency reference applications. It is well-known that the temperature-dependent frequency variation mainly results from material softening of the mechanical structures when the environment temperature increases. A temperature compensation technique using a layer of SiO_2 has been widely applied to different kinds of piezoelectric resonators [59]–[63] and Si-based electrostatic MEMS resonators [56]. Therefore, it is required to analyze the wave propagation properties of Lamb waves in a multilayer plate. Fig. 2–8 shows the geometry of the wave problem for a composite layer to be analyzed. Lamb wave modes propagate along the *x*-direction of a non-piezoelectric plate bounded by the planes z = 0 and H, and another piezoelectric layer bounded by the planes z = H

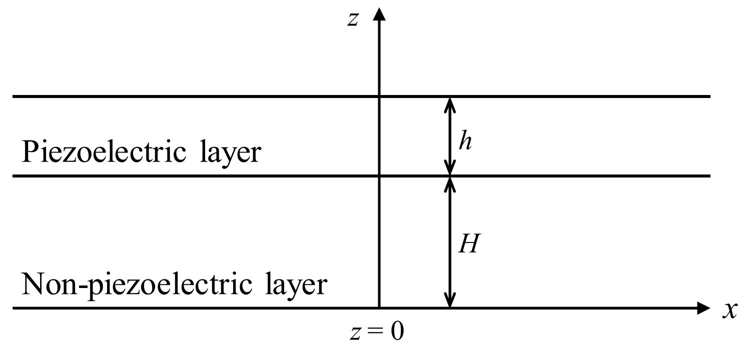

Figure 2-8. The coordinate system used in the analysis of a multilayer plate.

and H+h, respectively. As mentioned above, the transfer matrix is appropriate for a layered system because the overall solution can be obtained by the multiplication of the solutions of each layer. The only difference between the single layer and the composite plate is the boundary conditions.

2.3.1 Boundary Conditions and Effective Permittivity

In a multilayer plate, four types of electrode arrangements are considered as shown in Fig. 2–9. In the composite plate, the IDTs are deposited on the top surface of the piezoelectric thin film and the interface can be either electrically free or metalized. Moreover, the IDTs can be deposited at the interface and the top surface of the piezoelectric layer can be

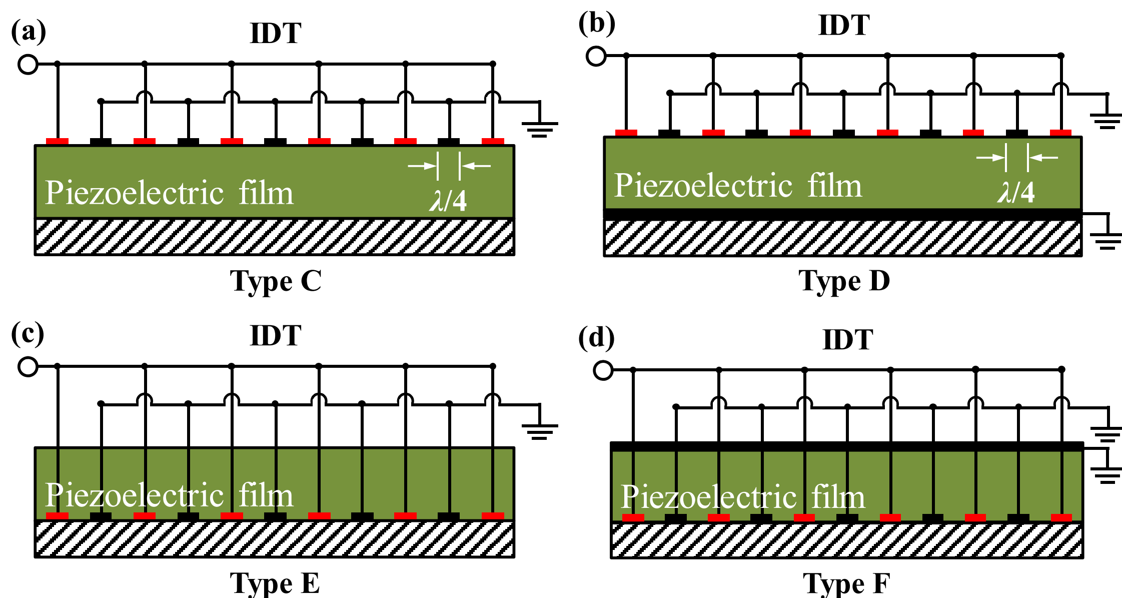

Figure 2-9. Cross-sectional illustrations of four electrode arrangements of composite LWRs: (a) free interface, (b) metallized interface, (c) free top surface, and (d) metallized top surface.

either electrically free or metallized. The metallization means zero potential and no mechanical loading in this work. For the four types of electrode arrangements, to satisfy the boundary conditions of the bottom surface at $z=0$ which include traction free and continuity of normal electric displacement, the surface impedance tensor $\mathbf{G}_0$ of the bottom surface is the same as (2.20).

In the layered structure of type C in Fig. 2–9, the boundary conditions of the interface at $z=H$ are continuous, so the recursive formulas can be employed directly. However, for the type D device, to satisfy the boundary conditions of the interface at $z=H$ which include the continuity of the traction and displacement as well as the zero potential, the surface impedance tensor $\mathbf{G}_1$ of the interface can be expressed as [79]

$$\mathbf{G}_1=\begin{bmatrix}\mathbf{G}_m & \mathbf{0}\\ \mathbf{0} & 0\end{bmatrix}. \tag{2.30}$$

Since the tractions on the top surface are vanishing for the both cases, the normal electric displacement at $z=H+h$ in the solid side is denoted as $\bar{D}_z\big|_{z=(H+h)^-}$ and can be given by

$$\bar{D}_z\big|_{z=(H+h)^-}=\omega\left(-\mathbf{g}_{DU}^{-1}\mathbf{G}_m^{-1}\mathbf{g}_{T\phi}+g_{D\phi}\right)\bar{\phi}\big|_{z=(H+h)^-}. \tag{2.31}$$

In the vacuum side (i.e. $z>H+h$), the electric potential satisfies the Laplace equation. The normal electric displacement $\bar{D}_z\big|_{z=(H+h)^+}$ at $z=H+h$ in the vacuum side is given by

$$\bar{D}_z\big|_{z=(H+h)^+}=\varepsilon_0 k_x\bar{\phi}\big|_{z=(H+h)^+}. \tag{2.32}$$

The effective permittivity at the top surface can then be written as

$$\varepsilon_s=\frac{\bar{D}_z\big|_{z=(H+h)^+}-\bar{D}_z\big|_{z=(H+h)^-}}{k_x\bar{\phi}\big|_{z=(H+h)}}=\varepsilon_0-\frac{\omega}{k_x}\left(-\mathbf{g}_{DU}^{T}\mathbf{G}_m^{-1}\mathbf{g}_{T\phi}+g_{D\phi}\right), \tag{2.33}$$

where the continuity of the electric potential on the top surface has been employed.

For the type E device in Fig. 2–9, to satisfy the boundary conditions of the top surface at $z=H+h$, which include traction free and continuity of normal electric displacement, the surface impedance tensor $\mathbf{G}_2$ of the top surface can be expressed as [79]

$$\mathbf{G}_2=\begin{bmatrix}\mathbf{0} & \mathbf{0}\\ \mathbf{0} & i\varepsilon_0 k_x\end{bmatrix}. \tag{2.34}$$

where the Laplace equation of the electric potential in the vacuum has been satisfied. However, in the layered structure of type F, to satisfy the boundary conditions of the top

surface at $z = H + h$, which include the traction free and zero potential, the surface impedance tensor $\mathbf{G}_2$ of the top surface can be expressed as [79]

$$\mathbf{G}_2 = \mathbf{0}. \tag{2.35}$$

At the interface of the two layered plates, the relation between the generalized traction vector and the displacement vector at $z = H^+$ in the piezoelectric membrane side can be expressed as

$$\begin{Bmatrix} i\bar{\mathbf{t}} \\ i\bar{D}_z \end{Bmatrix}\Bigg|_{z=H^+} = i\omega\mathbf{G}\begin{Bmatrix} \bar{\mathbf{u}} \\ \bar{\phi} \end{Bmatrix}\Bigg|_{z=H^+} = i\omega\begin{bmatrix} \mathbf{G}_m^+ & \mathbf{g}_{T\phi}^+ \\ \mathbf{g}_{DU}^{T+} & g_{D\phi}^+ \end{bmatrix}\begin{Bmatrix} \bar{\mathbf{u}} \\ \bar{\phi} \end{Bmatrix}\Bigg|_{z=H^+}, \tag{2.36}$$

and at $z = H^-$ in the non-piezoelectric membrane side, the generalized traction vector and the displacement vector can be expressed as

$$\begin{Bmatrix} i\bar{\mathbf{t}} \\ i\bar{D}_z \end{Bmatrix}\Bigg|_{z=H^-} = i\omega\mathbf{G}^-\begin{Bmatrix} \bar{\mathbf{u}} \\ \bar{\phi} \end{Bmatrix}\Bigg|_{z=H^-} = i\omega\begin{bmatrix} \mathbf{G}_m^- & \mathbf{g}_{T\phi}^- \\ \mathbf{g}_{DU}^{T-} & g_{D\phi}^- \end{bmatrix}\begin{Bmatrix} \bar{\mathbf{u}} \\ \bar{\phi} \end{Bmatrix}\Bigg|_{z=H^-}. \tag{2.37}$$

Since the tractions, mechanical displacement, and electric potential at the interface $z = H$ are continuous, the z-component of the electric displacements on the both sides of the interface are therefore given by

$$\bar{D}_z\Big|_{z=H^+} = \omega\left[\mathbf{g}_{DU}^{T+}\left(\mathbf{G}_m^- - \mathbf{G}_m^+\right)^{-1}\left(\mathbf{g}_{T\phi}^+ - \mathbf{g}_{T\phi}^-\right) + g_{D\phi}^+\right]\bar{\phi}\Big|_{z=H}, \tag{2.38}$$

$$\bar{D}_z\Big|_{z=H^-} = \omega\left[\mathbf{g}_{DU}^{T-}\left(\mathbf{G}_m^- - \mathbf{G}_m^+\right)^{-1}\left(\mathbf{g}_{T\phi}^+ - \mathbf{g}_{T\phi}^-\right) + g_{D\phi}^-\right]\bar{\phi}\Big|_{z=H}. \tag{2.39}$$

Accordingly, the effective permittivity at the interface can be written as

$$\varepsilon_s = \frac{\bar{D}_z\big|_{z=H^+} - \bar{D}_z\big|_{z=H^-}}{k_x\,\bar{\phi}\big|_{z=H}} = \frac{\omega}{k_x}\left[\left(\mathbf{g}_{DU}^{T+} - \mathbf{g}_{DU}^{T-}\right)\left(\mathbf{G}_m^- - \mathbf{G}_m^+\right)^{-1}\left(\mathbf{g}_{T\phi}^+ - \mathbf{g}_{T\phi}^-\right) + g_{D\phi}^{T+} - g_{D\phi}^{T-}\right]. \tag{2.40}$$

Fig. 2–10 shows the effective permittivity of an AlN/SiO_2 multilayer plate with the electrically free interface while the h_{AlN} is 1 μm, the SiO_2 layer thickness ($h_{\mathrm{SiO_2}}$) is 0.8 μm, the wavelength λ corresponds to 12 μm, and the phase velocity range is within 12000 m/s. In Fig. 2–10, the solid line represents the real part of effective permittivity and the dashed line represents the imaginary part. There are two poles and two zeros in Fig. 2–10 where the zeros are corresponding to the Lamb wave mode solutions for a free top surface due to the zero charge density whereas the poles indicate the Lamb wave mode solutions for a metallized top surface of the AlN thin film because it gives a finite charge density and a zero electric potential.

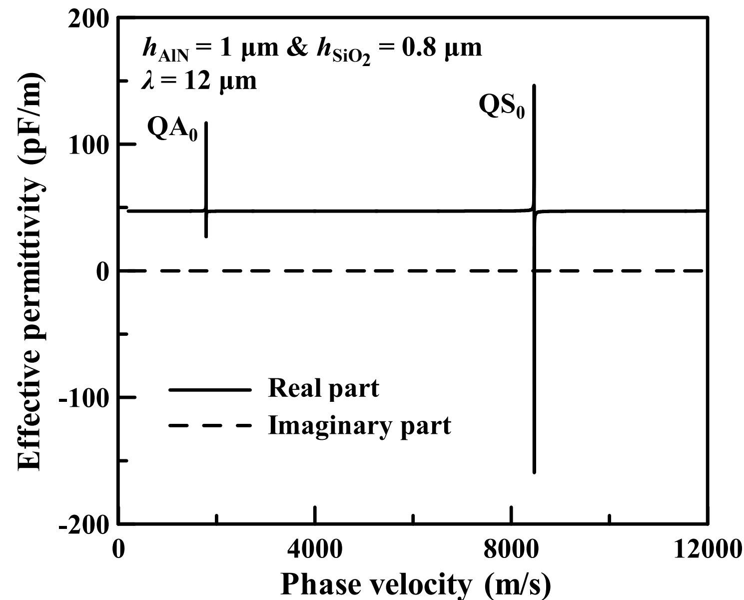

Figure 2-10. The effective permittivity of an AlN/SiO_2 membrane with free interface while h_{AlN} is 1 µm, h_{SiO_2} is 0.8 µm, and the wavelength λ corresponds to 12 µm.

As discussed above, Lamb waves are sorted into antisymmetric and symmetric modes according to their unique displacement fields. However, the different material properties of the AlN and SiO_2 layers make the Lamb wave displacement profiles no longer simply antisymmetric or symmetric with respect to the neutral axis. As shown in Fig. 2–11, when the 0.8-µm-thick SiO_2 layer is attached to the 1-µm-thick AlN plate, the normalized displacement profiles to the surface potentials of the Lamb wave modes are distorted. It is noted that the SiO_2 layer exhibits larger displacement profiles for both plate acoustic modes because SiO_2 has lower acoustic impedance than AlN [29], [84]. In this work, as a result, the plate acoustic wave modes in the multilayer plate are classified as quasi-Lamb

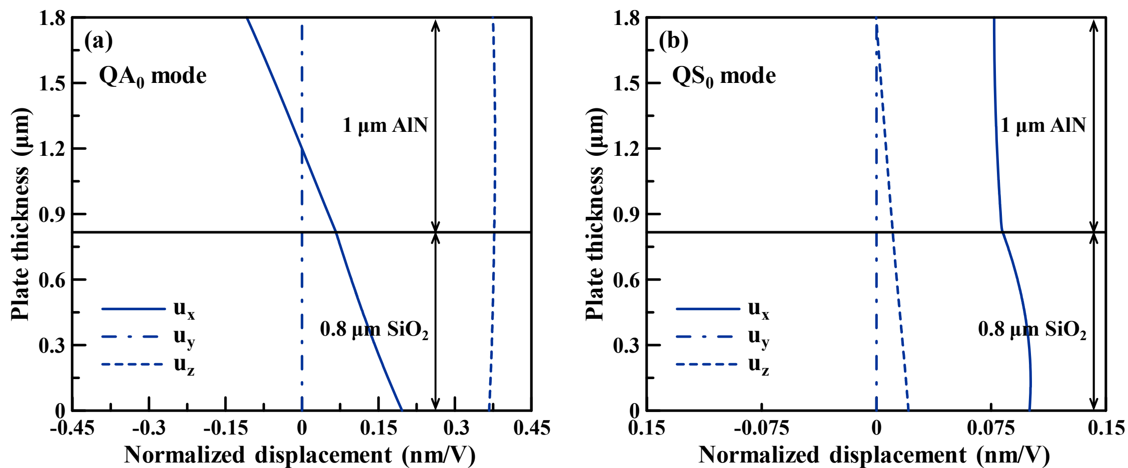

Figure 2-11. Normalized displacement profiles to surface potentials of the (a) QA_0 and (b) QS_0 Lamb wave modes in an AlN/SiO_2 multilayer plate while h_{AlN} is 1 µm and h_{SiO_2} equals 0.8 µm.

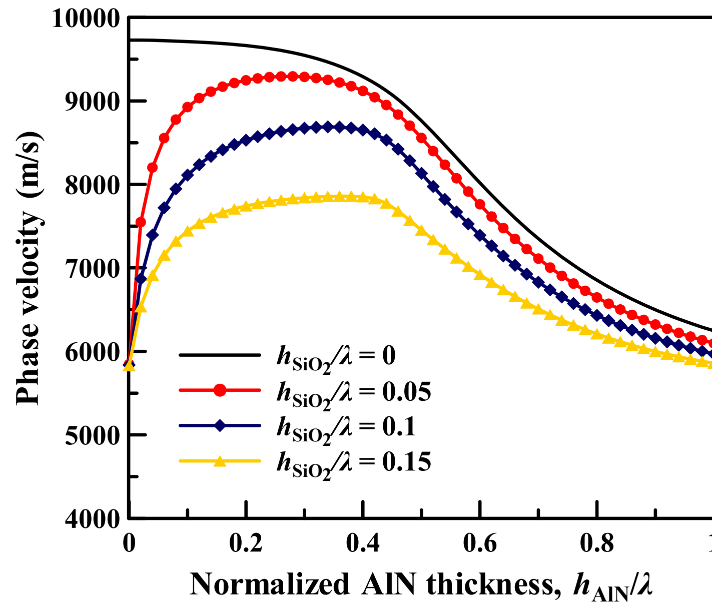

Figure 2-12. Simulated phase velocity dispersion of the QS_0 Lamb wave mode for h_{SiO_2}/λ equal to 0, 0.05, 0.1, and 0.15, respectively.

wave modes [7]. According to the displace profiles in Fig. 2–11, the first acoustic wave mode in Fig. 2–10 is called the lowest-order quasi-antisymmetric (QA_0) mode and the second acoustic wave mode is called the lowest-order quasi-symmetric (QS_0) mode.

2.3.2 Phase Velocity

Since the S_0 mode shows the higher phase velocity and larger k^2 than the A_0 mode in an AlN thin plate, only the QS_0 mode will be investigated in the AlN/SiO_2 composite layer. Similar to Lamb wave modes in an AlN layer, while the thicknesses of the piezoelectric thin film and the non-piezoelectric layer are comparable to the wavelength, the acoustic wave propagation properties are dispersive with respect to the thicknesses of the two layers. Fig. 2–12 shows the simulated phase velocity dispersions of the QS_0 mode propagating in an AlN/SiO_2 membrane with the free top surface and interface while the h_{SiO_2}/λ varies from 0 to 0.15 with a step of 0.05. The QS_0 mode shows the phase velocity decreased with the increasing SiO_2 thickness because SiO_2 has smaller material stiffness coefficients and lower acoustic velocities than AlN. The QS_0 mode in the AlN/SiO_2 composite layer exhibits a larger phase velocity while the h_{AlN}/λ approaches to 0.3.

2.3.3 Electromechanical Coupling Coefficient

The k^2 of the QS_0 mode in the AlN/SiO_2 composite plate is evaluated using the velocity difference method. Fig. 2–13 shows the k^2 of the LWRs using the QS_0 mode with the four configurations in Fig. 2–9 while the h_{SiO_2} is equal to 0.1λ. For the h_{AlN}/λ thinner than 0.4, the type D device using the QS_0 mode exhibits larger k^2 than the other configurations

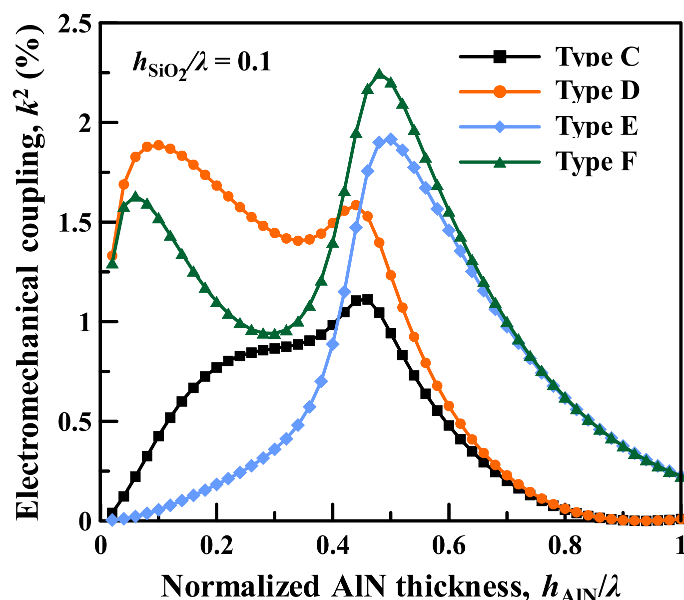

Figure 2-13. Comparison of k^2 of various types of AlN/SiO_2 LWRs while the h_{SiO_2} is equal to 0.1λ.

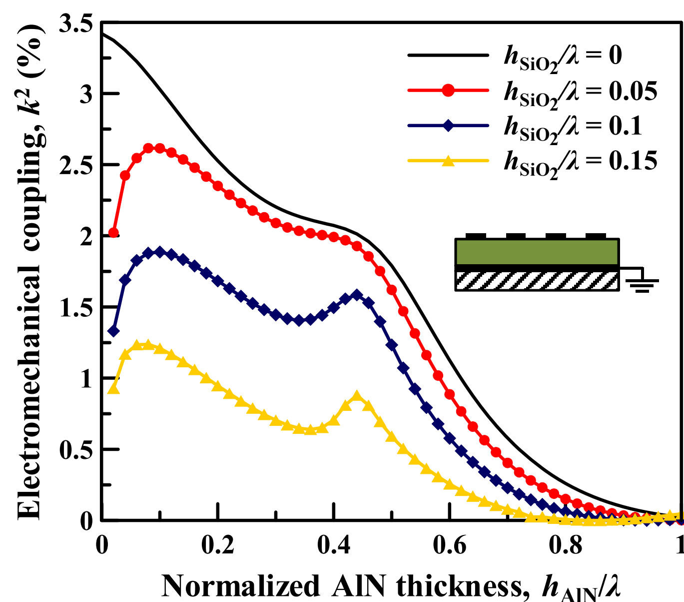

Figure 2-14. Simulated k^2 of the type D device utilizing the QS_0 mode for h_{SiO_2}/λ equal to 0, 0.05, 0.1, and 0.15, respectively.

so the type D configuration is desired for the temperature-compensated AlN/SiO_2 LWR studied in this work. Fig. 2–13 illustrates the k^2 dispersion of the type D device for the h_{SiO_2}/λ equal to 0, 0.05, 0.1, and 0.15, respectively. Under the type D configuration, for various SiO_2 thicknesses, the QS_0 Lamb wave mode exhibits a maximum k^2 while the h_{AlN} is around 0.1λ which is desirable for cost-effective AlN/SiO_2 LWRs since only a thinner AlN thickness is required to achieve a larger k^2.

Chapter 3

Temperature-Compensated LWRs on AlN/SiO_2 Composite Plates

Given that AlN becomes mechanically soft with an increasing temperature due to its negative TCEs, micromechanical AlN resonators usually show a first-order TCF of approximately –25 ppm/°C. Amorphous SiO_2 is well-known for its positive temperature dependence of elastic constants [58] and a passive thermal compensation technique using SiO_2 has been widely applied to different types of piezoelectric resonators [55], [59]–[63]. In this chapter, the TCF characteristics of the S_0 Lamb wave mode in an AlN plate and the QS_0 mode in an AlN/SiO_2 composite plate will be theoretical analyzed. A zero first-order TCF can be achieved in the AlN/SiO_2 composite plate using an appropriate thickness ratio of AlN to SiO_2. In addition, from the simulated results, near zero first-order TCFs over a wide frequency range from 100 MHz to 1000 MHz can be achieved simultaneously based on the same AlN/SiO_2 stack while the AlN film is deposited as thin as 250 nm. Finally, a temperature-compensated LWR utilizing the QS_0 Lamb wave mode was successfully fabricated on the AlN/SiO_2 plate composed of 1-µm-thick AlN and 0.83-µm-thick SiO_2. An AlN LWR operating at 711 MHz is completely compensated at its turnover temperature, 18.05 °C, and exhibits a zero first-order TCF, a small second-order TCF of –21.5 ppb/°C^2, a low motional resistance of 150 Ω, an effective coupling coefficient k^2_{eff} of 0.56%, and a quality factor Q of 980.

3.1 Electrode Metallization Selection for AlN LWRs

A bottom electrode beneath the AlN thin film usually can improve the k^2 of the S_0 mode since the metallized bottom surface strongly enhances the vertical electric field in the piezoelectric AlN thin film as observed in Fig. 2–7. Fig. 3–1 illustrates the one-port LWR consisting of one IDT, a grounded bottom electrode, and two suspended free edges at both sides of the AlN thin plate. Since the AlN thin films are grown onto the substrates using AC reactive magnetron sputtering, the AlN thin film quality heavily depends on the metal properties [85]. So far high-quality AlN films have been successfully deposited on various substrates [29], [86], [87]. Generally speaking, the surface temperature during

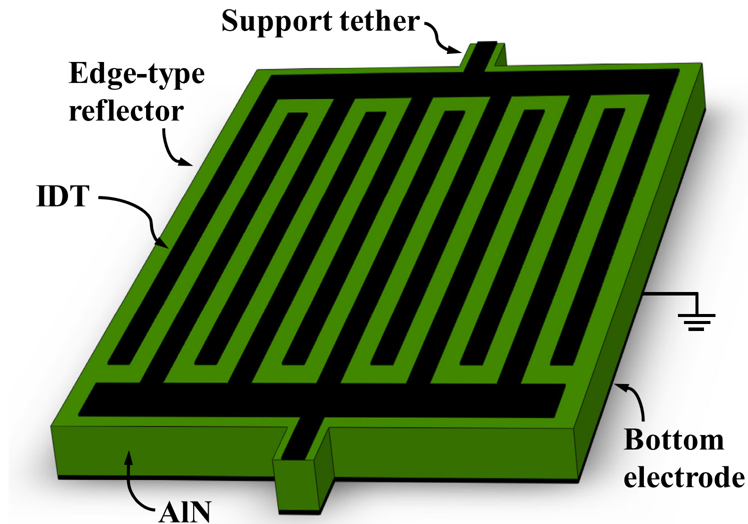

Figure 3-1. Illustration of an AlN LWR utilizing edge-type reflectors.

deposition, the surface roughness, the degree of the metal crystallinity, and the lattice mismatch between AlN thin films and bottom electrode metals are the most important factors which affect the quality and the residual stress of the AlN thin films. The surface temperature can be increased by using external heating during the initial stage of AlN nucleation on the surface of the bottom metal electrode [88] and the surface roughness can be significantly reduced by treating the bottom electrode metals with RF plasma etching [87]. As a result, selection of bottom electrode metals is essential for achieving high-quality AlN thin films. Ideally, if the metal surface has a low degree of lattice mismatch with AlN, a high degree of crystallinity, and an extremely smooth surface, it would be easy to obtain high-quality AlN thin films [89].

3.3.1 Lattice Mismatch between AlN and Metals

As it is pointed out that except for the texture and surface roughness of the underlying electrode metals, the degree of *c*-axis orientation of AlN thin films is strongly dependent on their crystal structures and lattice mismatch with AlN [89]. The most suitable metal for highly *c*-axis oriented AlN growth appears to have hexagonal (0002) crystal structure, such as titanium (Ti). However, Ti shows a high bulk resistivity up to 55 μΩ·cm which is not preferred for low-impedance acoustic wave devices. Since most metals have a cubic crystal structure, it is interesting to investigate the suitable crystalline orientation planes for AlN (0002) thin film growth on the cubic crystal structure. Experimental studies have demonstrated that a suitable texture for face-centered-cubic (FCC) crystal structure, such as aluminum (Al) and platinum (Pt), appears to be (111) and a suitable texture for body-centered-cubic (BCC) crystal structure, such as molybdenum (Mo) and tungsten (W), appears to be (100) [89]. That is, for the same crystal structure, the lattice mismatch between the AlN thin film and the bottom electrode metal becomes more important if the

Table 3-1. Physical properties of selected metals [29].

	Al	Pt	Mo	W	Units
Bulk resistivity	2.8	10.7	5.7	5.39	(10^{-6} Ω·cm)
Mass density	2700	21400	10200	19250	(kg/m^3)
Longitudinal acoustic wave velocity	~6400	~4200	~6700	~5500	(m/s)
Thermal expansion	18	8.9	5.1	4.3	(10^{-6}/°C)
Crystal structure	Cubic (FCC)	Cubic (FCC)	Cubic (BCC)	Cubic (BCC)	–
Crystalline orientation	(111)	(111)	(110)	(110)	–
Lattice constant	4.0494	3.9231	3.1472	3.16	(Å)
Lattice mismatch with AlN	8.68	12.18	1.12	1.52	(%)

degree of the metal crystallinity is similar.

Table 3–1 summarizes and compares the physical properties of common metals used for bottom surface metallization of AlN-based devices [29]. Since the lattice mismatch between AlN and Pt is as large as 12.18% and Pt has higher resistance and larger mass density than the other selected metals, Pt is less used for AlN-based acoustic devices. However, Pt is a good metal for the metallization of AlN-based devices used for high-temperature applications [90], [91]. Although Mo and W show less lattice mismatch than Al, W usually tends to have high levels of residual stress and large surface roughnesses and Mo would be etched by xenon difluoride (XeF_2) during the release process of the AlN LWRs. Moreover, the electrode resistance is a secondary but important factor in

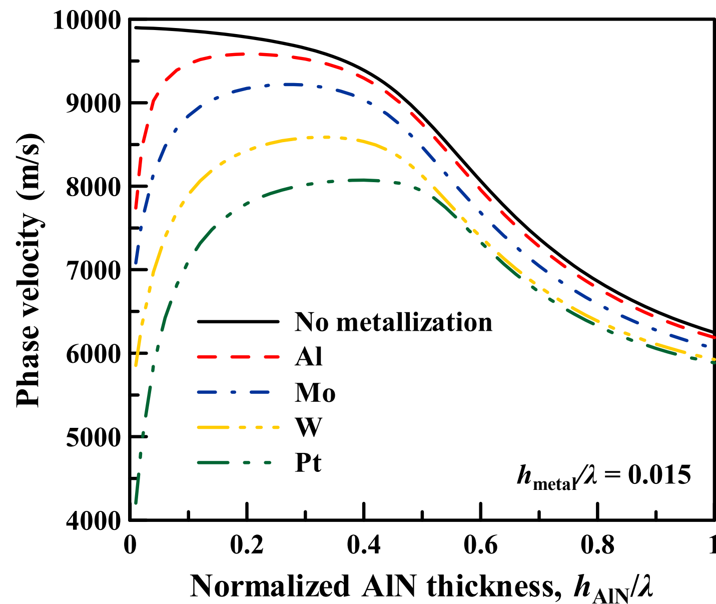

Figure 3-2. Simulated phase velocity of the S_0 mode in AlN films with various bottom metals while the metal thicknesses normalized to the wavelength are fixed to 0.015.

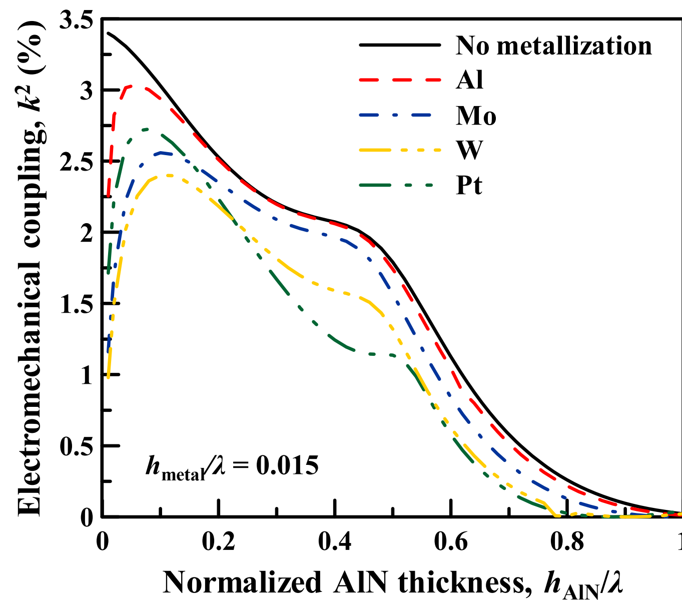

Figure 3-3. Simulated electromechanical coupling of the S_0 mode in AlN films with various bottom metals while the metal thicknesses normalized to the wavelength are fixed to 0.015.

metallization and Al shows a lower resistivity than Mo and W so Al is selected as the bottom metal of the AlN LWRs presented in this work.

3.3.2 Effects on Phase Velocity and Electromechanical Coupling

Except for the effects on the quality of the AlN films grown on metallized bottom surface, there are two main concerns of electrode metallization which strongly affect the Lamb wave resonator performance: phase velocity and electromechanical coupling strength. As shown in Table 3–1, metal materials usually have a low acoustic velocity so the phase velocity of the S_0 Lamb wave mode would be decreased by the metallization on the

Table 3-2. Temperature coefficients of Al, AlN, and SiO_2 used in simulation.

	Symbol	Al	AlN	SiO_2	Units
Temperature coefficients of stiffness constants	TC_{11}	–590	–37	239	(10^{-6} 1/K)
	TC_{12}	–80	–1.8	584	
	TC_{13}	–80	–1.8	584	
	TC_{33}	–590	–65	239	
	TC_{44}	–520	–50	151	
	TC_{66}	–520	–57	151	
Thermal expansion coefficients	α_{11}	18	5.27	0.55	(10^{-6} 1/K)
	α_{33}	18	4.15	0.55	

bottom surface. Fig. 3–2 illustrates the mass loading effect of various metals on the phase velocity of the S_0 Lamb wave mode for a normalized metal thickness fixed to 0.015 and Pt decreases the phase velocity most since Pt has the highest mass density among the selected metals. Contrary to Pt, Al does not decrease the phase velocity very much because of its relatively low mass density. As shown in Fig. 3–2, the electromechanical coupling coefficient would also be decreased by the metallization on the bottom surface and Al decreases the k^2 less than the other selected metals. It is also interesting to note that Pt reduces the k^2 less than Mo and W while the AlN thickness h_{AlN} is within 0.2λ. Considering the AlN thin films grown on the metallized bottom surface and the metal effects on phase velocity and electromechanical coupling strength of the S_0 Lamb wave mode, Al is still a better material for the bottom surface metallization.

3.2 First-order TCF of AlN LWRs

Most materials have negative temperature coefficients of elasticity, implying that they become softer and their resonance frequencies would decrease as temperature increases. However, SiO_2 exhibits positive temperature coefficients of elasticity which can be used to compensate the elasticity decrease of the other materials caused by the temperature increase. Table 3–2 lists the temperature coefficients of Al, AlN, and SiO_2 which can be used to predict the frequency-temperature behavior of the AlN LWR shown in Fig. 3–1. The frequency drift of the AlN LWR relates to the changes in the stiffness constants with temperature and the thermal expansion coefficients, which affect not only the dimensions of the resonator but also the density of the material. The temperature dependence of the stiffness coefficients $C_{ij}(T)$ and the mass density $\rho(T)$ can be defined as [92]

$$C_{ij}(T) = C_{ij}(T_0)(1 + TC_{ij}\Delta T), \tag{3.1}$$

$$\rho(T) = \rho(T_0)\left[1 - \left(\alpha_{\mathrm{x}} + \alpha_{\mathrm{y}} + \alpha_z\right)\Delta T\right], \tag{3.2}$$

where T_0 refers to the reference temperature of the material constants; ΔT is a relative temperature change; TC_{ij} refers to the relative temperature dependence of the stiffness constant C_{ij}; α_{x} (i.e. α_{11}) and α_{y} (i.e. α_{22}) are the thermal expansion coefficients along the x- and y-directions, respectively, which are assumed to be identical herein; α_z (i.e. α_{33}) is the thermal expansion coefficient along the z-direction. Under the linear approximation of the temperature dependence of the stiffness coefficients in (3.1), the mass density in (3.2), and the thermal expansion along the plate length, the TCF of an AlN LWR can be written as [92]

$$\mathrm{TCF}_{\mathrm{LWR}} = \frac{1}{v_{\mathrm{LW}}}\frac{\partial v_{\mathrm{LW}}}{\partial T} - \alpha_{\mathrm{x}}, \tag{3.3}$$

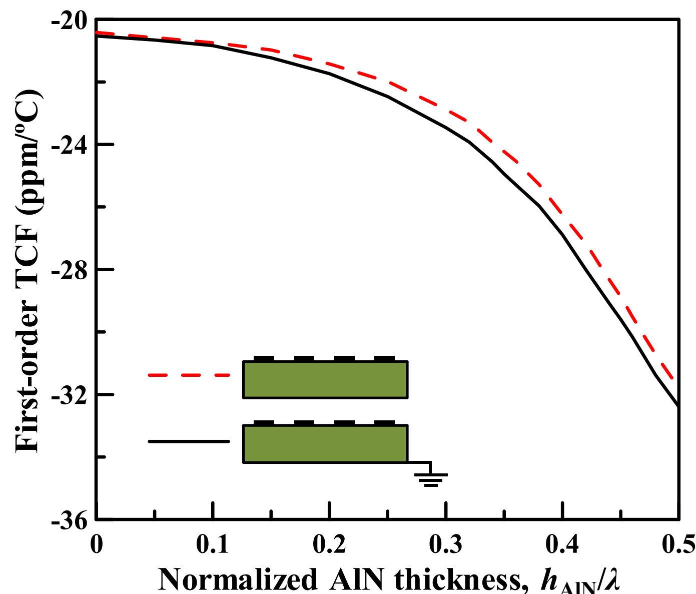

Figure 3-4. Simulated TCFs of the AlN LWRs using the S_0 mode.

where the first term refers to the temperature dependence of Lamb wave velocity which is computed using all the temperature dependent parameters, $C_{ij}(T)$ and $\rho(T)$ for ΔT equal to 10 °C, v_{LW} is the phase velocity of the Lamb wave mode propagating in the piezoelectric plate, and α_x corresponds to the thermal expansion coefficient along the propagation direction (i.e. x-direction in this case).

Neglecting the electrode mass loading effects, the TCF of an AlN LWR can be theoretically predicted using the above formulas and the temperature dependence of material coefficients listed in Table 3–2. Since there are only the first-order temperature coefficients of stiffness constants available in the literature [60], all theoretical simulation only includes the first-order effects on the TCF in this study. The simulated TCFs of AlN LWRs with and without metalized bottom surface are shown in Fig. 3–4. An AlN LWR using the S_0 mode shows a theoretical TCF of around –22 ppm/°C which is close to the experimental results [53]. Moreover, it is interesting to note that a thicker AlN plate shows a worse TCF, especially for an AlN membrane thicker than 0.4λ.

3.3 Zero First-order TCF of AlN/SiO_2 LWRs

In this work, for the first time, we propose a novel edge-type AlN/SiO_2 LWR with a zero first-order TCF. Fig. 3–5 illustrates the zero first-order TCF LWR consisting of one IDT, a metallized interface between the AlN and SiO_2 layers and two suspended free edges at both sides of the AlN/SiO_2 composite plate. The metallized interface can improve the k^2 of the QS_0 Lamb wave mode in an AlN/SiO_2 composite plate as depicted in Fig. 2–13. The TCF of the AlN/SiO_2 composite membrane can be analyzed utilizing the identical

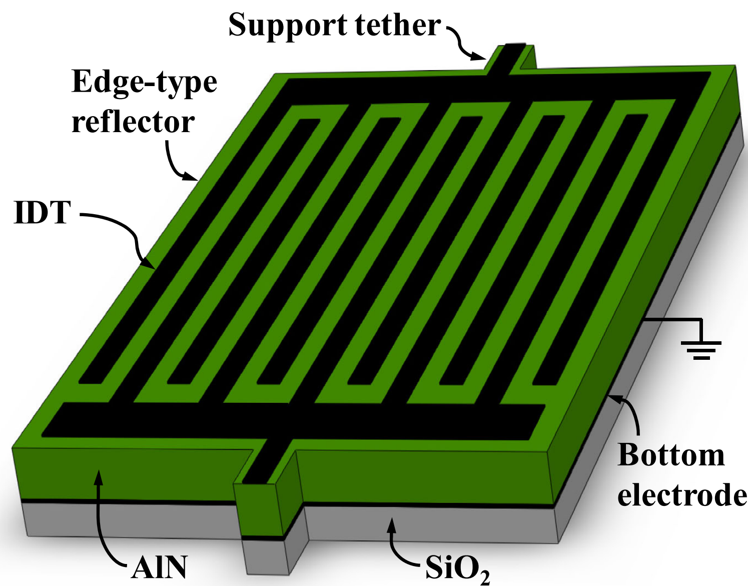

Figure 3-5. Illustration of an AlN/SiO_2 LWR utilizing edge-type reflectors.

computation method as previously used for determining the TCF of an AlN membrane. The only difference is the temperature dependent implementation of all the material parameters involved. The temperature dependence of phase velocity was first calculated for the QS_0 Lamb wave mode in an AlN/SiO_2 composite plate and then the effective thermal expansion in propagation direction of the stack is subtracted from the velocity dependence.

As illustrated in Fig. 3–6, an effective thermal expansion coefficient for estimating the elongation along the Lamb wave propagation direction is required for computing the TCF of the composite structures. The effective thermal expansion coefficient of an arbitrary stack of multiple layers is computed from the thermal expansion of the neutral plane in the stack [92]. The effective thermal expansion coefficient α_{eff} for a stack of i layers is then given as

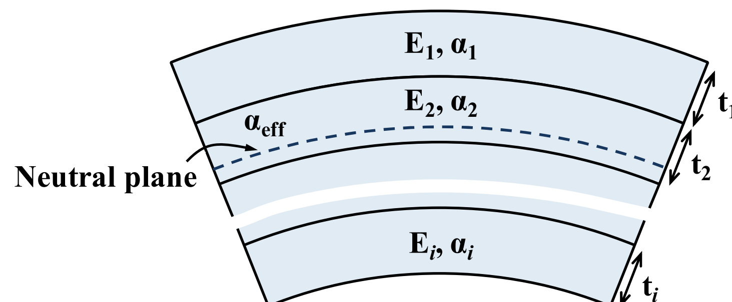

Figure 3-6. The effective thermal expansion experienced at the neutral plane.

$$\alpha_{\mathrm{eff}} = \frac{\sum_{i=1}^{n} E_i t_i \alpha_i}{\sum_{i=1}^{n} E_i t_i}, \tag{3.4}$$

where E_i is the Young's modulus of ith layer, t_i is the thickness of ith layer, and α_i is the thermal expansion coefficient of ith layer, respectively. The temperature dependence of mass density $\rho(T)$ can be defined as

$$\rho(T) = \rho(T_0)\left[1-\left(\alpha_{\mathrm{xeff}}+\alpha_{\mathrm{yeff}}+\alpha_z\right)\Delta T\right], \tag{3.5}$$

where α_{xeff} and α_{yeff} are the effective thermal expansion coefficients of the composite layers along the x- and y-directions, respectively, which are assumed to be identical in this work. Neglecting electrode mass loading effect, the TCF of the LWR on a composite plate is written as [92]

$$\mathrm{TCF}_{\mathrm{LWR}} = \frac{1}{v_{\mathrm{LW}}}\frac{\partial v_{\mathrm{LW}}}{\partial T} - \alpha_{\mathrm{xeff}}, \tag{3.6}$$

where v_{LW} is the phase velocity of the Lamb wave mode propagating in the composite plate and α_{xeff} corresponds to the effective thermal expansion coefficient along the propagation direction (i.e. x-direction herein).

On the AlN/SiO_2 composite structures, the first-order TCF of the QS_0 Lamb wave mode with various h_{AlN}/λ of 0.05, 0.1, 0.15, and 0.2 are theoretically analyzed as shown

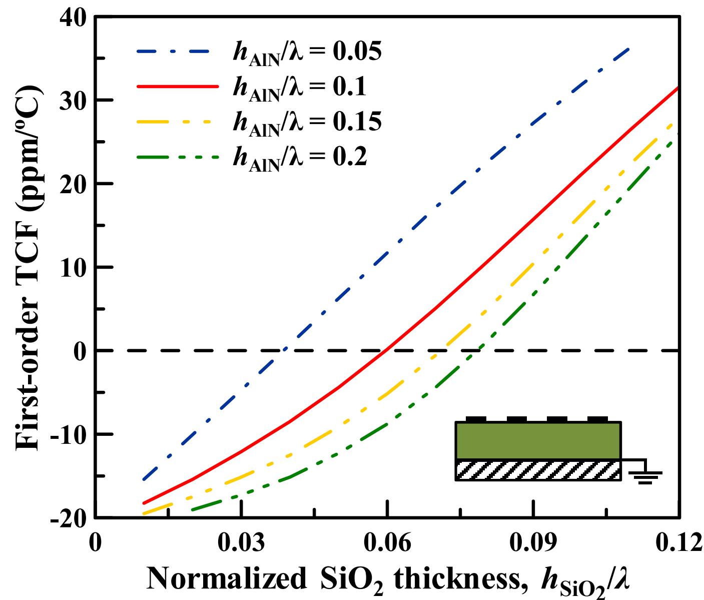

Figure 3-7. Simulated TCF dispersion of the AlN/SiO_2 LWRs using the QS_0 mode.

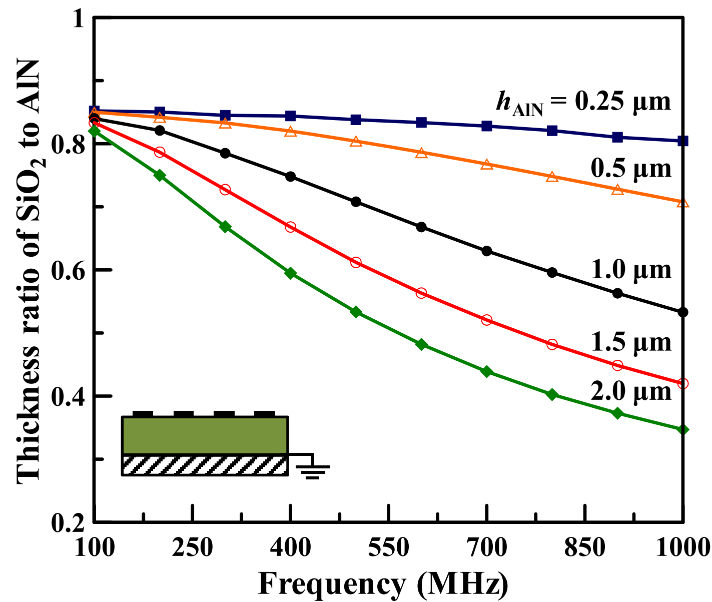

Figure 3-8. Required thickness ratios for the zero-TCF AlN/SiO_2 LWRs operating at different frequencies.

in Fig. 3–7. The analysis shows that the first-order TCF of the QS_0 Lamb wave mode in the AlN/SiO_2 composite membrane has a dispersive characteristic. In other words, the first-order TCF is a function of the relative SiO_2 thicknesses for different AlN thicknesses [92]–[94].

In order to achieve a zero first-order TCF, an appropriate thickness ratio of SiO_2 to AlN is required and the ratio varies with the wavelength λ and the operating frequency as predicted in Fig. 3–8. Considering the electromechanical coupling strength, as shown in

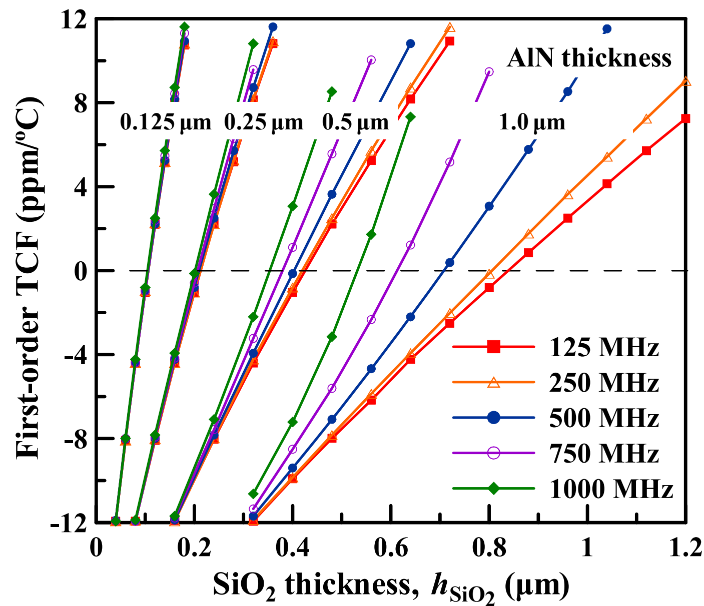

Figure 3-9. SiO_2 thickness and frequency dependence of the first-order TCF for four AlN thicknesses.

Fig. 2–14, the type D device utilizing the QS_0 Lamb wave mode exhibits a maximum k^2 while the h_{AlN} is around 0.1λ. Therefore, based on the simulated prediction, the AlN and SiO_2 thicknesses are selected as 0.1λ and 0.06λ, respectively, to obtain a zero first-order TCF and a large k^2 simultaneously at room temperature.

The TCF of the composite AlN/SiO_2 LWRs with the AlN thicknesses of 0.125 µm, 0.25 µm, 0.5 µm, and 1 µm are shown in Fig. 3–9. The lower dispersion for a very thin AlN plate makes it possible to achieve a very small TCF over the entire frequency range from 100 MHz to 1000 MHz. A composite LWR using a 1-µm-thick AlN film and a 0.72-µm-thick SiO_2 layer will show first-order TCFs varied from –2.45 to –13.86 ppm/°C over the entire frequency range. On the contrary, a Lamb wave device composed of a 0.25-µm-thick AlN thin film and a 0.2-µm-thick SiO_2 layer leads to nearly zero fir-order TCFs over the entire frequency range. In addition, a 200-nm-thick AlN thin film has been successfully deposited on highly textured Mo (110) bottom electrodes and shows a full width at half maximum (FWHM) of rocking curve of 1.8°, showing the possibility to achieve the complete temperature compensation over a wide frequency range by using ultrathin AlN films [88].

3.4 Resonator Basics and Equivalent Circuits

As mentioned in Chapter 1, an IDT usually consists of two sets of electrodes connected alternatively to two bus bars placed on a piezoelectric substrate. The space Λ between two adjacent electrode fingers and their overlap length W are called pitch and aperture, respectively. As shown in Fig. 1–5 (b), the electrode finger width (w) and the distance between them are equal so that the metallization ratio (η) is 0.5 and the IDT finger width is equal to quarter wavelength (λ/4) in this case. Once the phase velocity of the Lamb wave mode of interest is obtained, the resonance frequency can be intuitively estimated by assigning the acoustic wavelength as

$$f_0 = v_{LW} / \lambda = v_{LW} / 2\Lambda = v_{LW} / 4w. \tag{3.7}$$

The resonance frequency of a LWR is determined by the width of the IDT so a thinner electrode finger width in the transducer can achieve higher operation frequencies and it is limited by the lithographic resolution. In addition, by employing high-order Lamb wave modes with higher phase velocities in the piezoelectric plate, one can obtain higher operation frequencies using the same electrode finger width w.

A piezoelectric resonator can be described with the Butterworth-Van Dyke (BVD) equivalent circuit which consists of a mechanical resonance branch including motional resistor (R_m), motional capacitor (C_m), and motional inductor (L_m) and a static capacitor (C_0) in parallel [95], [96]. The clamped capacitor C_0 is simply formed by the capacitance between the IDT electrodes and the plate capacitance sandwiched between the top and bottom electrodes. As shown in Fig. 3–10, a modified Butterworth-Van Dyke (MBVD) equivalent circuit model including two loss resistors, R_s and R_0, was proposed by Larson

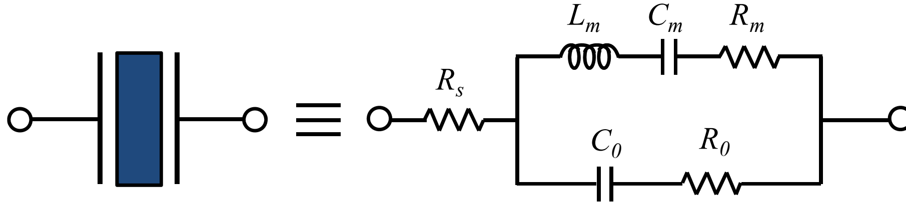

Figure 3-10. Modified Butterworth-Van Dyke (MBVD) equivalent circuit for a piezoelectric resonator.

et al. to improve the match to real piezoelectric BAW resonators [97]. Nominally, the series resistor R_s describes the resistance of the routing pads and electrodes and the parallel resistor R_0 represents the parasitic resistance in the Si substrate [50].

The series and parallel resonance frequencies, f_s and f_p, are the frequencies of the maximum conductance (the real part of the admittance) and the maximum resistance (the real part of the impedance). Based on the six parameters of the MBVD equivalent circuit, the series and parallel resonance frequencies, f_s and f_p, the impedance $Z(\omega)$, and the admittance $Y(\omega)$ can be expressed as [97]

$$f_s = \frac{\omega_s}{2\pi} = \frac{1}{2\pi}\sqrt{\frac{1}{L_m C_m}}, \tag{3.8}$$

$$f_p = f_s\left(1+\frac{C_m}{C_0}\right) = \frac{1}{2\pi}\sqrt{\frac{1}{L_m C_m}\left(1+\frac{C_m}{C_0}\right)}, \tag{3.9}$$

$$Z(\omega) = R_s + \frac{\left(R_0 + \frac{1}{j\omega C_0}\right)\left(R_m + \frac{1}{j\omega C_m} + j\omega L_m\right)}{R_0 + \frac{1}{j\omega C_0} + R_m + \frac{1}{j\omega C_m} + j\omega L_m}, \tag{3.10}$$

$$Y(\omega) = \frac{1}{Z(\omega)}. \tag{3.11}$$

A typical admittance spectrum including magnitude and phase of a resonator is depicted in Fig. 3–11.

Another important characteristic for the resonator is the quality factor Q which represents the ratio of the energy stored in a system to the energy dissipated per cycle. The quality factors of the resonance peaks at the series and parallel frequencies, Q_s and Q_p, can be expressed using the MBVD equivalent circuit parameters,

$$Q_s = \frac{1}{\omega_s (R_m + R_s) C_m}, \tag{3.12}$$

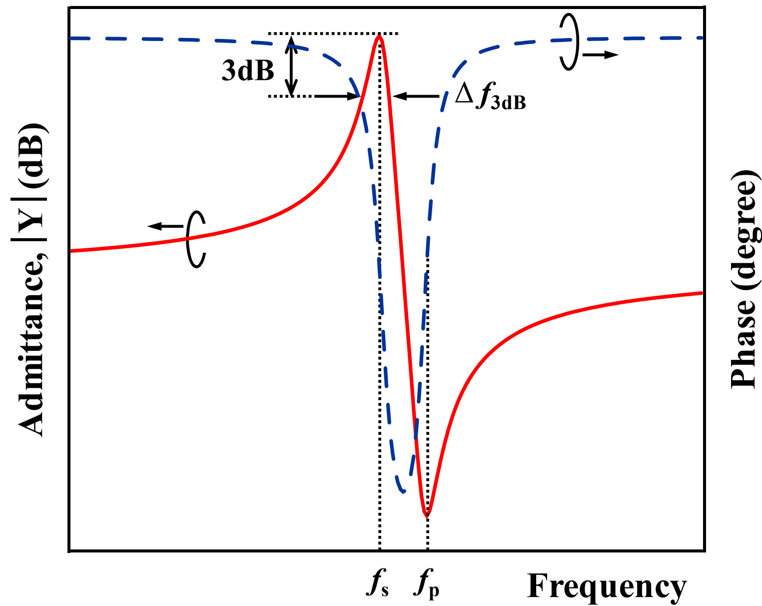

Figure 3-11. A typical admittance spectrum including magnitude and phase of a piezoelectric resonator.

$$Q_p = \frac{1}{\omega_p \left(R_m + R_0\right) C_m} . \tag{3.13}$$

For an simple RLC circuit, the quality factor Q is defined as the ratio of the resonance frequency f_0 to the two-sided 3-dB bandwidth, Δf_{3dB} [98],

$$Q = \frac{f_0}{\Delta f_{3dB}} . \tag{3.14}$$

The quality factor Q can also be determined by using the phase slope of the admittance and defined as [98]

$$Q = \frac{\omega_0}{2} \left| \frac{d\Phi}{d\omega} \right| , \tag{3.15}$$

where ω_0 is the angular frequency at the resonance frequency f_0 and $d\Phi/d\omega$ denotes the phase slope of the admittance with respect to angular frequency.

The electromechanical coupling coefficient is a measure of energy transduction efficiency between the electrical and mechanical domains. In the literature, several different definitions are used for evaluating the effective electromechanical coupling coefficient (k^2_{eff}) of piezoelectric resonators from the measured results. One of the most often used definitions is IEEE standard definition which is fully consistent with analytical derivation for a BAW resonator [95], [99],

$$k_{\mathrm{eff}}^2 = \frac{\pi}{2}\frac{f_{\mathrm{s}}}{f_{\mathrm{p}}}\left[\tan\left(\frac{\pi}{2}\frac{f_{\mathrm{s}}}{f_{\mathrm{p}}}\right)\right]^{-1}. \tag{3.16}$$

The most used approximation for the effective coupling coefficient is defined as

$$k_{\mathrm{eff}}^2 = \frac{\pi^2}{4}\left(\frac{f_{\mathrm{p}} - f_{\mathrm{s}}}{f_{\mathrm{p}}}\right), \tag{3.17}$$

which is simply estimated by the relative difference of the series and parallel resonance frequencies. The k^2_{eff} can be also expressed as the parameters of the MBVD equivalent circuit, C_{m} and C_0,

$$k_{\mathrm{eff}}^2 = \frac{\pi^2}{8}\left(\frac{C_{\mathrm{m}}}{C_0}\right), \tag{3.18}$$

which provides the direct connection the effective coupling to the ratio of the motional capacitance to the clamped capacitance. In this work, the IEEE standard definition in (3.16) is used to evaluate the k^2_{eff} of the AlN/SiO_2 LWRs.

3.5 Experimental Results and Discussions

The fabricated temperature-compensated LWRs were tested in a vacuum probe system (Suss MicroTec® PMC150) that allows probing of chuck-mounted wafers while they are cooled via liquid helium and heated by electric heating elements (on the chuck). A feedback controlled heating unit can provide a precise control of the chuck temperature during measurement. S_{11} parameters for the resonators were extracted using an Agilent E5071B network analyzer. To determine the frequency-temperature characteristic of the AlN/SiO_2 LWRs, resonators were measured in the temperature range from –55 to 125 °C (military grade). The chuck temperature was varied in a 5 °C step with a temperature stabilization time of 10 minutes before measurement at each temperature, and the S_{11} parameters of the resonator were measured five times at each 5 °C step. Before the measurements were taken, the devices were temperature cycled over the full temperature range five times to eliminate observed hysteresis [94]. The quality factor of the series resonance frequency Q_s was extracted from the admittance plot by measuring the 3dB bandwidth method, and the six equivalent circuit parameters were determined by fitting to the measured results with the MBVD equivalent circuit model.

Micromechanical LWRs were fabricated on an AlN/SiO_2 multilayer plate composed of 1-µm-thick AlN and 0.83-µm-thick SiO_2 using the microfabrication process that will be described in Chapter 4. To better understand the effect of the normalized thickness of each layer on the frequency-temperature behavior, two resonator designs with different

Table 3-3. Dimensions of the AlN/SiO_2 LWRs.

	Design 1	Design 2	Units
Top electrode finger number	13	13	–
Aperture W	125	125	(μm)
Electrode finger width w	4.44	2.76	(μm)
Wavelength λ	17.76	11.04	(μm)
Metallization ratio η	0.5	0.5	–
Top Al electrode thickness	150	150	(nm)
Bottom Al electrode thickness	150	150	(nm)
Normalizaed AlN thickness h_{AlN}/λ	0.056	0.091	–
Normalizaed SiO_2 thickness h_{SiO_2}/λ	0.047	0.075	–

wavelengths were compared, and their detailed dimensions are given in Table 3–3. As shown in Fig. 3–12, the design 1 resonator has an f_s of 460 MHz, a R_m of 107 Ω, a k^2_{eff} of 0.33%, and a Q_s of 1532, and the design 2 resonator shows an f_s of 711 MHz, a R_m of 150 Ω, a k^2_{eff} of 0.56%, and a Q_s of 980. Some spurious modes at around 900 MHz for the design 1 resonator might be the high-order Lamb wave modes propagating in the AlN plate. For the design 2 resonator, there is no spurious mode over a 1 GHz frequency range which is excellent for oscillator and filter applications.

From Table 3–3, the wavelength of the design 2 resonator was 11.04 μm, and the measured resonance frequency is 711 MHz, so the measured Lamb wave velocity is roughly equal to 7850 m/s. This measured value is close to the theoretical phase velocity

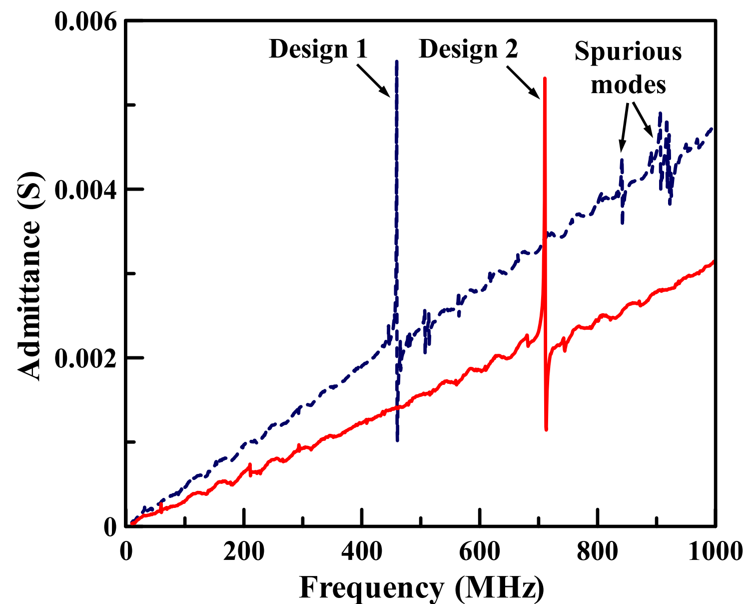

Figure 3-12. Measured broadband frequency spectrums of the two AlN/SiO_2 LWRs.

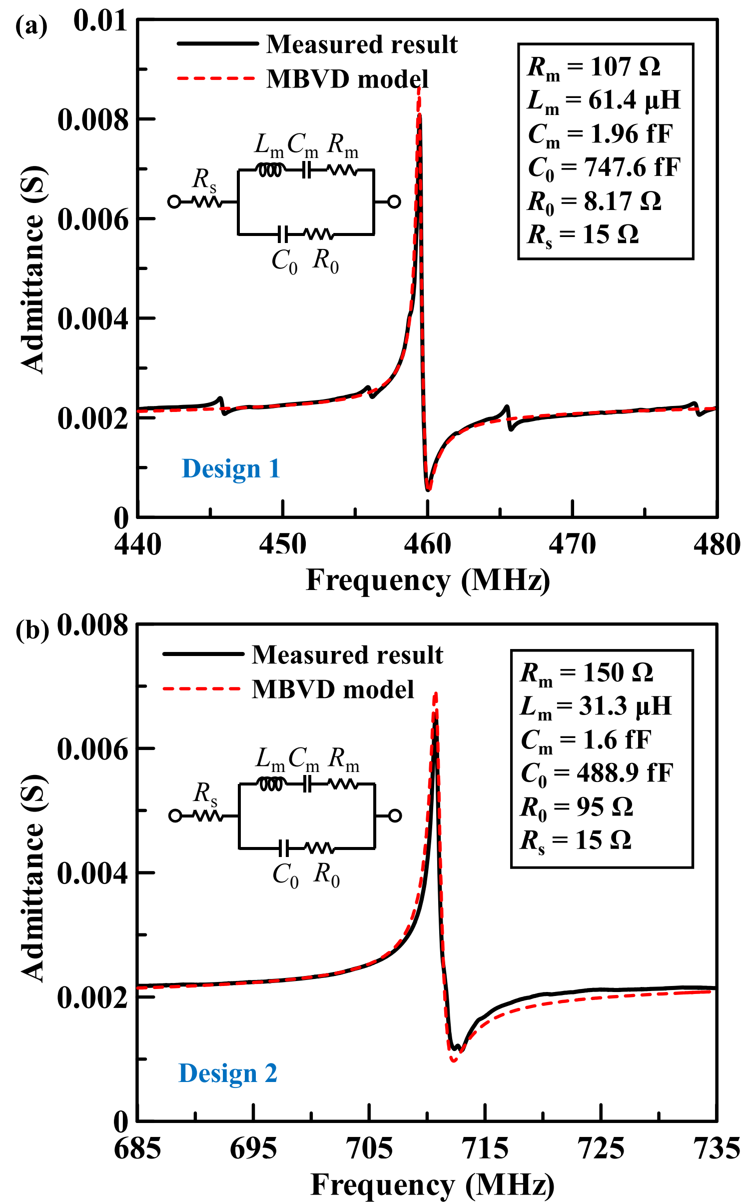

Figure 3-13. Close-up view of the frequency spectrums and the MBVD equivalent circuit fitting of (a) design 1 and (b) design 2 resonators.

of the S_0 mode, 8435 m/s, for the h_{AlN} and h_{SiO2} equal to 0.091$\lambda$and 0.075λ, respectively. If the 150-nm-thick Al bottom electrode (h_{Al}/λ = 0.0136) were taken into account in the simulation, the theoretical phase velocity would be reduced to 8142 m/s. The mismatch between theoretical and the experimental velocities of the S_0 mode might be caused from the neglect of IDT and the inaccuracy of the AlN material constants in the simulation.

Fig. 3–13 shows the close-up view of the frequency spectrums of the two LWRs and their MBVD equivalent circuit model fitting which is used for extracting the 6 equivalent circuit parameters. From the experimental results, we observe that the design 1 and 2 resonators show low effective coupling coefficients of 0.33% and 0.56%, respectively,

which are less than the expected values. The electromechanical coupling coefficient is originally given for an idealized simple structure composed of uniform thin film materials. In fact, the real devices are more complex: the influence of the electrode metallization, the electrode thickness, and the AlN thin film quality are not considered in the theoretical calculation. In general, the intrinsic electromechanical coupling k^2 calculated using (2.28) overestimates the effective electromechanical coupling k^2_{eff} excited by the interdigital transducer [100]. In addition, as shown in Fig. 3–13 (b), a large electrical capacitance C_0 of 488.9 fF is observed from the MBVD equivalent circuit. The electrical capacitance, resulted from a static capacitance of 372.8 fF and an external parasitic capacitance of 116.1 fF, also reduces the effective coupling coefficient k^2_{eff}. Furthermore, in this study, the AlN thin film has an FWHM value of 1.77° which indicates less than the perfect thin film quality. The combination of these phenomena is suspected to cause the low effective electromechanical coupling coefficients in the fabricated devices.

Fig. 3–14 shows the plot of measured fractional frequency variation for the two design resonators in Table 3–3 over the wide temperature range from –55 to 125 °C. It should be noted that the total fractional frequency variation of the design 2 resonator is less than 250 ppm over the temperature range of 180 °C and completely compensated at around room temperature. In addition, the temperature-dependent fractional frequency variation of the two LWRs shows a quadratic function of temperature since their linear TCF part was significantly reduced by the SiO_2 layer. As pointed out in Fig. 3–7, the first-order TCF is dispersive with the relative AlN and SiO_2 thicknesses. That is to say, the thickness ratio of AlN to SiO_2 determines the first-order TCF of the whole stacked structure. As a result, the first-order TCF of the design 2 resonator is almost cancelled out with an appropriate thickness ratio of SiO_2 to AlN.

In Fig. 3–15, a quadratic polynomial is adopted to fit the experimental results for the design 1 resonator, which shows a first-order TCF of –7.61 ppm/°C and a second-order

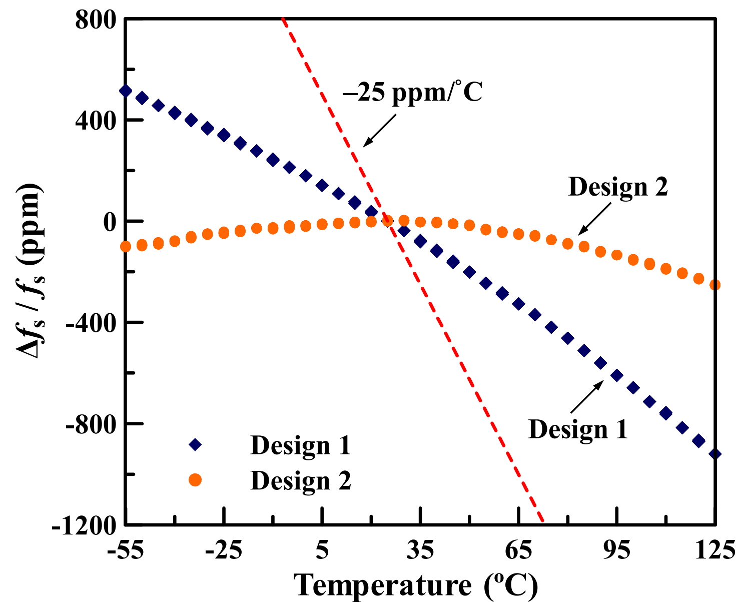

Figure 3-14. The plot of measured fractional frequency variation versus temperature of the two LWRs.

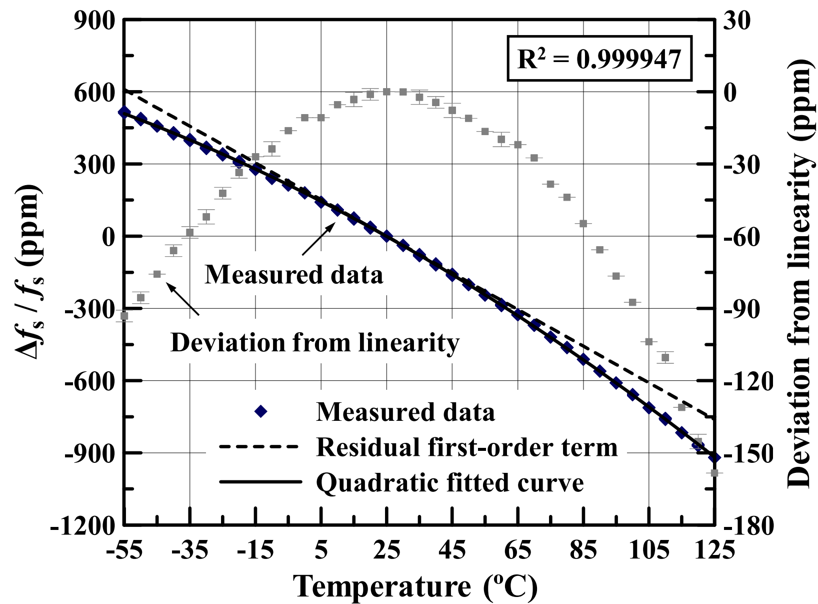

Figure 3-15. Measured fractional frequency variation versus temperature of the design 1 LWR.

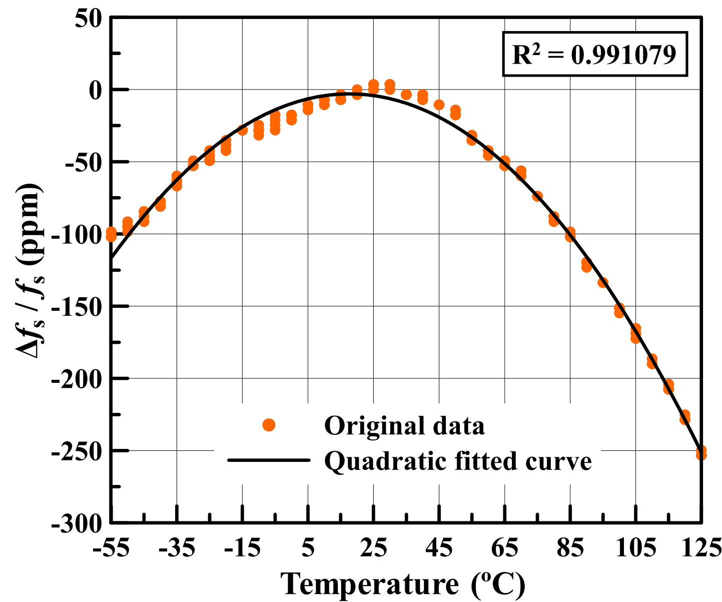

Figure 3-16. Measured fractional frequency variation versus temperature of the design 2 LWR.

TCF of –15.7 ppb/°C^2 at room temperature, 25 °C. The first-order TCF of the design 1 resonator is only reduced to –7.61 ppm/°C because the thickness ratio of AlN to SiO_2 is not correct for the zero first-order TCF compensation at room temperature. As a result, although the TCF of the design 1 resonator includes a combination of first-order, second-order, and even higher-order terms, clearly the residual first-order TCF dominates its temperature-dependent fractional frequency variation.

In contrast, with a proper combination of AlN thin film and SiO_2 layer, the first-order TCF of the design 2 resonator is almost zero at room temperature so that the second-order

Table 3-4. Performance of the AlN/SiO_2 LWRs.

	Design 1	Design 2	Units
Series resonance frequency f_s	460	711	(MHz)
Motional resistance R_m	107	150	(Ω)
Effective coupling coefficient k^2_{eff}	0.33	0.56	(%)
Quality factor Q_s	1532	980	–
First-order TCF at 25 °C	–7.61	–0.31	(ppm/°C)
Second-order TCF at 25 °C	–15.7	–21.5	(ppb/°C^2)

term dominates its characteristic of temperature-dependent fractional frequency variation. The experimental result shows a first-order TCF of –0.31 ppm/°C and a second-order TCF of –21.5 ppb/°C^2 at room temperature as depicted in Fig. 3–16. The fractional frequency variation of the resonator exhibits a temperature-dependent quadratic function with a turnover temperature (T_o) at 18.05°C. If room temperature is used as the reference temperature, the fractional frequency variation can be expressed as

$$\frac{f(T)-f(25)}{f(25)} = -0.31\times10^{-6}\times(T-25)-21.5\times10^{-9}\times(T-25)^2 \tag{3.19}$$

The turnover temperature T_o can be used as the reference temperature and the first-order TCF becomes zero at its turnover temperature so the fractional frequency variation can be

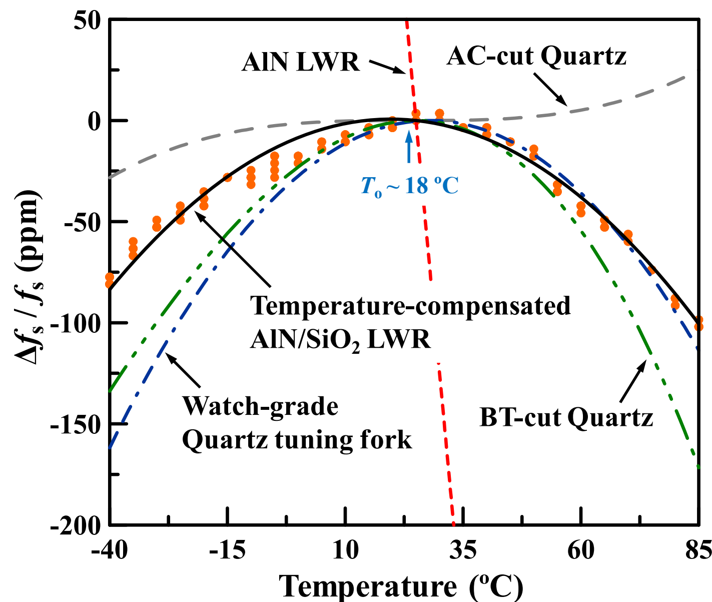

Figure 3-17. Comparison of the frequency-temperature stability between the design 2 LWR and three selected crystal resonators.

expressed as

$$\frac{f(T)-f(T_o)}{f(T_o)} = -21.5\times10^{-9}\times(T-T_o)^2 \tag{3.20}$$

The overall performance of the two AlN/SiO_2 LWRs is summarized in Table 3–4. The frequency-temperature stability of the design 2 resonator is also compared with that of the AT-cut and BT-cut quartz resonators as well as the watch-grade quartz tuning fork in a temperature range from –40 to 85 °C (industrial grade). As shown in Fig. 3–17, the performance of the design 2 resonator is only worse than the AT-cut quartz since it has both of zero first- and second-order TCFs. The second-order TCF of the LWR can be further reduced by using a metal with positive second-order TCEs as the bottom electrode metal, such as Mo [61].

In the case of the design 2 resonator, the excellent temperature compensation was achieved using 0.83-µm-thick SiO_2 and 1-µm-thick AlN layers, and the first-order TCF is successfully reduced to –0.31 ppm/°C at room temperature. However, the experimental results do not show good agreement with the theoretical predictions in Fig. 3–7. The slight difference between the experimental and theoretical results is likely due to the assumption of infinitely thin bottom electrodes and the neglect of IDT thickness in the simulation. As shown in Fig. 3–18, the dashed line represents the theoretical first-order TCF of the design 2 resonator when the Al bottom electrode is assumed to be infinitely thin in the metallized interface; in contrast, the solid line represents the theoretical first-order TCF while the 150-nm-thick Al bottom electrode is considered in the metallized interface, and the red dot represents the experimental result. As is shown in Table 3–2, Al has larger temperature coefficients than AlN and thermal expansion coefficients than AlN

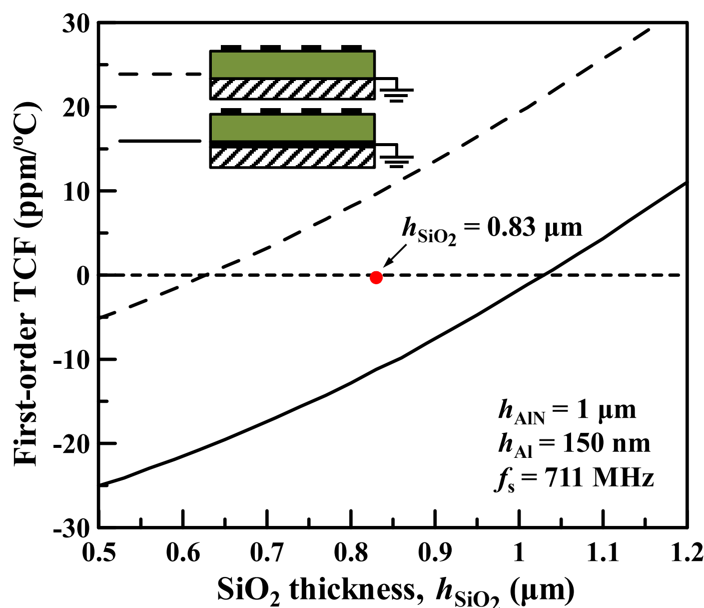

Figure 3-18. The effect of the Al bottom electrode on the first-order TCF of the design 2 LWR.

and SiO_2, and its thickness is comparable to the thicknesses of the AlN and SiO_2 layers used in this work. As a result, the theoretical first-order TCF of the design 2 resonator decreases from 9.62 to –11.2 ppm/°C when the 150-nm-thick Al bottom electrode is taken into account in the simulation. As depicted in Fig. 3–18, the experimental result lies between these two extremes.

There are several sources of uncertainty in the simulation. First, the accuracy of the first-order TCF prediction heavily relies on the accuracy of the material property data, in particular the TCEs of the materials used in the simulation. At least three different sets of the temperature coefficients of stiffness for AlN have been published and compared [101]. The low-temperature oxide layer is used as the thermal compensating material in this experiment but the material properties of bulk fused silica are used in the simulation due to the lack of reliable temperature coefficient data for the SiO_2 thin film. Furthermore, all of the thin films have residual stresses of several hundred MPa after deposition, which can affect the first-order TCF variation to a great extent [101]. Finally, although the two resonators were fabricated on the same wafer, the thin film depositions (AlN, Al, and SiO_2) were not ideally uniform across the wafer and the uncertainties in film thicknesses influence the accuracy of the predicted TCFs. In this study, the non-uniformity of the Al film thickness was about 3 %, the non-uniformity of the AlN film was about 1 %, and the non-uniformity of SiO_2 film was about 6 %. The worst cases for the uncertainties in the simulated first-order TCF (–11.2 ppm/°C) caused by the film non-uniformity are –15.8 % and +14.2 %, respectively. Despite all of these sources of uncertainty, we are encouraged that the experimental results fall within the range of performance predicted by the model and it presents a useful tool for designing zero TCF LWRs. In the future, more accurate temperature coefficients of elasticity and residual stresses in thin films are needed to be introduced to the theoretical simulation for a better theoretical prediction of the TCF.

Chapter 4

Microfabrication of Temperature-Compensated AlN/SiO_2 LWRs

Bulk piezoelectric materials have been found for over 100 years and play an important role in the timing and frequency control applications for over 50 years. Microfabrication techniques for piezoelectric thin films compatible with CMOS chips have advantages in reducing the device sizes, manufacturing costs, and enabling integration with electronics. Fundamental limitation in the miniaturization process of piezoelectric devices concerns issues with deposition of well-textured piezoelectric thin films in a repeatable manner. Sputtered AlN thin films have demonstrated the fabrication of piezoelectric devices on Si substrates, the capability of mass production and the integration of AlN BAW resonators above integrated circuits [85], [102]. Duplexers and oscillators based on the AlN FBARs have been commercially available [13], [29]. In this chapter, a five-mask fabrication process is described to manufacture the temperature-compensated AlN/SiO_2 LWRs. The deposition and characterization of highly *c*-axis oriented AlN thin films on Al bottom electrodes are also presented. Some issues with Al metallization of the bottom surface and oxide hard mask deposition on the Al top electrode are discussed and addressed.

4.1 Fabrication Process Flow

As described in Fig. 4–1, a five-mask fabrication process, compatible with CMOS chips, was utilized to fabricate the temperature-compensated AlN/SiO_2 LWRs. As we discussed in Chapter 3, Al is selected as the metal material for the bottom surface metallization since Al shows small lattice mismatch with AlN, low resistivity, as well as slight mass loading effects on the phase velocity and electromechanical coupling. The fabrication process could be easily modified for other bottom electrode metals, such as Mo, Pt, or W.

First, as shown in Figs. 4–1 (a) and (b), a 300-nm-thick low-stress nitride (LSN) layer was deposited on Si (100) wafers in a low pressure chemical vapor deposition (LPCVD) furnace under 835 °C. The LSN stress depends on the film thickness and the film stress is around 300 MPa while the LSN thickness is around 300 nm. The LSN layer is used for electrical isolation with the Si substrates and eliminates unwanted current feedthrough

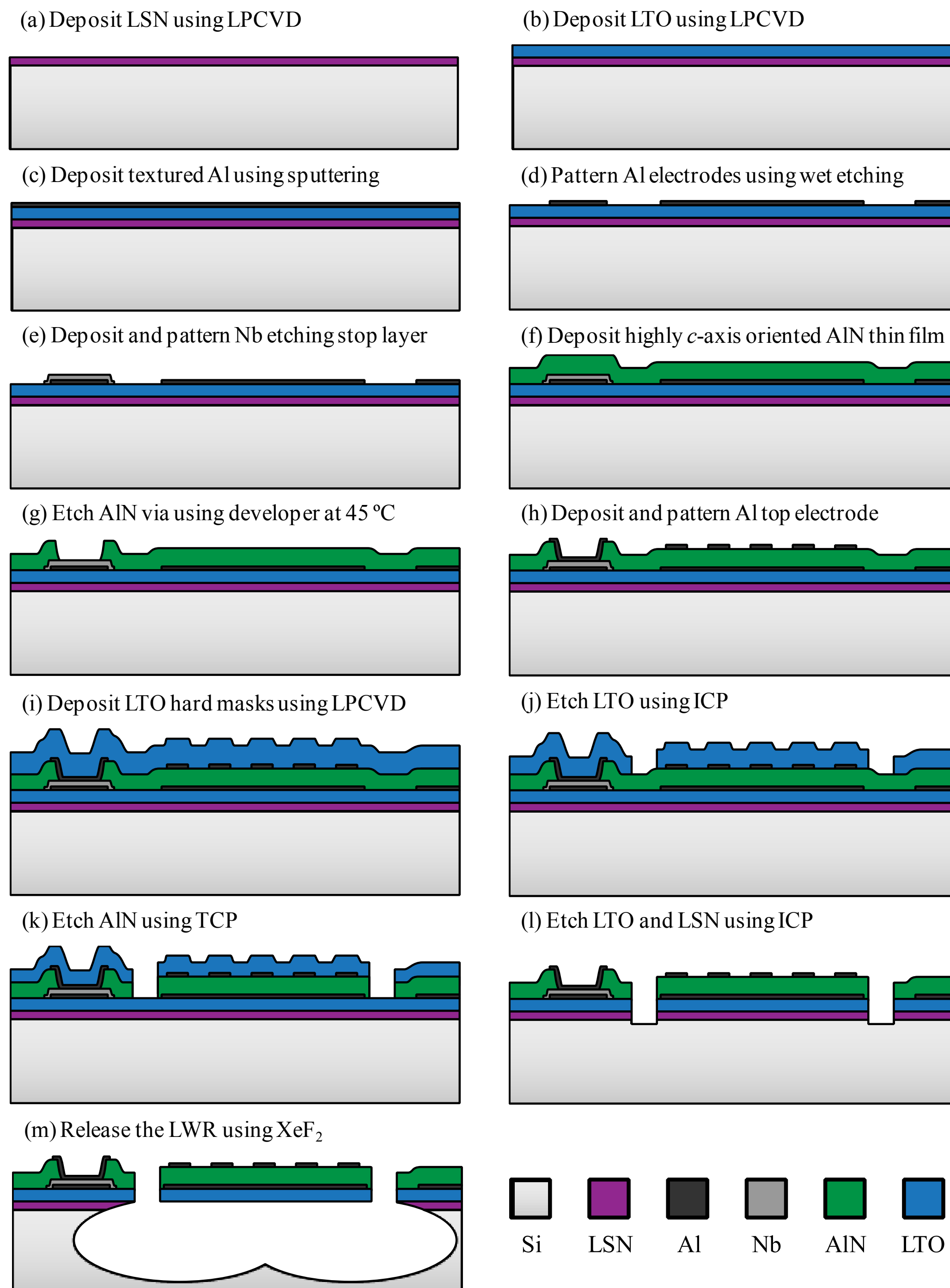

Figure 4-1. Cross-sectional process flow for the AlN/SiO_2 LWRs.

and substrate losses. Then a low-temperature oxide (LTO) layer was deposited on the top surface of the LSN layer in another LPCVD furnace at approximately 400 °C, and is used for temperature compensation and electrical isolation.

The 150-nm-thick Al bottom electrode with strong crystalline orientation at (111) was deposited by sputtering and the patterned by a wet etching process using commercial Al

etchant solution. A Shipley Microposit CD30 developer is used in the photoresist development process step since the existing OCG 934 2:1 and OPD 4262 developer containing tetramethylammonium hydroxide (TMAH), which attacks Al and AlN during the development process. Since the preparation of highly textured Al (111) bottom electrodes is critical for AlN thin film growth, a detailed discussion on the sputtered Al bottom electrode is presented in Section 4.2. The molybdenum (Mo) or niobium (Nb) used for etching stop layer was then deposited and patterned by a lift-off process on the Al bottom electrodes as shown in Figs. 4–1 (c)~(e). If other metal material which can stand the attack from the developer, such as Mo, Pt, or W, is used as the bottom electrode, the process step of the etching stop layer in Fig. 4–1 (e) can be ignored.

A 1-μm-thick highly *c*-axis oriented AlN (0002) thin film was deposited by AC reactive sputtering using an Endeavor-AT sputtering tool from the Tegal Corporation [85]. The preparation of highly textured AlN thin films on the Al bottom electrodes and the AlN characterization will be discussed in details in Section 4.3. As shown in Fig. 4–1 (g), the electrical contact vias through the 1-μm-thick AlN layer were opened by wet etching using the developer OCG 4262 at around 45 °C. Because the developer is utilized as the etchant for AlN, the photoresist should be hot baked using ultraviolet light at 240 °C for 4 minutes before the wet etching process.

Consequently a dual photoresist layer was coated and patterned for the lift-off process of the 150-nm-thick Al top finger electrodes on the AlN thin film as shown in Fig. 4–1 (h). Prior to the dry etching of the AlN thin film, as shown in Figs. 4–1 (i) and (j), a layer of LTO was deposited at around 400 °C, patterned using C_4F_8-based inductively coupled plasma (ICP) etching, and then used as a hard mask. Since the melting point of Al is approximately 650 °C, the LPCVD LTO furnace at around 400 °C would cause some damage on the Al bottom electrodes. Therefore, an additional protection layer is required for Al to stay in the LPCVD LTO furnace. A detailed discussion on the selection of the protection layer will be described in Section 4.4.

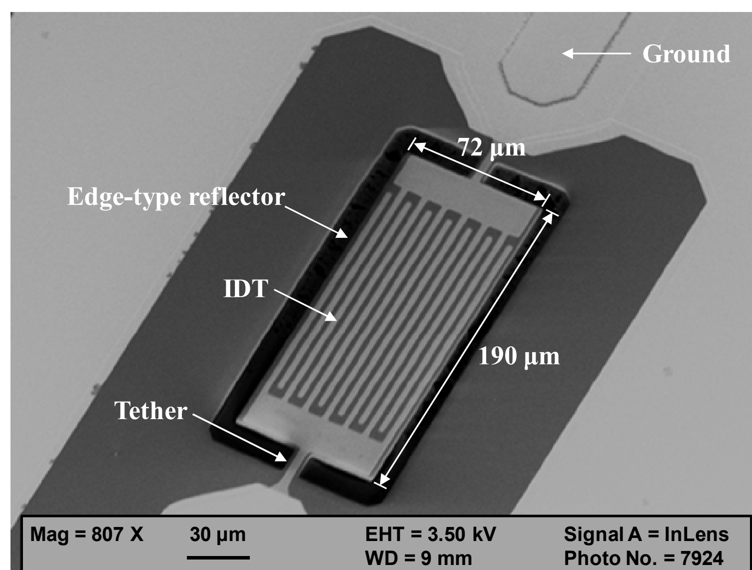

Figure 4-2. SEM image of the fabricated AlN/SiO_2 LWR (design 2) using edge-type reflectors.

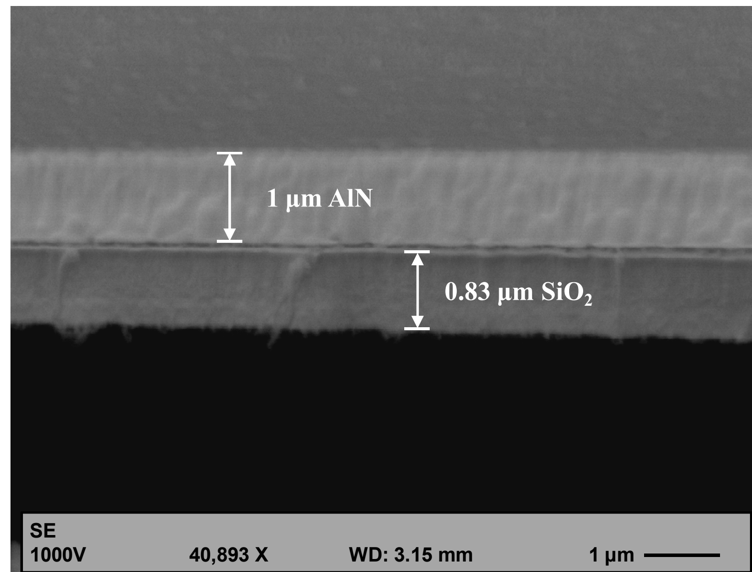

Figure 4-3. Cross-sectional SEM image of the AlN/SiO_2 composite membrane.

The photoresist used to define the patterns of the LTO hard mask has to be removed after the LTO etching step since the photoresist would generate some organic byproducts on the sidewalls in the dry etching chamber. As shown in Figs. 4–1 (k) and (l), a CF_4-based reactive ion etching (RIE) process was used to remove the remaining LTO hard mask and simultaneously pattern the LTO thermal compensation layer after the AlN layer was patterned by the Cl_2-based transformer coupled plasma (TCP) etching. Finally, as shown in Fig. 4–1 (m), the AlN/SiO_2 resonators were released by using a XeF_2-based isotropic dry etching of Si, and the LSN layer beneath the AlN/SiO_2 composite structure was also etched by XeF_2 during the release process.

Fig. 4–2 shows a scanning electron micrograph (SEM) image of the fabricated AlN/SiO_2 LWR (design 2) using the processes described above. Fig. 4–3 shows a cross-sectional SEM image of the composite AlN/SiO_2 membrane with a 1-µm-thick AlN film and a 0.83-µm-thick SiO_2 layer which was used for the temperature-compensated LWRs in this study.

4.2 Metallization of Al Bottom Electrode

As mentioned in Section 3.1, the crystal orientation of piezoelectric AlN thin films has direct correlation with the quality of the underlying metal layer, especially its crystal orientation, and surface roughness. In our experimental results, the sputtered Al layer has no preferred orientation on the surface of the SiO_2/LSN/Si substrate due to the poor crystal orientation of the amorphous SiO_2 layer. However, sputtered Al deposition on the surface of the textured AlN layer enables growth of highly (111) oriented Al films [87]. Therefore, an AlN seed layer is critical to form highly textured Al electrodes. Moreover,

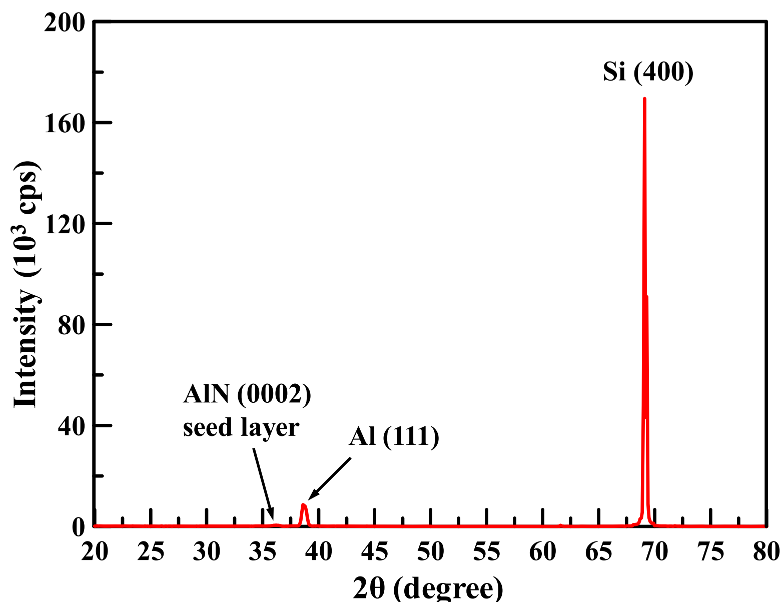

Figure 4-4. Normal coupled scan of the Al(111)/AlN(0002)/SiO_2/Si layered structure.

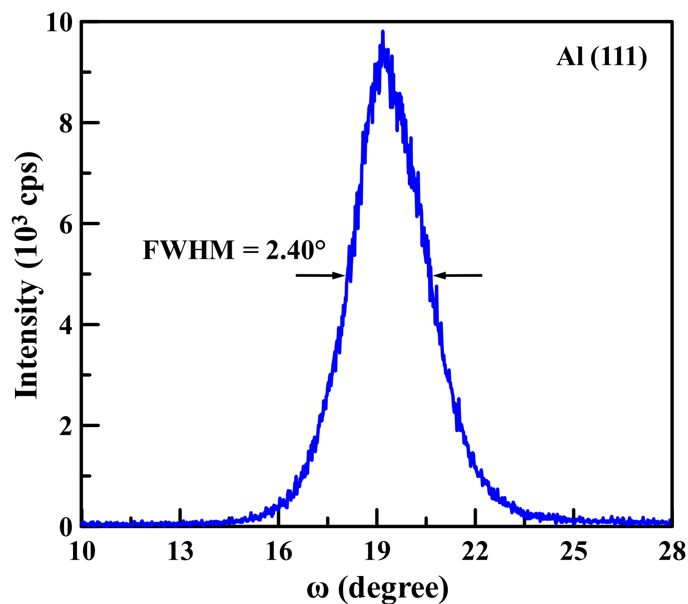

Figure 4-5. Rocking curve scan of the 150-nm-thick Al (111) layer.

the orientation efficiency of the AlN seed layer was significantly improved when the surface of the SiO_2 layer was treated with RF plasma etching prior to the AlN seed layer deposition.

In this work, both of the AlN seed layer and Al electrode were deposited in the same process module equipped with AC (40 kHz) powered S-Gun for sputtering [85], [87]. The main process flow to prepare a highly textured Al (111) bottom electrode consists of the following steps:

(1) Etch the surface of the substrate in argon (Ar) plasma using a capacitive-coupled

RF (13.56 MHz) plasma source for 180 sec at least.

(2) Deposit a 25-nm-thick AlN seed layer using reactive sputtering to enhance the crystallization of the subsequently deposited Al film.

(3) Deposit the 150-nm-thick Al electrode by sputtering with Ar gas right after the AlN seed layer deposition without the Al target cleaning.

Using the above process flow, smooth Al electrodes with surface roughness as low as 2 nm and low residual tensile stress below 100 MPa can be deposited.

X-ray diffraction (XRD) provides a non-destructive and efficient method to analyze the crystallized material structure. A normal coupled scan (i.e. θ–2θ scan) is utilized to know the number of the crystallized material structures and a rocking curve (i.e. ω curve) scan is used to determine the film quality of the Al bottom electrode and AlN layer in this work. Fig. 4–4 shows the normal coupled scan of the Al(111)/AlN(0002)/SiO_2/Si layered structure, and as shown in Fig. 4–5, the 150-nm-thick Al bottom electrode shows a rocking curve FWHM value of 2.4°, indicating highly crystallized Al metal layer was successfully grown on the LTO layer. Most recently, Al electrode layer with excellent crystallinity exhibited single (111) crystal orientation, showing a rocking curve FWHM of 0.7° was demonstrated using a optimization of film nucleation conditions as well as sputtering with low deposition rate and low sputtering Ar gas pressure [87].

4.3 AlN Thin Film Deposition and Characterization

The grain orientation of the AlN thin film exhibits a strong correlation with the electromechanical coupling strength and quality factor so the deposition of highly *c*-axis oriented AlN thin films is the most critical process for piezoelectric devices. Except for the crystalline orientation, a low thin film stress is equally important since the released devices are usually broken due to a high residual stress. In this work, the AlN thin film was deposited on the Al/SiO_2/Si substrate by AC (40 kHz) powered S-Gun magnetron. Prior to the AlN film deposition, the surface of the patterned Al bottom electrodes was pretreated by RF plasma etching to achieve smooth surface roughness. For different substrate materials, the required plasma etching time would be different since they have different atomic binding energy and the lower sputtering yield [87], [88]. For example, a

Table 4-1. Reactive sputtering conditions for AlN thin film deposition.

		Units
Al target purity	99.999	(%)
Base pressure	$< 2\times10^{-7}$	(torr)
AC power (40 kHz)	4~6.5	(kW)
Ar flow rate	0~10	(sccm)
N_2 flow rate	18~30	(sccm)
Deposition rate	50~60	(nm/min)

RF plasma etching duration of 180 sec is long enough to achieve highly *c*-axis oriented AlN thin films on a Si substrate but a plasma etching time of 300 sec is required to deposit highly textured AlN thin films on a cubic silicon carbide (3C–SiC) substrate [103], [104].

The AlN thin film sputtering process was performed at the ambient temperature of around 300–350 °C and the common reactive sputtering conditions are summarized in Table 4–1. Fig. 4–6 shows the normal coupled scan of the AlN(0002)/Al(111)/SiO_2/Si layered structure. As shown in Fig. 4–7, the 1-μm-thick AlN layer shows a rocking curve

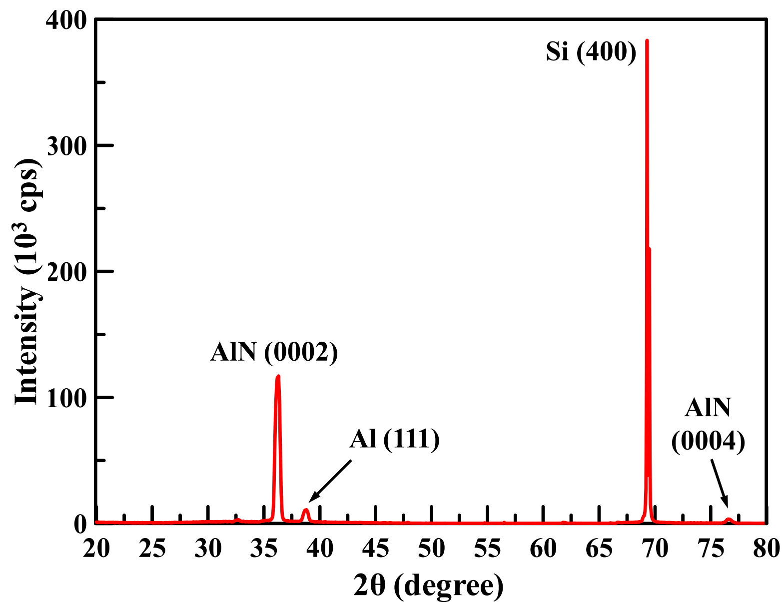

Figure 4-6. Normal coupled scan of the AlN(0002)/Al(111)/SiO_2/Si layered structure.

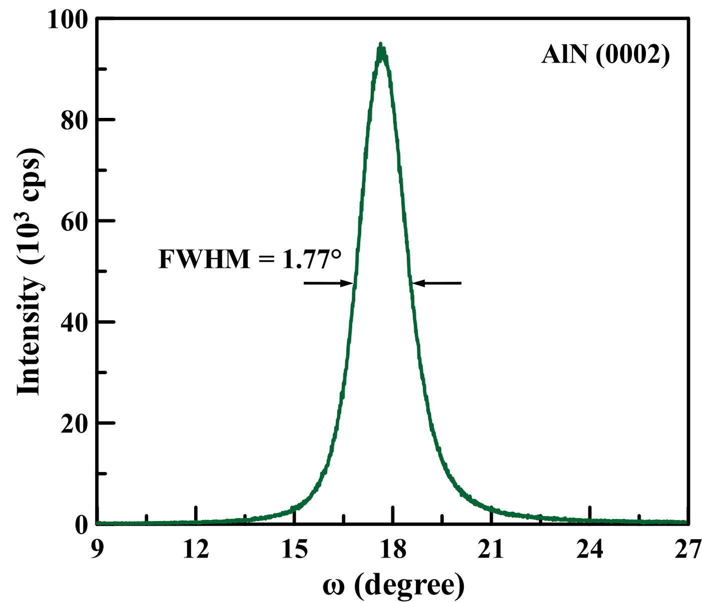

Figure 4-7. Rocking curve scan of the 1-μm-thick AlN (0002) layer.

FWHM value of 1.77°, implying highly *c*-axis oriented AlN thin film was successfully grown on the patterned 150-nm-thick Al bottom electrodes. The residual stress of the AlN thin film can be measured by a laser interferometer, measuring the curvature of the whole wafer before and after the deposition of the AlN thin film. By adjusting the AC power or the Ar and nitrogen (N_2) flow rates, the stress of the deposited AlN thin film can be controlled within tensile and compressive 100 MPa. It should be noted that the AC power and the gas flow rate also influence the deposition rate and the uniformity of the AlN thin film on the whole wafer.

4.4 Low-Temperature Oxide (LTO) Hard Mask

Although the LTO hard mask layer was deposited at around 400 °C in the LPCVD furnace, as shown in Fig. 4–8, the sputtered or evaporated Al top finger electrodes on the AlN layer had some damages due to its staying in the elevated temperature environment for eight hours at least. Therefore, an additional protection layer is required for Al to stay in the high-temperature furnace.

Because Nb has a melting point up to around 2450 °C, excellent temperature stability, and it can be easily removed by Cl_2-based dry etching, it was selected as the protection layer for the Al top electrodes. First a 20-nm-thick Nb as sputtered on the surface of the Al layer right after the 150-nm-thick Al deposition. The Nb/Al top electrode was patterned using a lift-off process and then a 2-μm-thick LTO layer was deposited on the surface of the Nb/Al top electrodes. For the 2-μm-thick LTO layer deposition, it usually takes six hours at least for temperature stabilization and deposition in the LPCVD furnace. Fig. 4–9 (a) shows the microscope image of the Nb/Al top finger electrodes after the LTO layer deposition. The Nb/Al top electrodes still had serious damages after long-time stay in the high-temperature furnace.

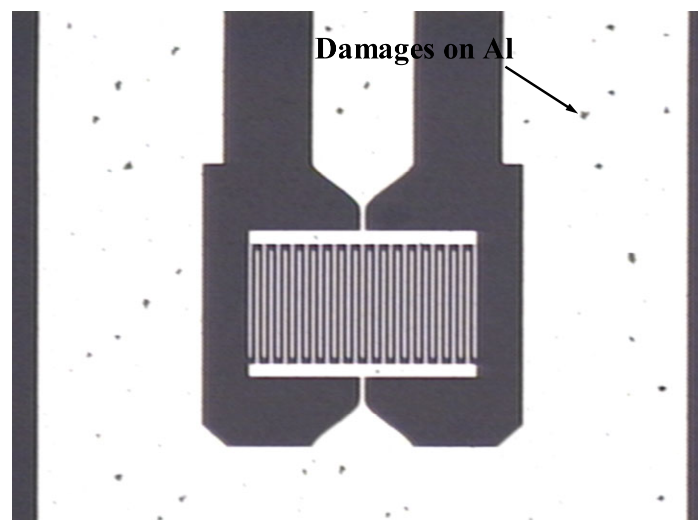

Figure 4-8. Microscope image of the Al electrode after LTO layer deposition.

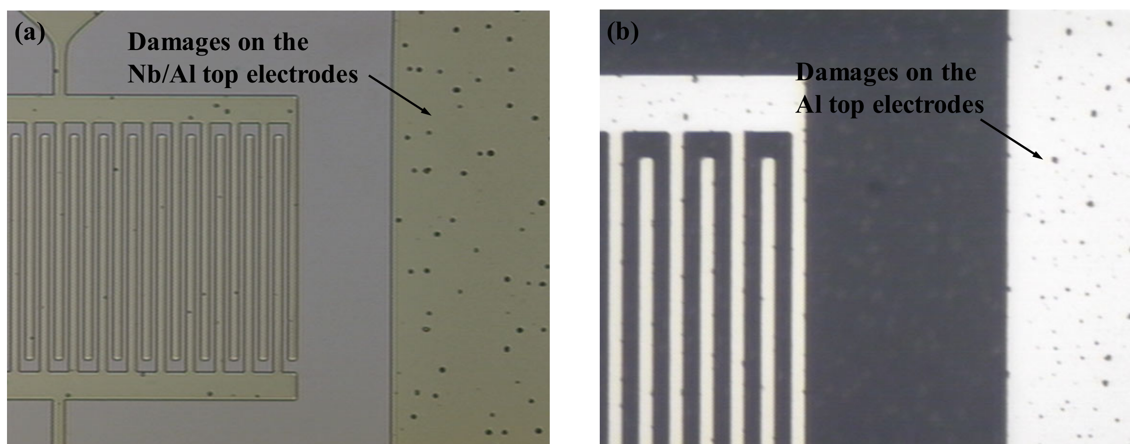

Figure 4-9. Microscope images of the (a) Al top electrodes with 20-nm-thick Nb layer and (b) Al top electrodes with 400-nm-thick PECVD oxide layer after LPCVD LTO deposition.

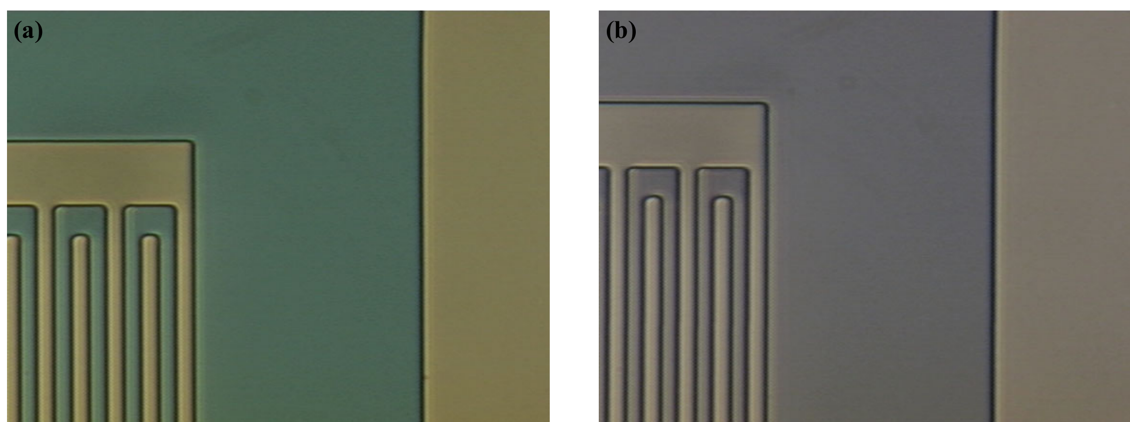

Figure 4-10. Microscope images of the Al top electrodes with 20-nm-thick Nb after (a) 400-nm-thick PECVD oxide deposition and (b) then 2-μm-thick LPCVD LTO deposition.

An alternative approach is to deposit thin plasma enhanced chemical vapor deposition (PECVD) oxide layer at 300 °C first and then 2-μm-thick LPCVD LTO layer. There is no damage on the Al top electrodes after 400-nm-thick PECVD oxide layer deposition which usually takes 30 minutes to deposit in total. However, as shown in Fig. 4–9 (b), the Al top finger electrodes exhibited notable damages after the LPCVD oxide deposition.

Finally, the issue with the damages of the Al top electrodes can be addressed using the 20-nm-thick Nb layer combined with the 400-nm-thick PECVD oxide layer. As shown in Fig. 4–10 (a), there is no damage hole in the Nb/Al top finger electrodes after the deposition of the 400-nm-thick PECVD oxide layer. The Nb/Al top electrodes still has no defects after the deposition of the 2-μm-thick LPCVD LTO layer as shown in Fig. 4–10 (b). As a result, the Al top finger electrodes can sustain the high temperature of the LPCVD furnace and the 2-μm-thick LPCVD LTO layer can be used as the hark mask for the subsequent AlN etching step. It should be noted that the different color of Figs. 4–10 (a) and (b) is caused by the different thicknesses of the oxide layer.

Chapter 5

Conclusions and Future Research Directions

To date, piezoelectric AlN MEMS LWRs present a promising technology which provides high quality factor, low motional resistance, post-CMOS compatibility, and multiple frequency operation from 100 MHz to over 2 GHz on the same chip. These AlN LWRs show the potential in terms of performance and scalability to revolutionize the current wireless communication techniques, for example, frequency references. Although crystal resonators have excellent temperature stability, the discrete quartz resonators diminish their performance in the electronic system. There is always a strong interest to replace the quartz resonators. In order to enhance the oscillator performance, the integration of micromechanical resonators directly on the oscillator circuitry is the best approach to avoid unnecessary energy loss. Therefore, the ultimate goal is the integration of the RF MEMS resonators directly with the CMOS processes, leading to a single chip solution. There are many research studies concerning how to improve the quality factors of the MEMS resonators to surpass the quartz resonators; however, they cannot achieve the excellent temperature stability as the crystal resonators perform. The passive temperature compensation technology is required for piezoelectric resonators to address the thermal stability issue. This Chapter will conclude this study on the temperature compensation of the AlN MEMS LWRs and give some possible future research directions.

5.1 Summary

This report presents the theoretical analysis, design, fabrication, and experimental results to demonstrate that an AlN LWR using the S_0 mode can achieve a zero first-order TCF by adding a SiO_2 layer with an appropriate thickness. The effective permittivity based on a transfer matrix is utilized to calculate the phase velocities of Lamb wave modes propagating in an AlN plate and an AlN/SiO_2 composite plate. The electromechanical coupling coefficient k^2 of Lamb waves excited by an IDT can be analyzed using the velocity difference method or Green's function approach. The frequency-temperature characteristics of the S_0 Lamb wave mode in an AlN plate and the QS_0 mode in an

AlN/SiO_2 composite plate are also theoretically analyzed based on their phase velocities and thermal expansion coefficients. The first-order TCFs of AlN and AlN/SiO_2 LWRs are also predicted and an optimal thickness ratio of SiO_2 to AlN is also suggested to achieve a zero first-order TCF for the AlN/SiO_2 LWRs. In addition, a feasible solution utilizing thinner AlN plates is proposed to realize the temperature compensation over a wide frequency range.

The five-mask microfabrication process for the AlN/SiO_2 LWR technology has been characterized and used to fabricate the temperature-compensated LWRs. A 25-nm-thick AlN seed layer is used to improve the crystalline orientations of the Al (111) bottom electrodes and AlN (0002) thin films. The sputtered 1-µm-thickness AlN thin film has shown good quality on the patterned Al (111) bottom electrodes with a tensile film stress within 100 MPa.

A temperature-compensated LWR operating at 711 MHz exhibits a first-order TCF of –0.31 ppm/°C, a second-order TCF of –21.5 ppb/°C^2, a motional resistance R_m of 150 Ω, an effective coupling coefficient k^2_{eff} of 0.56 %, and a quality factor Q_s of 980 at room temperature, 25 °C. In other words, this temperature-compensated LWR shows a zero first-order TCF and a second-order TCF of –21.5 ppb/°C^2 at its turnover temperature, 18.05 °C. The LWR utilizing the S_0 mode propagating in the AlN/SiO_2 composite plate achieves a high phase velocity, 7850 m/s, even though the 0.83-µm-thick SiO_2 layer reduces the overall phase velocity in the composite membranes. In addition, compared with the LWRs using grating reflectors, the edge-type reflector can efficiently reduce the resonator size without sacrificing their quality factors. The AlN LWR using edge-type reflectors, with low motional resistance, small size, potential for CMOS integration, and now good temperature stability, is a promising technology for advanced RF oscillators and narrowband filters.

5.2 Future Research Directions

This research work has presented the fundamental analysis of temperature compensation for the AlN MEMS LWRs and successfully demonstrated an AlN/SiO_2 LWR with a zero first-order TCF at room temperature. There are still a number of engineering challenges which must be addressed to optimize the performance of the AlN Lamb wave devices. This subsection presents some potential extended research works.

5.2.1 Temperature Compensation at High Temperatures

AlN is the most interesting piezoelectric thin film for high temperature applications because it can maintain its piezoelectric properties up to 1150 °C and does not exhibit phase transitions on heating from room temperature up to the melting point which exceeds 2000 °C in a nitrogen atmosphere. Many research efforts are ongoing to demonstrate AlN-based acoustic devices for high temperature applications. In addition to operation at high temperatures, maintaining the frequency-temperature stability of

piezoelectric AlN devices at high temperatures is also essential for harsh environment applications. The passive temperature compensation technology using SiO_2 presented in this work can be used to address the challenge of achieving good temperature stability at high temperatures.

5.2.2 Temperature Compensation of the Second-Order TCF

Although the temperature-compensated LWR exhibits a first-order TCF of –0.31 ppm/°C and a second-order TCF of –21.5 ppb/°C^2 at room temperature, it still shows a total frequency drift up to around 100 ppm in the temperature range from –40 to 85 °C, which is still worse than the AT-cut quartz as shown in Fig. 3–17. As a result, it is of strong interest to reduce the second-order TCF of the AlN/SiO_2 LWRs using other materials with positive second-order TCEs. Recently, Mo is reported to have a second-order TCF of +7 ppb/°C^2 [61] so the use of Mo as the top and bottom electrodes is possible to further improve the frequency-temperature stability.

5.2.3 Temperature Compensation for a Wide Frequency Range

In this work, the AlN/SiO_2 multilayer plate composed of 1-μm-thick AlN and 0.83-μm-thick SiO_2 was used to successfully reduce the first-order TCF of the LWR operating at 711 MHz from –25 to –0.31 ppm/°C at room temperature. However, the other LWR operating at 460 MHz still showed a first-order TCF of –7.61 ppm/°C due to the intrinsic dispersion of the Lamb waves. According to the theoretical simulation, an AlN layer as thin as 250 nm can significantly reduces the dispersion of the first-order TCF, and it is possible to achieve nearly zero first-order TCFs for the AlN LWRs operating at multiple frequencies on the same AlN/SiO_2 stack.

5.2.4 Temperature Compensation Using Other Materials

As discussed in Chapter 2, the oxide layer significantly decreases the phase velocity and coupling strength of the S_0 Lamb wave mode. If a thinner thermal compensation layer is used, the unwanted effects can be eliminated. To achieve a zero TCF, a higher phase velocity and a larger coupling coefficient simultaneously, a more efficient temperature compensation layer is required. Most recently, TeO_2 [64] and SiOF [67] are investigated to own larger positive TCEs than undoped SiO_2 thin films. As a result, it is interesting to integrate these new thermal compensation materials with the AlN LWRs to enhance the effective coupling strength and increase the series resonance frequency. The synthesis of new materials with positive TCEs for temperature compensation is also of great interest.

5.2.5 Temperature-Stable Oscillators Using AlN/SiO_2 LWRs

A 1.05 GHz CMOS oscillator based on an AlN contour-mode resonator was demonstrated with phase noises of –140 dBc/Hz at 100 kHz offset frequency and –81 dBc/Hz at 1 kHz

offset frequency [10]. However, the frequency-temperature stability is not addressed in the work. Therefore, it is interesting to combine the AlN/SiO_2 LWRs and CMOS circuits to realize a high-performance and zero-TCF oscillator. Some *Q*-boosting techniques can be also implemented to improve the phase noise at the same time [53], [105].

Bibliography

1. J. T. M. van Beek and R. Puers, "A review of MEMS oscillators for frequency reference and timing applications," *J. Micromech. Microeng.*, vol. 22, 013001, Jan. 2012.
2. http://www.txccorp.com.
3. C. T.-C. Nguyen, "MEMS technology for timing and frequency control," *IEEE Trans. Ultrason. Ferroelectr. Freq. Control*, vol. 54, pp. 251–270, Feb. 2007.
4. J. Wang, Z. Ren, and C. T.-C. Nguyen, "1.156-GHz self-aligned vibrating micromechanical disk resonator," *IEEE Trans. Ultrason. Ferroelectr. Freq. Control*, vol. 51, pp. 1607–1628, Dec. 2004.
5. V. Yantchev and I. Katardjiev, "Micromachined thin film plate acoustic resonators utilizing the lowest order symmetric Lamb wave mode," *IEEE Trans. Ultrason. Ferroelectr. Freq. Control*, vol. 54, pp. 87–95, Jan. 2007.
6. S. Gong, N.-K. Kuo, and G. Piazza, "GHz high-*Q* lateral overmoded bulk acoustic-wave resonators using epitaxial SiC thin film," *J. Microelectromech. Syst.*, vol. 21, pp. 253–255, Apr. 2012.
7. C.-M. Lin, Y.-Y. Chen, V. V. Felmetsger, D. G. Senesky, and A. P. Pisano, "AlN/3C–SiC composite plate enabling high-frequency and high-*Q* micro-mechanical resonators," *Adv. Mater.*, vol. 24, pp.2722–2727, May 2012.
8. V. Kaajakari, T. Mattila, A. Oja, J. Kiihamäki, and H. Seppä, "Square-extensional mode single-crystal silicon micromechanical resonator for low-phase-noise oscillator applications," *IEEE Electron Device Lett.*, vol. 25, pp.173–175, Apr. 2004.
9. Y.-W. Lin, S. Lee, S.-S. Li, Y. Xie, Z. Ren, and C. T.-C. Nguyen, "Series-resonant VHF micromechanical resonator reference oscillators," *IEEE J. Solid-State Circuits*, vol. 39, pp.2477–2491, Dec. 2004.
10. C. Zuo, J. Van der Spiegel, and G. Piazza, "1.05-GHz CMOS oscillator based on lateral-field-excited piezoelectric AlN contour-mode MEMS resonators," *IEEE Trans. Ultrason. Ferroelectr. Freq. Control*, vol. 57, pp. 82–87, Jan. 2010.
11. M. Rinaldi, C. Zuo, J. Van der Spiegel, and G. Piazza, "Reconfigurable CMOS oscillator based on multi-frequency AlN contour-mode resonators," *IEEE Trans. Electron Devices*, vol. 58, pp. 1281–1286, May 2010.
12. J. Hu, L. Callaghan, R. Ruby, and B. P. Otis, "A 50ppm 600MHz frequency reference utilizing the series resonance of an FBAR," in *Tech. Dig. IEEE Radio Frequency Integrated Circuits Symp.*, 2010, pp.325–328.

13. R. C. Ruby, M. Small, F. Bi, D. Lee, L. Callaghan, R. Parker, and S. Ortiz, “Positioning FBAR technology in the frequency and timing domain,” *IEEE Trans. Ultrason. Ferroelectr. Freq. Control*, vol. 59, pp. 334–345, Mar. 2012.

14. M. A. Schmidt and R. T. Howe, “Silicon resonant microsensors,” *Ceram. Eng. Sci. Proc.*, vol. 8, pp. 1019–1034, Oct. 1987.

15. W. C. Tang, T.-C. H. Nguyen, and R. T. Howe, “Laterally driven polysilicon resonant microstructures,” *Sens. Actuators*, vol. 20, pp. 25–32, Nov. 1989.

16. C. T.-C. Nguyen and R. T. Howe, “An integrated CMOS micromechanical resonator high-*Q* oscillator,” *IEEE J. Solid-State Circuits*, vol. 34, pp.440–455, Apr. 1999.

17. J. R. Clark, W.-T. Hsu, and C. T.-C. Nguyen, “High-*Q* VHF micromechanical contour-mode disk resonators,” in *Tech. Dig. IEEE Intl. Electron Devices Mtg.*, 2000, pp. 493–496.

18. J. R. Clark, W.-T. Hsu, M. A. Abdelmoneum, and C. T.-C. Nguyen, “High-*Q* UHF micromechanical radial-contour mode disk resonators,” *J. Microelectromech. Syst.*, vol. 14, pp. 1298–1310, Dec. 2005.

19. A. Ballato, “Piezoelectricity: history and new thrusts,” in *Proc. IEEE Intl. Ultrason. Symp.*, 1996, pp. 575–583.

20. B. Drafts, “Acoustic wave technology sensors,” *IEEE Trans. Microw. Theory Tech.*, vol. 49, pp. 795–802, Apr. 2001.

21. L. Rayleigh, “On waves propagated along the plane surface on an elastic solid,” *Proc. London Math. Soc.*, vol. 17, pp. 4–11, Nov. 1885.

22. R. M. White and F. W. Voltmer, “Direct piezoelectric coupling to surface elastic waves,” *Appl. Phys. Lett.*, vol. 7, pp. 314–316, Dec. 1965.

23. R. Weigel, D. P. Morgan, J. M. Owens, A. Ballato, K. M. Lakin, K. Hashimoto, and C. C. W. Ruppel, “Microwave acoustic materials, devices, and applications,” *IEEE Trans. Microw. Theory Tech.*, vol. 50, pp. 738–749, Mar. 2002.

24. M. Werner, S. Klose, F. Szücs, Ch. Moelle, H. J. Fecht, C. Johnston, P. R. Chalker, and I. M. Buckley-Golder “High temperature Young's modulus of polycrystalline diamond,” *Diam. Relat. Mater.*, vol. 6, pp. 344–347, Mar. 1997.

25. T.-T. Wu and Y.-Y. Chen, “Exact analysis of dispersive SAW devices on ZnO/diamond/Si layered structures,” *IEEE Trans. Ultrason. Ferroelect. Freq. Control*, vol. 49, pp. 142–149, Jan. 2002.

26. M. El Hakiki, O. Elmazria, M. B. Assouar, V. Mortet, L. Le Brizoual, M. Vanecek, and P. Alnot, “ZnO/AlN/diamond layered structure for SAW devices combining high velocity and high electromechanical coupling coefficient,” *Diam. Relat. Mater.*, vol. 14, pp. 1175–1178, Mar.–Jul. 2005.

27. M. Benetti, D. Cannata, F. Di Pietrantonio, and E. Verona, “Growth of AlN piezoelectric film on diamond for high-frequency surface acoustic wave devices,” *IEEE Trans. Ultrason. Ferroelectr. Freq. Control*, vol. 52, pp. 1806–1811, Oct. 2005.

28. C.-M. Lin, T.-T. Wu, Y.-Y. Chen, and T.-T. Chou, "Improved frequency responses of SAW filters with interdigitated interdigital transducers on ZnO/Diamond/Si layered structure," *J. Mech.* vol. 23, pp. 253–259, Sept. 2007.

29. K. Hashimoto, Ed., *RF Bulk Acoustic Wave Filters for Communications*, Norwood: Artech House, 2009.

30. W. H. Horton and R. C. Smythe, "On the trapped-wave criterion for AT-cut quartz resonators with coated electrodes," *Proc. IEEE*, pp. 598–599, Apr. 1967.

31. K. M. Lakin, G. R. Kline and K. T. McCarron, "High-*Q* microwave acoustic resonators and filters," *IEEE Trans. Microw. Theory Tech.*, vol. 41, pp. 2139–2146, Dec. 1993.

32. W. E. Newell, "Face-mounted piezoelectric resonators," *Proc. IEEE*, pp. 575–581, Jun. 1965.

33. E. Klier, "Fundamental extensional mode of circular quartz plates," *Czech. J. Phys.*, vol. 3, pp. 72–82, Mar. 1953.

34. J. Hermann and C. Bourgeois, "A new quartz crystal cut for contour mode resonators," in *Proc. IEEE Intl. Freq. Control Symp.*, 1979, pp. 255–262.

35. S. C. Hight and G. W. Willard, "A simplified circuit for frequency substandards employing a new type of low-frequency zero-temperature-coefficient quartz crystal," *Proc. Inst. Radio Eng.*, vol. 25, pp. 549–563, May 1937.

36. W. P. Mason, "A new quartz-crystal plate, designated the GT which produces a very constant frequency over a wide temperature range," *Proc. Inst. Radio Eng.*, vol. 28, pp. 220–223, May 1940.

37. G. Piazza and A. P. Pisano, "Dry-released post-CMOS compatible contour-mode aluminum nitride micromechanical resonators for VHF applications," in *Tech. Dig. Solid-State Sens. Actuators Microsyst. Workshop*, 2004, pp. 37–40.

38. G. Piazza, P. J. Stephanou, and A. P. Pisano, "Piezoelectric aluminum nitride vibrating contour-mode MEMS resonators," *J. Microelectromech. Syst.*, vol. 15, pp. 1406–1418, Dec. 2006.

39. G. Piazza, P. J. Stephanou, and A. P. Pisano, "Single-chip multiple-frequency AlN MEMS filters based on contour-mode piezoelectric resonators," *J. Microelectromech. Syst.*, vol. 16, pp. 319–328, Apr. 2007.

40. K. Toda, "Lamb-wave delay lines with interdigital electrodes," *J. Appl. Phys.*, vol. 44, pp. 56–62, Jan. 1973.

41. D. S. Ballantine, R. M. White, S. J. Martin, A. J. Ricco, G. C. Frye, E. T. Zellers, and H. Wohltjen, *Acoustic Wave Sensors: Theory, Design, and Physico-Chemical Applications*, San Diego: Academic Press, 1997.

42. R. M. White and S. W. Wenzel, "Fluid loading of a Lamb wave sensor," *Appl. Phys. Lett.*, vol. 52, pp. 1653–1655, May 1988.

43. J. Bjurström, I. Katardjiev, and V. Yantchev, "Lateral-field-excited thin-film Lamb wave resonator," *Appl. Phys. Lett.*, vol. 86, 154103, Apr. 2005.

44. J. Bjurström, I. Katardjiev, and V. Yantchev, "Thin film Lamb wave resonant structure – the first approach," *Solid-State Electron.*, vol. 50, pp. 322–326, Mar. 2006.

45. V. Yantchev, J. Enlund, J. Bjurström, and I. Katardjiev, "Design of high frequency piezoelectric resonators utilizing laterally propagating fast modes in thin aluminum nitride (AlN) films," *Ultrason.*, vol. 45, pp. 208–212, Dec. 2006.

46. V. Yantchev, L. Arapan, and I. Katardjiev, "Micromachined thin film plate acoustic resonators (FPAR): Part II," *IEEE Trans. Ultrason. Ferroelect. Freq. Control*, vol. 56, pp. 2701–2710, Dec. 2009.

47. P. J. Stephanou and A. P. Pisano, "800 MHz low motional resistance contour-extensional aluminum nitride micromechanical resonators," in *Tech. Dig. Solid-State Sens. Actuators Microsyst. Workshop*, 2006, pp. 60–61.

48. G. Piazza, P. J. Stephanou, and A. P. Pisano, "One and two port piezoelectric higher order contour-mode MEMS resonators for mechanical signal processing," *Solid-State Electron.*, vol. 51, pp. 1596–1608, Nov.–Dec. 2007.

49. M. Rinaldi, C. Zuniga, C. Zuo, and G. Piazza, "Super-high-frequency two-port AlN contour-mode resonators for RF applications," *IEEE Trans. Ultrason. Ferroelect. Freq. Control*, vol. 57, pp. 38–45, Jan. 2010.

50. C. Zuo, N. Sinha, J. Van der Spiegel, and G. Piazza, "Multifrequency Pierce oscillator based on piezoelectric AlN contour-mode MEMS technology," *J. Microelectromech. Syst.*, vol. 19, pp. 570–580, Jun. 2010.

51. C.-M. Lin, Y.-J. Lai, T.-T. Yen, J.-C. Hsu, Y.-Y. Chen, D. G. Senesky, and A. P. Pisano, "Quality factor enhancement in Lamb wave resonators utilizing AlN plates with convex edges," in *Tech. Dig. Intl. Conf. Solid-State Sens. Actuators Microsyst.*, 2011, pp. 1512–1515.

52. C.-M. Lin, V. Yantchev, Y.-Y. Chen, V. V. Felmetsger, and A. P. Pisano, "Characteristics of AlN Lamb wave resonators with various bottom electrode configurations," in *Proc. IEEE Intl. Freq. Control Symp.–Eur. Freq. Time Forum*, 2011, pp. 505–509.

53. C.-M. Lin, Y.-J. Lai, J.-C. Hsu, Y.-Y. Chen, D. G. Senesky, and A. P. Pisano, "High-*Q* aluminum nitride Lamb wave resonators with biconvex edges," *Appl. Phys. Lett.*, vol. 99, 143501, Oct. 2011.

54. I. A. Viktorov, *Rayleigh and Lamb waves: physical theory and applications*, New York: Plenum Press, 1967.

55. G. Wingqvist, L. Arapan, V. Yantchev, and I. Katardjiev, "A micromachined thermally compensated thin film Lamb wave resonator for frequency control and sensing applications," *J. Micromech. Microeng.*, vol. 19, 035018, Mar. 2009.

56. R. Melamud, S. A. Chandorkar, B. Kim, H. K. Lee, J. C. Salvia, G. Bahl, M. A. Hopcroft, and T. W. Kenny, "Temperature-insensitive composite micromechanical resonators," *J. Microelectromech. Syst.*, vol. 18, pp. 1409–1419, Dec. 2009.

57. R. Bechmann, A. D. Ballato, and T. J. Lukaszek, "Higher-order temperature coefficients of the elastic stiffness and compliances of alpha-quartz," *Proc. Inst. Radio Eng.*, vol. 50, pp. 1812–1822, Aug. 1962.

58. S. Spinner and G. W. Cleek, "Temperature dependence of Young's Modulus of vitreous germania and silica," *J. Appl. Phys.*, vol. 31, pp. 1407–1410, Aug. 1960.

59. S. Ohta, K. Nakamura, A. Doi, and Y. Ishida, "Temperature characteristics of solidly mounted piezoelectric thin film resonators," in *Proc. IEEE Intl. Ultrason. Symp.*, 2003, pp. 2011–2015.

60. J. Bjurstrom, G. Wingqvist, V. Yantchev, and I. Katardjiev, "Temperature compensation of liquid FBAR sensors," *J. Micromech. Microeng.*, vol. 17, pp. 651–658, Mar. 2007.

61. W. Pang, R. C. Ruby, R. Parker, P. W. Fisher, M. A. Unkrich, and J. D. Larson III, "A temperature-stable film bulk acoustic wave oscillator," *IEEE Electron Device Lett.*, vol. 29, pp. 315–318, Apr. 2008.

62. G. Wingqvist, L. Arapan, V. Yantchev, and I. Katardjiev, "Temperature compensation of thin AlN film resonators utilizing the lowest order symmetric Lamb mode," in *Proc. IEEE Intl. Ultrason. Symp.*, 2008, pp. 1207–1210.

63. K. Hashimoto, M. Kadota, T. Nakao, M. Ueda, M. Miura, H. Nakamura, H. Nakanishi, and K. Suzuki, "Recent development of temperature compensated SAW devices," in *Proc. IEEE Intl. Ultrason. Symp.*, 2011, pp. 79–86.

64. N. Dewan, K. Sreenivas, and V. Gupta, "Anomalous elastic properties of RF-sputtered amorphous TeO_{2+x} thin film for temperature-Stable SAW device applications," *IEEE Trans. Ultrason. Ferroelect. Freq. Control*, vol. 55, pp. 552–558, Mar. 2008.

65. W. Pan and F. Ayazi, "Thin-film piezoelectric-on-substrate resonators with Q enhancement and TCF reduction," in *Tech. Dig. IEEE Intl. Conf. Micro Electro Mech. Syst.*, 2010, pp. 727–730.

66. A. K. Samarao and F. Ayazi, "Temperature compensation of silicon resonators via degenerate doping," *IEEE. Trans. Electron Devices*, vol. 59, pp. 87–93, Jan. 2012.

67. S. Matsuda, M. Hara, M. Miura, T. Matsuda, M. Ueda, Y. Satoh, and K. Hashimoto, "Use of fluorine-doped silicon oxide for temperature compensation of radio frequency surface acoustic wave devices," *IEEE Trans. Ultrason. Ferroelect. Freq. Control*, vol. 59, pp. 135–138, Jan. 2012.

68. G. Piazza, R. Abdolvand, G. K. Ho, F. Ayazi, "Voltage-tunable piezoelectrically-transduced single-crystal silicon micromechanical resonators," *Sens. Actuators A*, vol. 111, pp. 71–78, Mar. 2004.

69. D. E. Serrano, R. Tabrizian, F. Ayazi, "Electrostatically tunable piezoelectric-on-silicon micromechanical resonator for real-time clock," *IEEE Trans. Ultrason. Ferroelect. Freq. Control*, vol. 59, pp. 358–365, Mar. 2012.

70. B. A. Auld, *Acoustic Fields and Waves in Solids*, New York: Wiley, 1973.

71. K. Tsubouchi and N. Mikoshiba, "Zero-temperature-coefficient SAW devices on AlN epitaxial filsm," *IEEE Trans. Sonics Ultrason.*, vol. SU-32, pp. 634–644, Sept. 1985.

72. H. Iwanaga, A. Kunishige, and S. Takeuchi, "Anisotropic thermal expansion in wurtzite-type crystals," *J. Mater. Sci.*, vol. 35, pp. 2451–2454, May 2000.

73. V. Cimalla, J. Pezoldt, O. Ambacher, "Group III nitride and SiC based MEMS and NEMS: materials properties, technology and applications," *J. Phys. D: Appl. Phys.* vol. 40, pp. 6386–6434, Oct. 2007.

74. M. E. Levinshtein, S. L. Rumyantsev, and M. S. Shur, Ed., *Properties of advanced semiconductor materials: GaN, AlN, InN, BN, SiC, SiGe*, New York: Wiley, 2001.

75. A. A. Nassar, *Excitation of Surface Waves with Piezoelectric Layers*, Ph. D. dissertation, Department of Electrical Engineering, McGill University, Montreal, Canada, 1983.

76. Y.-Y. Chen, *A Theoretical and Experimental Study of Layered SAW Devices and Its Applications*, Ph. D. dissertation, Institute of Applied Mechanics, National Taiwan University, Taipei, Taiwan, 2002. (in Chinese)

77. S. G. Joshi and Y. Jin, "Excitation of ultrasonic Lamb waves in piezoelectric pates," *J. Appl. Phys.*, vol. 69, pp. 8018–8024, Jun. 1991.

78. Y.-Y. Chen, "Exact analysis of Lamb waves in piezoelectric membranes with distinct electrode arrangements," *Jpn. J. Appl. Phys.*, vol. 48, 07GA06, Jul. 2009.

79. Y.-Y. Chen, "Theoretical analysis of electromechanical coupling coefficient of Lamb waves in ZnO/Si multilayered piezoelectric plates," *Jpn. J. Appl. Phys.*, vol. 49, 07HD23, Jul. 2010.

80. C.-M. Lin, Y.-Y. Chen, and A. P. Pisano, "Theoretical investigation of Lamb wave characteristics in AlN/3C–SiC composite membranes," *Appl. Phys. Lett.*, vol. 97, 193506, Nov. 2010.

81. B. Honein, A. M. B. Braga, P. Barbone, and G. Herrmann, "Wave propagation in piezoelectric layered media with some applications," *J. Intell. Mater. Syst. Struct.*, vol. 2, pp. 542–557, Oct. 1991.

82. D. P. Morgan, *Surface-Wave Devices for Signal Processing*, Holland: Elsevier, 1991.

83. L. E. McNeil, M. Grimsditch, and R. H. French, "Vibrational spectroscopy of aluminum nitride," *J. Am. Ceram. Soc.*, vol. 76, pp. 1132–1136, May 1993.

84. K. Hashimoto, *Surface Acoustic Wave Devices in Telecommunications: Modelling and Simulation*, Germany: Springer-Verlag, 2000.

85. V. V. Felmetsger, P. N. Laptev, and S. M. Tanner, "Innovative technique for tailoring intrinsic stress in reactively sputtered piezoelectric aluminum nitride films," *J. Vac. Sci. Technol. A*, vol. 27, pp. 417–422, May–Jun. 2009.

86. S. M. Tanner and V. V. Felmetsger, "Microstructure and chemical wet etching characteristics of AlN films deposited by ac reactive magnetron sputtering," *J. Vac. Sci. Technol. A*, vol. 28, pp. 69–76, Jan.–Feb. 2010.

87. V. V. Felmetsger and M. K. Mikhov, "Deposition of smooth and highly (111) textured Al bottom electrodes for AlN-based electroacoustic devices," in *Proc. IEEE Intl. Freq. Control Symp.*, 2012, pp.411–414.

88. V. V. Felmetsger and P. N. Laptev, "Deposition of ultrathin AlN films for high frequency electroacoustic devices," *J. Vac. Sci. Technol. A*, vol. 29, 021014, Mar.–Arp. 2011.

89. G. F. Iriarte, J. Bjurstrom, J. Westlinder, F. Engelmark, and I. V. Katardjiev, "Synthesis of c-axis-oriented AlN thin films on high-condcuting layers: Al, Mo, Ti, TiN, and Ni," *IEEE Trans. Ultrason. Ferroelectr. Freq. Control*, vol. 52, pp. 1170–1174, Jul. 2005.

90. C.-M. Lin, T.-T. Yen, V. V. Felmetsger, M. A. Hopcroft, J. H. Kuypers, and A. P. Pisano, "Thermal compensation for aluminum nitride Lamb wave resonators operating at high temperature," in *Proc. IEEE Intl. Freq. Control Symp.*, 2010, pp. 14–18.

91. C.-M. Lin, T.-T. Yen, V. V. Felmetsger, M. A. Hopcroft, J. H. Kuypers, and A. P. Pisano, "Thermally compensated aluminum nitride Lamb wave resonators for high temperature applications," *Appl. Phys. Lett.*, vol. 97, 083501, Aug. 2010.

92. J. H. Kuypers, C.-M. Lin, G. Vigevani, and A. P. Pisano, "Intrinsic temperature compensation of aluminum nitride Lamb wave resonators for multiple-frequency references," in *Proc. IEEE Intl. Freq. Control Symp.*, 2008, pp. 240–249.

93. C.-M. Lin, T.-T. Yen, Y.-J. Lai, V. V. Felmetsger, M. A. Hopcroft, J. H. Kuypers, and A. P. Pisano, "Experimental study of temperature-compensated aluminum nitride Lamb wave resonators," in *Proc. Eur. Freq. Time Forum–IEEE Intl. Freq. Control Symp.*, 2009, pp.5–9.

94. C.-M. Lin, T.-T. Yen, Y.-J. Lai, V. V. Felmetsger, M. A. Hopcroft, J. H. Kuypers, and A. P. Pisano, "Temperature-compensated aluminum nitride Lamb wave resonators," *IEEE Trans. Ultrason. Ferroelectr. Freq. Control*, vol. 57, pp. 524–532, Mar. 2010.

95. J. F. Rosenbaum, *Bulk Acoustic Wave Theory and Devices*, Norwood: Artech House, 1998

96. K. M. Lakin, "Modeling of thin film resonators and filters," in *Tech. Dig. IEEE MTT-S Intl. Microw. Symp.*, 1992, pp. 149–152.

97. J. D. Larson III, P. D. Bradley, S. Wartenberg, and R. C. Ruby, "Modified Butterworth-Van Dyke circuit model for FBAR resonators and automated measurement system," in *Proc. IEEE Intl. Ultrason. Symp.*, 2000, pp. 863–868.

98. B. Razavi, "A study of phase noise in CMOS oscillators," *IEEE J. Solid-State Circuits*, vol. 31, pp. 331–343, Mar. 1996.

99. R. Aigner, "Bringing BAW technology into volume production: the ten commandments and the seven deadly sins," in *Proc. 3rd Intl. Symp. Acoustic Wave Devices for Future Mobile Communication Systems*, 2007, pp. 85–91.

100. V. Yantchev and I. Katardjiev, "Quasistatic transduction of the fundamental symmetric Lamb mode in longitudinal wave transducers," *Appl. Phys. Lett.*, vol. 88, 214101, May 2006.

101. P. Nicolay, O. Elmazria, B. Assouar, F. Sarry, and L. Lebrizoual, "Theoretical and experimental study of the differential thermal expansion effect on the TCD of layered SAW temperature sensors," in *Proc. IEEE Intl. Ultrason. Symp.*, 2007, pp. 272–275.

102. M. Dubois, C. Billard, C. Muller, G. Parat, and P. Vincent, "Integration of high-*Q* BAW resonators and filters above IC," in *Tech. Dig. IEEE Intl. Solid-State Circuits Conf.*, 2005, pp. 392–393.

103. C.-M. Lin, W.-C. Lien, T.-T. Yen, V. V. Felmetsger, D. G. Senesky, M. A. Hopcroft, and A. P. Pisano, "Growth of highly *c*-axis oriented AlN films on 3C–SiC/Si substrate," in *Tech. Dig. Solid-State Sens. Actuators Microsystems Workshop*, Hilton Head, SC, 2010, pp. 324–327.

104. C.-M. Lin, W.-C. Lien, V. V. Felmetsger, M. A. Hopcroft, D. G. Senesky, and A. P. Pisano, "AlN thin films grown on epitaxial 3C–SiC (100) for piezoelectric resonant devices," *Appl. Phys. Lett*., vol. 97, 141907, Oct. 2010.

105. B. P. Harrington and R. Abdolvand, "In-plane acoustic reflectors for reducing effective anchor loss in lateral–extensional MEMS resonators," *J. Micromech. Microeng.*, vol. 21, 085021, Aug. 2011.